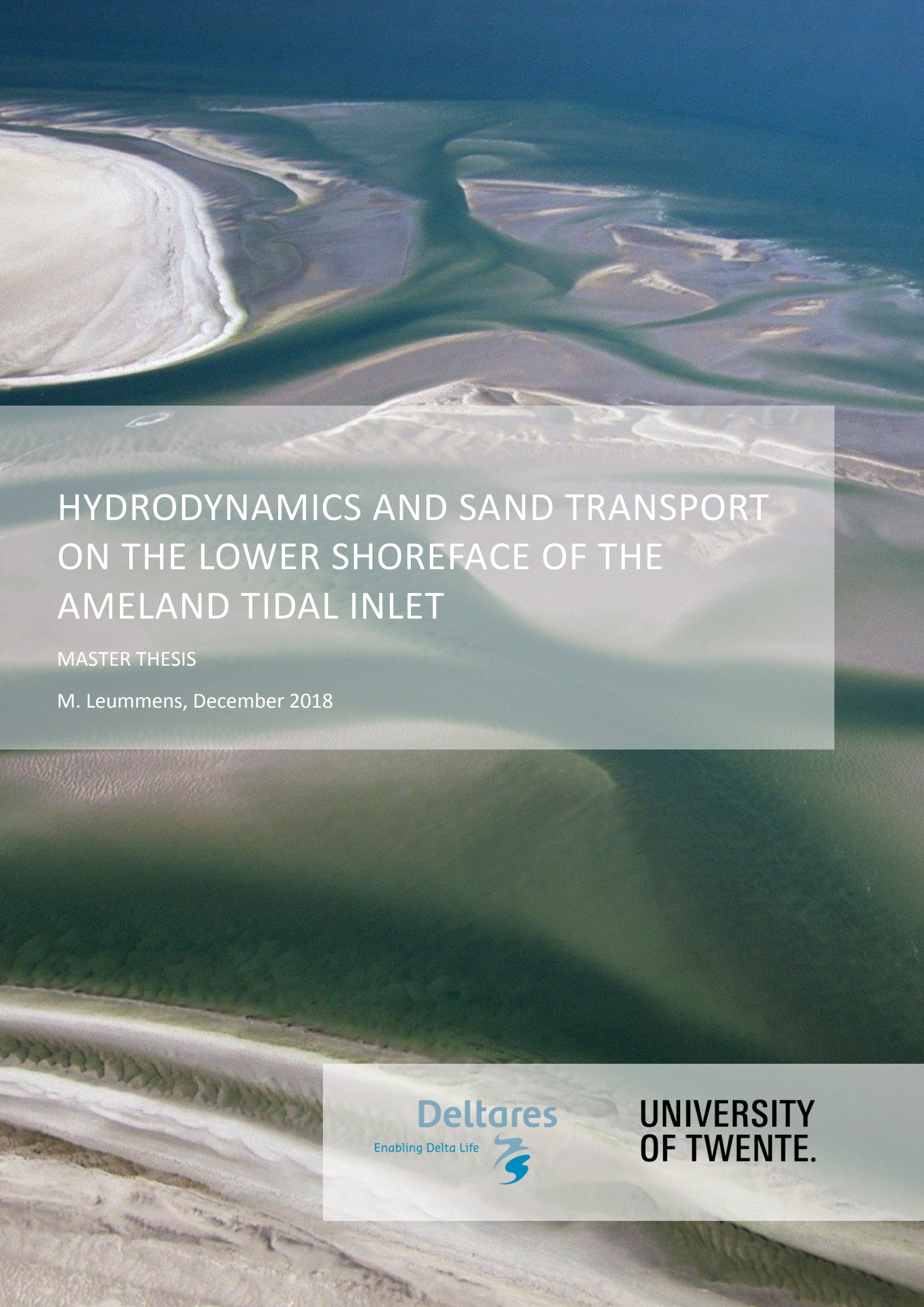

HYDRODYNAMICS AND SAND TRANSPORT ON THE LOWER SHOREFACE OF THE AMELAND TIDAL INLET

MASTER THESIS

M. Leummens, December 2018

Deltares
Enabling Delta Life

UNIVERSITY OF TWENTE.

HYDRODYNAMICS AND SAND TRANSPORT ON THE LOWER SHOREFACE OF THE AMELAND TIDAL INLET

by

Max Leummens

In partial fulfilment of the requirements for the degree of Master of Science in Water Engineering and Management at the University of Twente

December 2018

Delft

Contact: max.leummens@gmail.com

Graduation Committee: Prof. Dr. Kathelijne M. Wijnberg (University of Twente)

Dr.ir. Jebbe J. van der Werf (Deltares / University of Twente)

Cover Image: Martin Stock, Landesbetrieb Küstenschutz, Nationalpark, Meeresschutz Schleswig-Holstein. Retrieved from: https://www.merian.de/europa/deutschland/galerie/nationalparks-in-deutschland

SUMMARY

The lower shoreface, part of the coastal profile located between 8 and 20 m water depth, corresponds to the deeper part of the so-called Coastal Foundation. This is defined as a coastal area between the first row of the dunes and 20 m depth contour and is one of the main concepts for the management of the Dutch coast. In order to provide the long-term safety given sea level rise, yearly nourishments are applied on the coast and its volume is determined based on the rate of yearly sea level rise and the area of the Coastal Foundation assuming there is no significant net sediment transport through the offshore boundary. This assumption, however, is not well substantiated and, because of that, the "Kustgenese 2.0" ("Coastal Genesis 2.0", KG2) was started by Rijkswaterstaat along with the lower shoreface subproject at Deltares in order to investigate potential alternatives for the offshore boundary of the Coastal Foundation and required nourishment volume. For this purpose, Grasmeijer (2018) proposed a new "offline" approach, in which net annual sediment transport rates at any location can be calculated using simplified Van Rijn (2007a, b) formulas (TSAND model) with input currents from the DCSM-FM model (Zijl et al., 2018) and waves from the Wave Transformation Tool (de Fockert et al., 2011).

The objective of this master project was to obtain a better understanding of the hydrodynamics and sediment transport on the lower shoreface of the Ameland tidal inlet and to validate the new sediment transport modelling approach. To meet these objectives, first, current measurements conducted in November and December of 2017 on the lower shoreface of the Ameland tidal inlet at 11, 16 and 20 m water depth were analysed in order to assess the effect of storms. The data analysis has shown that during storm events characterised by north-western wind and waves of more than 4 m there is a strong eastward and onshore residual flow on the lower shoreface increasing towards the shallow water, signs of which are also observed at 20 m water depth. Validation of the DCSM model, however, has shown that these currents are not captured by the model that does not include wave-driven currents. Comparing the results to the detailed Delft3D model of Nederhoff et al. (2018) with and without waves confirmed that the mismatch is not caused by the model resolution. Using the measured and the DCSM model currents as input for the TSAND model has shown that, even though statistically the model performs relatively well, the mismatch in currents during storms results in a similar mismatch in cross-shore and longshore sediment transport. Comparison of the transport rates predicted using measured current with the yearly transport rates calculated with the DCSM currents has shown that on a yearly time scale this mismatch can be significant even at 20 m water depth and, because of that, in its current state the "offline" approach cannot be applied for the analysis of the net annual sediment transport rates on the lower shoreface of the Ameland tidal inlet. Besides that, contribution of different sediment transport mechanisms to the net annual sediment transport was studied using the TSAND model with the DCSM model currents for the years 2013 to 2017 and the measured currents. This analysis has shown that the absence of wave-driven currents in the DCSM model also affects the calculated contributions of different mechanisms at shallow part of the lower shoreface, however, some qualitative conclusions still could be made there. The analysis has shown that wave asymmetry and near bed wave-induced streaming play very small role in the net annual suspended load and bedload sediment transport respectively. The additional transport due to Stokes drift can be significant, especially for the years that are characterized by large storm events, as well as wind-driven currents, which cause an increased eastward longshore and offshore transport.

PREFACE

This report is the result of the master thesis project that was carried out over a period of nine months at Deltares in Delft and is the final part of my study at the University of Twente. First of all, I would like to thank Jebbe van der Werf, who was my supervisor at Deltares, for making this project possible, for numerous long meetings discussing the results and his guidance that helped to overcome any difficulties that appeared. Also, I would like to thank Kathelijne Wijnberg for the valuable feedback during all the stages of the project, Bart Grasmeijer, Firmijn Zijl and Jelmer Veenstra for the providing the models that were used during the project and for being open to answer all the questions that I encountered, Lodewijk de Vet and Floris de Wit for their help with data processing and analysis. Finally, I would like to thank my fellow students at Deltares for all the nice discussions we had during lunch breaks and additional motivation for the work that they gave me, my family for their continuous support and my friends in Russia, who were far away but always seemed to be very close.

Hope you enjoy reading this report.

Max Leummens

Delft, December 2017

CONTENTS

LIST OF FIGURES

LIST OF TABLES

1 INTRODUCTION

1.1 FRAMEWORK

In order to develop knowledge necessary to make decisions about the maintenance and management of the Dutch coast after 2020, the "Kustgenese 2.0" ("Coastal Genesis 2.0", KG2) project was started by Rijkswaterstaat in 2017. The scope of Deltares subproject "Diepere Vooroever" (DV, "Lower Shoreface") within the KG2 project is mainly determined by two following questions:

1. What are the possibilities for an alternative offshore boundary of the coastal foundation?
2. How much sediment is required for the coastal foundation to grow with the sea level rise?

Deltares aims to answer both these questions by studying net cross-shore sediment transport on the Dutch lower shoreface as a function of depth based on numerical modelling as well as on new field measurements, that were conducted within the KG2 project measurement campaign in a period between August of 2017 and May of 2018 at three locations along the Dutch coast: Ameland tidal inlet, central part of the Terschelling island coast and at the Holland coast near Noordwijk (Figure 1). For each location measurements included multibeam bathymetry, boxcore and vibrocore sampling and flow and sand transport processes from three frames, which were placed along a cross-shore profile at different water depths.

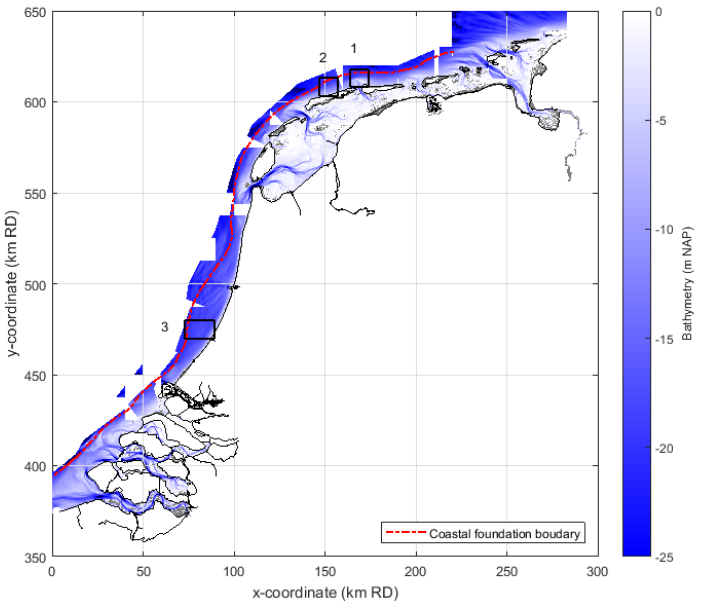

Figure 1 "Kustgenese 2.0" field campaign locations: 1 – Ameland tidal inlet; 2 – Terschelling island coast; 3 – Holland coast at Noordwijk

This master thesis project focuses on the lower shoreface of the Ameland tidal inlet, where the field campaign took place in November and December of 2017. Lower shoreface in general is a rather complex area, where currents are determined by a combination of the effects of tide, waves, wind and density gradients due to river freshwater discharge. In the Wadden Sea area in front of a tidal inlet it becomes even more complicated as the coastline is interrupted and the exchange between the North Sea and the Wadden Sea also can have a significant impact on currents and sediment transport on the lower shoreface. Most of the previous field and modelling studies on the Dutch lower shoreface were focused mainly on the uninterrupted Holland coast, including modelling studies of Roelvink and Stive (1990) and Van Rijn (1997) on the net annual sediment transport. For the lower shoreface of the Wadden coast and especially for the tidal inlets information is very limited.

In order to study the sediment transport processes on lower shoreface along the entire Dutch coast, a new so-called “offline” approach was proposed at Deltares by Grasmeijer (2018). Within this approach, modelled currents and wave conditions are used as input for a 1DV transport model TSAND, which is based on simplified expressions of Van Rijn (2007a, b). The input is derived using the 3D DCSM-FM hydrodynamic model (Zijl et al., 2018) and Wave Transformation Tool (Fockert et al., 2011). Using this method, sediment transport rates can be determined at any location for multiple years given that the model output is available. This allows to compute the net annual sediment transport, study its variation and analyse contribution of different physical processes, which is essential for investigating alternatives for the offshore coastal foundation boundary and required nourishment volume. However, there are two main issues with this method, which are related to the flow conditions input. First of all, the resolution of the DCSM model is quite low, with minimum grid cell size of approximately 900 m at the area of interest and, second, the model does not include the effect of wave-induced currents. These two factors together can lead to mismatch between real sediment transport rates over the Dutch lower shoreface and ones that are predicted using this offline approach, which might be significant for answering the questions defined for the KG2 project. Because of this, it was necessary to validate this method using the field data, while combining the new measurements and a hydrodynamic model allows to analyse to what extend different processes affect the currents on the lower shoreface and to assess their relative importance for the net annual sediment transport.

1.2 OBJECTIVE AND RESEARCH QUESTIONS

The objective of this master thesis was twofold, first, to obtain better understanding about the hydrodynamics and sediment transport processes on the lower shoreface of the Ameland tidal inlet, in particular about the contribution of wave-driven currents to the total current and about physical mechanisms that determine the net annual sediment transport, and, second, to validate the new sediment transport modelling approach for the lower shoreface of the Ameland tidal inlet. In order to meet this objective, three major research questions were formulated and each of them was also divided into several sub questions:

1. What are the hydrodynamics at the lower shoreface of the Ameland tidal inlet?
    1.1. What is the vertical structure of the currents?
    1.2. How do currents vary in time and in cross-shore direction?
    1.3. What is the effect waves and wind on currents, particularly during storm events?
2. How valid is the offline sediment transport modelling approach for the lower shoreface of the Ameland tidal inlet?
    2.1. How well does the DCSM-FM model reproduce the measured currents?
    2.2. What are the implications of using DCSM-FM model currents on predicted sediment transport rates?
3. What is the magnitude and direction of the cross-shore and longshore net annual sediment transport on the lower shoreface of the Ameland tidal inlet and which physical mechanisms determine this?
    3.1. What is the average net annual sediment transport and how does it vary from year to year and what causes the variation?
    3.2. What are the dominant mechanisms that determine sediment transport?
    3.3. How sensitive are the results for varying model input parameters?

1.3 APPROACH

In order to answer the first research question, measurements, conducted during the KG2 field campaign at the lower shoreface of the Ameland tidal inlet, were analysed. From the vast range of data collected during that campaign, this master thesis project focused primarily on currents measured at three frames that were placed on the lower shoreface at 20, 16 and 11 m water depth. The analysis of the data focused on spatial and

temporal variation of the currents on the lower shoreface and included harmonic analysis of the tidal currents, analysis of the vertical structure, residual currents, determined using the Fourier transform low-pass filter, and time-average current profiles for the entire measurement period as well as for particular wind and wave conditions in order to analyse their influence of storm events on currents.

To answer the second research question, the DCSM model (Zijl et al., 2018) was validated using the standard water level measurements, currents data from the KG2 field campaign and measured discharges through the tidal inlet. During that validation, the DCSM model versions with the resolution near the Dutch coast of 1800 and 900 m were used. Besides that, an additional model run with refined grid (450 m) in the Wadden Sea area and updated model bathymetry at the area of the Ameland tidal inlet was performed in order to assess the impact of these two factors on the model results. Validation of the model water levels was done for two stations near the Ameland tidal inlet inside and outside of the Wadden Sea using the goodness of fit statistics, harmonic analysis and surge water levels currents, also determined using the Fourier transform low-pass filter. Currents on the lower shoreface were validated in the longshore and cross-shore direction using goodness of fit statistics, but also by comparing measured and modelled instant current profiles, depth average residual currents and time-average profiles for the entire period of the field campaign at three locations along the lower shoreface. Also, in order to assess the effect of the wave-driven currents and the model resolution, the measured and the DCSM model currents were compared with the results of the detailed Delft3D model of the Ameland tidal inlet (Nederhoff et al., 2018). At the next stage, the measured and the modelled currents along with the wave conditions from the Wave Transformation Tool (Fockert et al., 2011) were used as input for the TSAND model to compute the sediment transport rates for the period of the field campaign and the net annual sediment transport rates for the period from 2013 to 2017. Based on the results of the sediment transport computations a conclusion was made regarding applicability of the offline sediment transport modelling approach for the lower shoreface of the Ameland tidal inlet.

For the third research question, sediment transport calculations were done using TSAND including and excluding different sediment transport mechanisms in order to assess their contribution to the net annual sediment transport. The effects of Longuet-Higgins streaming and Stokes drift were analysed using the analytical expressions for their contribution to the currents, which were then added to the currents that were used to compute bed load and suspended load transport respectively. To compute sediment transport due to wave velocity asymmetry the equation of Van Rijn (2007b) included in the TSAND model was used. To analyse contributions of these mechanisms to the net annual sediment transport, they were first analysed for the period of the field campaign for the measured and the modelled currents in order to assess the effect of the data-model mismatch on the calculated sediment transport rates related to a particular mechanism. After that, the net annual transport was analysed using the TSAND results for the modelled currents for the period of 5 years from 2013 to 2017. To assess the role of wind-driven currents an additional DCSM model run was performed for conditions without wind for the year of 2017. The sediment transport rates calculated using the output of this model run was then compared to the results for the run with wind and with the sediment transport calculated for the field campaign.

1.4 THESIS OUTLINE

This master thesis report contains seven chapters. In the Chapter 2 the information on the relevant Dutch coastal policy, characteristics of the study area including typical wind, wave and current conditions is given. Chapter 3 contains description of the available velocity measurements, methods that were used for the data processing and analysis, offline sediment transport modelling approach and its component (TSAND, DCSM-FM model and Wave Transformation Tool), Delft3D model of the Ameland tidal inlet and the methodology that was used for validation of this approach and for sediment transport modelling. In the Chapter 4 the results of the data analysis are presented, particularly on variation of tidal and residual currents over the cross-shore profile of the lower shoreface. Chapter 5 covers the results of the offline sediment transport modelling

approach validation, including comparison of the measured and the modelled currents and analysis of the predicted sediment transport rates. Chapter 6 contains the results on the analysis of the processes contributing to the net annual sediment transport, including the effects of Longuet-Higgins streaming, wave velocity asymmetry, Stokes drift and wind-driven currents. The discussion, conclusions and recommendations are presented in Chapter 7.

2. LITERATURE REVIEW

In the current section some results from the literature review, which was done prior to the start of this master thesis project, will be presented. It will include, first, the background on the Dutch coastal policy and the concept of the Coastal Foundation, which is essential for calculating annual nourishment volume and maintaining safety of the Dutch coast. Besides that, general definition of the lower shoreface will be given and characteristics of the lower shoreface of the Ameland tidal inlet will be presented along with its typical wind and wave conditions. After that, a general description of currents and sediment transport processes on the lower shoreface will be given along with the impact they can have on the net annual sediment transport.

2.1 DUTCH COASTAL POLICY

The Dutch coastal policy aims for a safe, economically strong and attractive coast. This is achieved by preserving the strength of the dunes at a predefined safety level in order to provide sufficient protection against flooding. To prevent further structural recession of the coastline, the "Dynamic Preservation" policy was adopted in 1990 in which a "base coastline" was defined for 250 m wide sections along the coast. This coastline has to be maintained in order to provide sustainable safety level of the dunes (Taal et al., 2006). However, soon it became clear that the risk of coastal flooding in the future is expected to be higher as a consequence of socio-economic development and increasing value of the coastal zone as well as increasing probability of flooding, which is mainly related to the long-term relative sea level rise due to the climate change and postglacial subsidence of the North Sea basin, leading also to increased frequency and intensity of the storm conditions (van der Burgh, 2018). Relative sea level rise is also strongly related to the evolution of the coast and hence coastal sediment budgets, and can lead to the shoreline recession. The amount of recession can be defined according to the geometric shift concept of Bruun, in which (dynamic) equilibrium profile of the beach and surf zone moves upward and landward in response to the sea level rise (Figure 2).

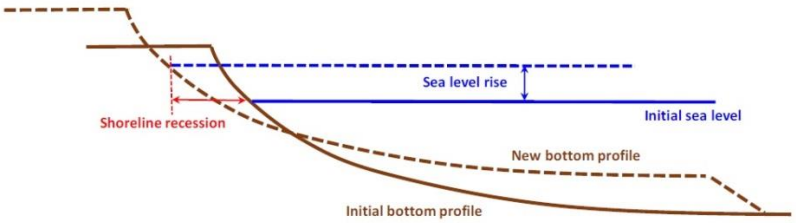

Figure 2 Coastal recession due to sea level rise according to the concept of Bruun (Van Rijn, 2016)

Therefore, it was decided to adopt a more long-term and large-scale approach for maintaining safety in the coastal zone. This approach was elucidated in the National Spatial Strategy (NSS, 2004), in which the Coastal Foundation concept was introduced (van der Burgh, 2018). This was defined as the area along the Dutch coast between the -20 m NAP depth contour (Figure 1) and the landward edge of the first dune row for the closed coast and tidal inlets for open coast. Such definition of the seaward boundary of the Coastal Foundation is based on two main reasons. Firstly, it corresponds to the landward boundary of the sand extraction zone, which is located seaward of the 20 m depth contour in order to limit the effect of sand extraction on the coastal zone, and, secondly, it is assumed that there is no significant sediment transport across this boundary. In order to provide long-term safety of the dune area with sea level rise sediment budget of the Coastal Foundation should be maintained and the primary method to do it is by means of sand nourishments (van der Burgh, 2018). The amount of required annual input of sand to the Coastal Foundation, based on the concept of

Bruun and assuming no sediment transport through the boundaries, can be determined according to the following equation from Lodder (2016):

$$Q_{nour} = A_{CF} * SLR + Q_{losses} \quad (1.1)$$

where A_{CF} – area of the coastal foundation, SLR – annual relative sea level rise and Q_{losses} – compensation term for sediment losses into the Western Scheldt and Wadden Sea and for land subsidence. From this expression, total yearly averaged nourishment volume on the Dutch coast is equal to 12.5 million m^3 of sand which is actually nourished every year since 2000 (Lodder, 2016). The area of the coastal foundation, which is used in this expression, depends on the position of the offshore boundary. Currently assumed boundary at -20 m water depth, however, is not very well substantiated and if it will be defined differently, area of the coastal foundation and, consequently, required nourishment volume will also be different.

2.2 HYDRODYNAMIC PROCESSES ON THE LOWER SHOREFACE

Significant part of the Coastal Foundation corresponds to the shoreface, which is defined as an active littoral zone between the low tide water level at the coast and a nearly horizontal continental shelf (Niedoroda et al., 1984). In cross-shore direction it can be subdivided in several zones based on sediment transport processes. The depths of the upper and lower boundaries of the shoreface and its zones are variable depending upon local sediment supply and on wave and current conditions, which leads to different classifications in the literature. In general, for the Dutch coast three major zones within the shoreface can be distinguished: upper shoreface, which corresponds to the surf zone with breaker bars between waterline and -8 m depth contour with mean bottom slopes between 1:50 and 1:200, lower shoreface, located between -8 m and -20 m depth contours with slopes between 1:200 and 1:1000, and offshore transitional zone, which is between -20 m depth contour and the shelf with bottom slope less than 1:1000 (Figure 3). In the work of Van Rijn (2016) these zones are defined as upper, middle and lower shoreface, respectively.

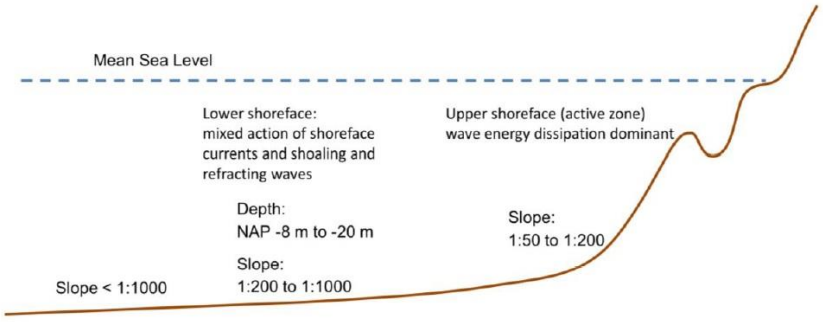

Figure 3 Typical Dutch cross-shore coastal profile

Hydrodynamic conditions on the shoreface are influenced by multiple forcing mechanisms and what is observed in nature is usually a resultant response to these mechanisms which is also varying with water depth (Niedoroda et al., 1985). According to their forcing main hydrodynamic processes can be divided into tidal, wind-, wave- and density-induced currents, and the wave-induced orbital motion. In general, upper shoreface is defined as an active zone with wave energy dissipation dominant and it is characterized by relatively large sediment transport rates and shorter response time of the morphology, almost on the scale of events. At the lower shoreface, on the other hand, sediment transport rates are relatively small and hence the response time of the morphology are generally slow, on a scale of years (Van Rijn, 2016). In this section of the report a general description of the Ameland tidal inlet will be given, including characteristics of the lower shoreface and regular wind and wave conditions. Besides that, it will include an overview of different forcing mechanisms in terms of what contribution they make for resulting currents in general and how important are these contributions particularly for the lower shoreface of the Ameland tidal inlet.

2.2.1 CHARACTERISTIC OF THE AMELAND TIDAL INLET LOWER SHOREFACE

The Ameland tidal inlet is located in the northern part of the Netherlands between barrier islands Terschelling and Ameland and is one of the inlets that connect the Dutch Wadden Sea to the North Sea (Figure 4). This area is characterised by semidiurnal tide, which propagates along the Dutch coast from south-west to north-east with a mean tidal range at the Ameland tidal inlet of approximately 2 m. As a result, Ameland tidal inlet experiences strong alongshore tidal current with peak velocities of the order of 1 m/s at the seaward boundary of the shoreface zone. Flood current is slightly higher than ebb current, which results in a residual tidal current along the coast directed to the east of order of 0.1 m/s (Van Rijn, 2013). Also, tidal wave shows a faster rise and slower fall which implies flood dominant conditions. Besides that, the inlet channel itself is also characterised by strong currents of order of 1 m/s (Dissanayake, 2011), which are mainly driven by head difference between the North Sea and the Wadden Sea. This head difference is a result of non-linear interaction between tide and storm surge, which is generated by meteorological effects, such as wind shear stress and pressure drop.

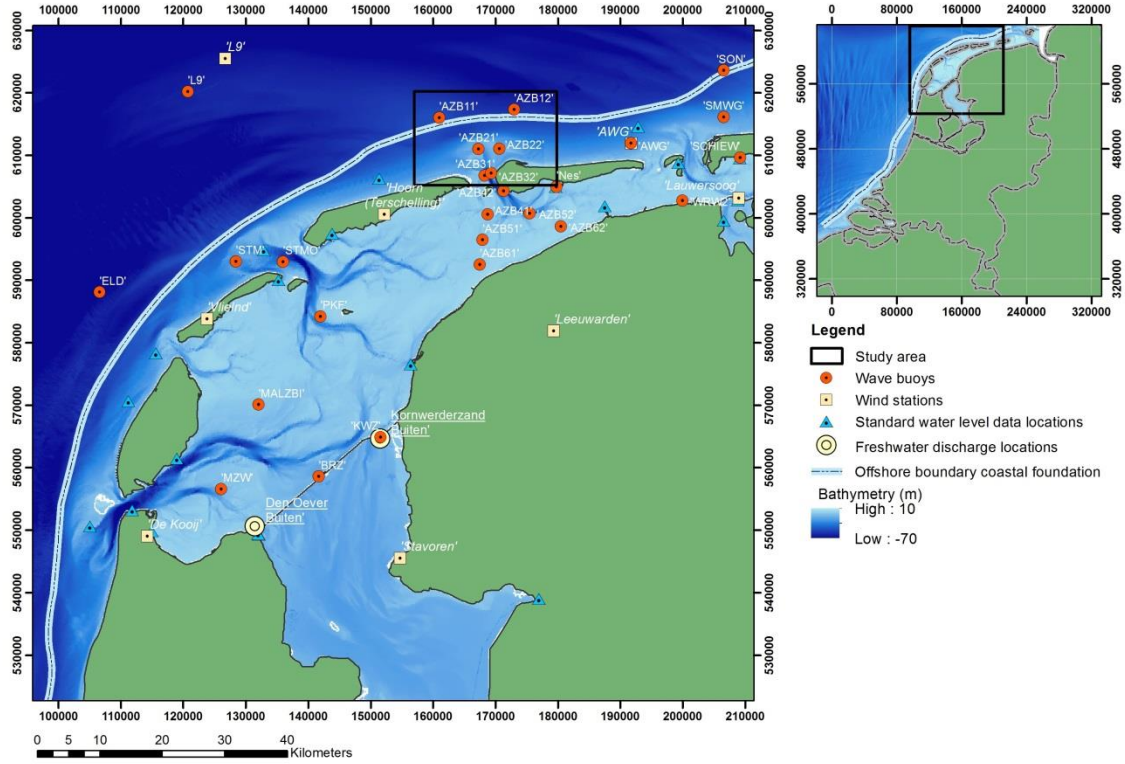

Figure 4 Study area and locations of standard water levels, wind and waves measurements

In order to analyse the currents on the lower shoreface and relate measured data to particular wind and wave conditions, data from regular wave buoys and KNMI weather stations is necessary. In Figure 4 locations of buoys and weather stations near the study area is shown along with locations where standard water level measurements are conducted. From this figure it can be seen that Ameland tidal inlet is covered by wave buoys quite well. These wave buoys, which are titled 'AZB' on the map, were placed in 2003 and they record significant wave height, wave direction and mean and peak wave periods for approximately half a year each year, mainly during autumn and winter. This means that they also cover the period when the KG2 field campaign took place and can be used to relate measured currents on the lower shoreface with observed wave conditions. In particular, buoys 'AZB11' and 'AZB12', located at water depth of approximately 20 m, were used. Besides that, in order to understand how conditions, observed during KG2 field campaign, relate to regular wave conditions long continuous observations dataset is needed. For that purpose station Eierlandse Gat,

which is located offshore of Eierland tidal inlet at water depth of 26 meters ('ELD' in Figure 4) and has data on significant wave height, wave direction and mean wave period available for a time interval between 1979 and 2018, was used. Data on meteorological conditions was derived from KNMI weather station #251 Hoorn (Terschelling), which has a 24 years long time series of hourly wind observations available, from 1994 to 2018.

To analyse regular wave conditions, significant wave height and mean wave period related to exceedance probabilities of 50, 10, 1 and 0.1 % were calculated. The results are presented in Table 1.

Table 1 Wave characteristics at Eierlandse Gat station

Exceedance	Significant wave height [m]	Mean wave period [s]
50 %	1.2	4.6
10 %	2.5	5.8
1 %	4.2	7.1
0.1 %	5.8	8.2

In Figure 5 wind (a) and wave roses (b) are presented, which illustrate how wind speed and wave height are distributed according to their direction and how often particular wind and wave conditions occur. For both characteristics roses in Figure 5 are given for the entire period of available measurements. From the first figure it can be seen, that dominant wind direction is from southwest and in general wind is originating in the third quadrant (between west and south) and for the same directions the strongest winds are mostly observed. For the Ameland tidal inlet it corresponds to directions in a range from offshore to alongshore to the east. These winds, however, do not result in the conditions with the highest waves as it can be seen from the Figure 5b. Most of the waves originate from the north-northeast and southwest, meanwhile high waves with more than 4 m significant wave height originate mainly in the second quadrant (between north and west). This sector is not characterised by frequent events with high wind speed and observed wave conditions are mainly resulting from higher fetch length in this direction.

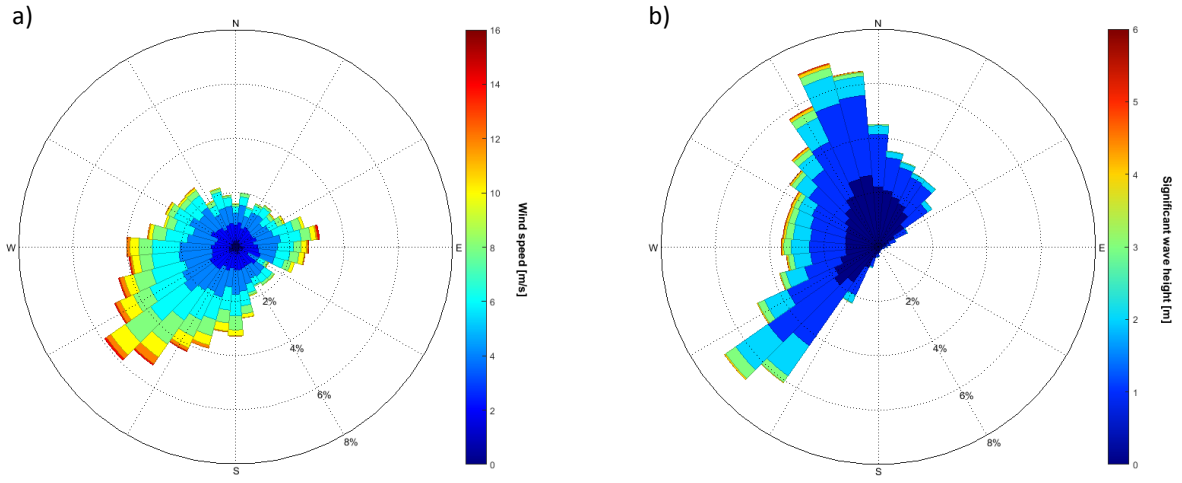

Figure 5 Wind rose for a period from 1994 to 2018 at KNMI weather station Hoorn (Terschelling) (a) and wave rose for a period from 1979 to 2018 at Eierlandse Gat wave station (b)

If we look at how significant wave height characteristics are distributed over the year (Figure 6), we can see clear seasonal pattern. During late spring and summer months wave height with exceedance probability of 10 % is less than 2 m and for 1 % - around 3 m, while during period from October until January wave height value is larger than 2.8 m more than 10 % of the time and larger than 4.5 m more than 1 % of the time. This means

that KG2 field campaign at the Ameland tidal inlet took place during high storm period, which can be important for interpreting data analysis and modelling results and making conclusions about net annual sediment transport at this location.

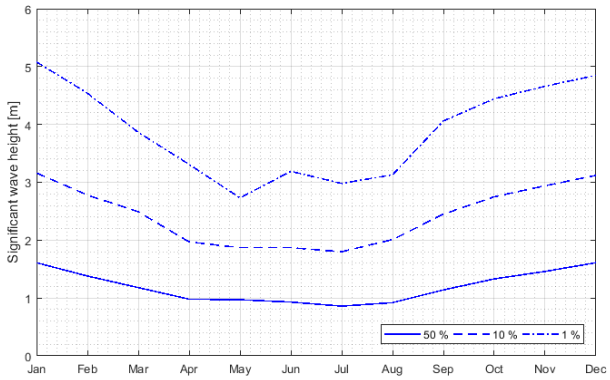

Figure 6 Monthly distribution of significant wave height with 50 %, 10 % and 1 % exceedance probability at Eierlandse Gat station

Cross-shore profile in this area is different from the profile that is usually observed for straight closed coast due to the presence of ebb-tidal delta associated with the inlet. Ebb-tidal deltas in general are characterised by low slopes (less than 1:1000) on top with inter- to supratidal sand bars dissected by ebb- and flood tidal channels. On the seaward side of ebb-tidal deltas slope becomes much steeper ranging from 1:1000 to more than 1:100, becoming less steep towards the -20 m depth contour.

2.2.2 HYDRODYNAMIC PROCESSES

In general, hydrodynamic processes can be classified into two major time scales. The first time scale corresponds to small scale variations due to individual short and infragravity waves with periods of less than 5 minutes (Figure 7), flow in this case is related to wave orbital velocities. The second time scale covers long period waves, which are characterized by variations on timescales from hours to days. Flow at this time scale is related to currents and variations are mainly caused by tidal action, however, there are also other processes that can alter tidal pattern of the currents. According to the forcing, we can distinguish wave-, wind- and density driven contribution to the currents. In order to analyse these contributions, tidal variation can be removed from the measured or modelled currents thus isolating the residual current. Residual current is usually characterized by much smaller magnitude than currents that develop due to tidal action, but at the same time they can play very important role for long-term sediment transport processes. Below a general description of wave-, wind- and density driven currents will be given and their influence on resulting picture of currents will be discussed.

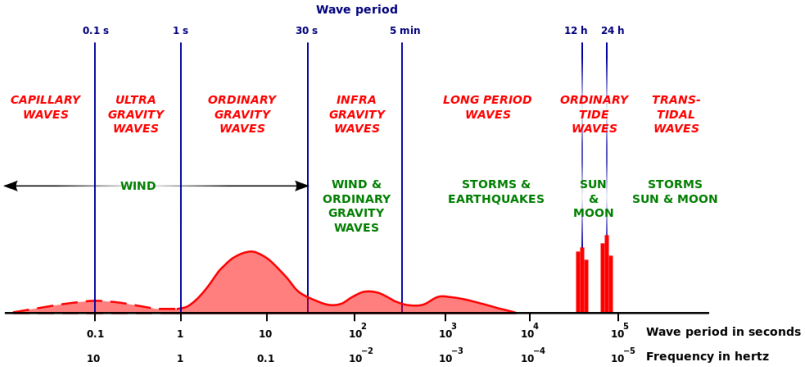

Figure 7 Classification of ocean waves according to wave period

WAVE-DRIVEN CURRENTS

Wind waves in the coastal zone can typically be divided into two groups: short waves, with periods less than approximately 30 seconds, and infragravity waves, which are oscillations with periods between 30 seconds and 5 minutes. Short waves are also divided into local wind waves and swell waves, which are generated by wind fields far away and travel over long distances, not associated with local wind conditions. Wave-induced currents include currents due to wave breaking and near-bed streaming.

Breaking of the individual waves starts when the wave grows in height and its steepness exceeds a certain critical value. Breaking can generally divided into three main types depending on steepness of the waves and slope of the shoreface: spilling, plunging and surging breaking. Spilling breaking is dominant in case of high wave steepness and mild bottom slope, whereas plunging breaking is dominant in case of low wave steepness and steep bottom slopes. For the first approximation of the wave height in the zone of wave breaking a simple expression $H_s = \gamma h$ can be used, where H_s denotes significant wave height, h - water depth and γ – dimensionless wave breaking coefficient. The values of γ vary for different types of breaking, according to Van Rijn (2013) for the onset of breaking for irregular waves γ is about 0.3 to 0.4. For spilling breaking values of γ are typically between 0.4 and 0.6. Combing this relation with the linear wave theory shoaling model the location of the breaker point can be estimated for some typical wave conditions. Using this method and assuming coefficient γ equal 0.4, waves will start breaking at the landward boundary of the lower shoreface at water depth of 8 m when their height will exceed 3.2 m, which corresponds to a storm event with 1 % exceedance frequency. For a typical 0.1 % storm, when the wave height at deep water is around 5.5 m, wave breaking will begin at water depth of around 12.5 m. From this estimation we can conclude that during fair weather conditions wave breaking will only be present in the surf zone and lower shoreface will be affected mainly during storm conditions. This means that, at least for a certain period of time, lower shoreface will also be influenced by the currents that develop due to wave breaking. Wave breaking and associated energy dissipation leads to gradients in the radiation stress, which drives set-up of the mean water level, generating an offshore directed undertow (Figure 8) and the longshore current (Figure 9).

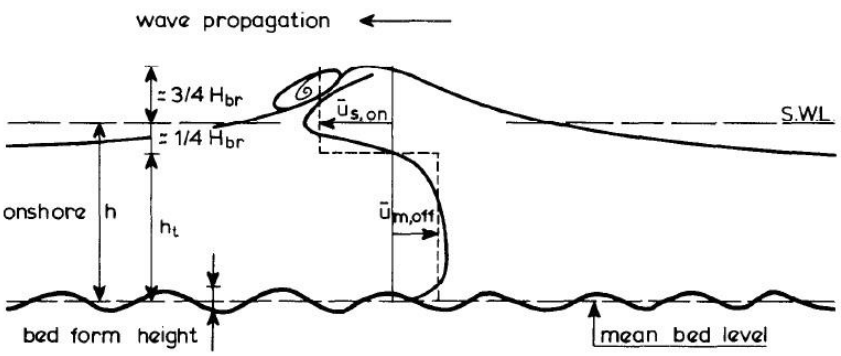

Figure 8 Net cross-shore velocities in breaking waves (Van Rijn, 1993)

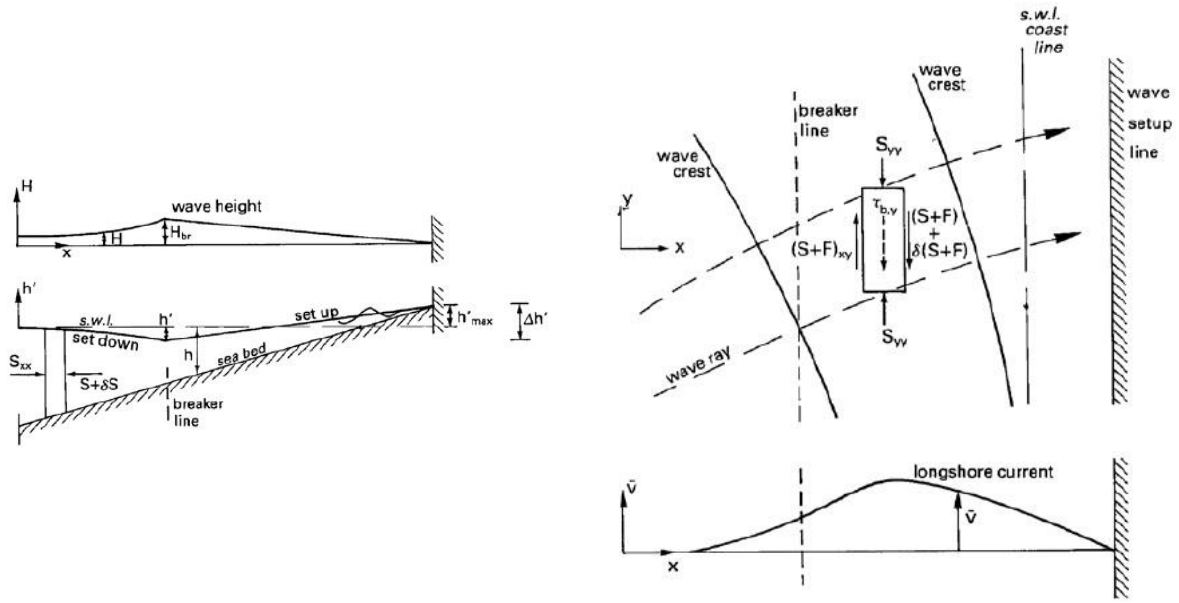

Figure 9 Wave-induced water level variation and longshore current in the surf zone (Van Rijn, 2013)

Another process that can contribute to the cross-shore sediment transport is generation of the near-bed streaming induced by the waves. Stokes (1847) first pointed out that fluid particles do not describe exactly closed orbital trajectories in case of small amplitude waves propagating in a perfect non-viscous oscillatory flow. Because horizontal orbital velocity increases with height above the bed, particles at the top of the orbit beneath wave crest move faster in the forward direction than it does in the backward direction at the bottom of the orbit beneath a wave trough. As a result, the particles have a second-order mean Lagrangian velocity (called Stokes drift) in the direction of wave propagation. For waves propagating in a horizontally bounded domain the total volume flux over the water column is equal to zero, which leads to an onshore volume flux in the upper part balanced by a return volume flux in the near-bed region of the water column (Figure 10) requires the presence of a horizontal pressure gradient caused by water level set-up towards the coast.

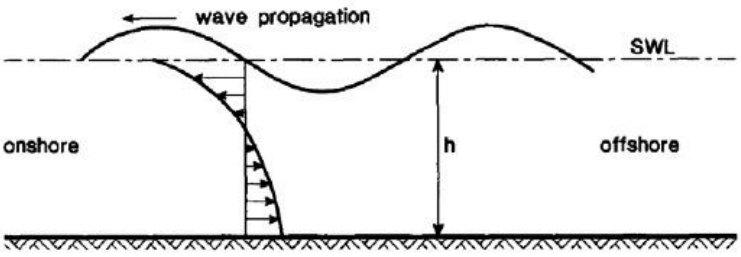

Figure 10 Drift velocity profile according to Stokes (Van Rijn, 2013)

Longuet-Higgins (1953) has shown that vicinity of the bed affects the phase of the horizontal and vertical orbital velocities, which leads to a time-averaged net downward transfer of momentum into the boundary layer by viscous diffusion causing a mean Eulerian flow in addition to the Stokes drift causing an onshore boundary layer current (progressive wave streaming) (Figure 11).

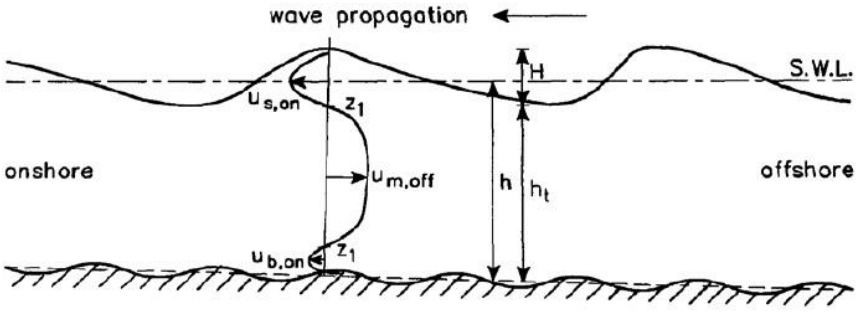

Figure 11 Average velocity profile according to Longuet-Higgins (Van Rijn, 2013)

WIND-DRIVEN CURRENTS

When the wind exerts a shear stress on the water surface in the coastal zone, upper layers of the water will start to move in the same direction as the surface wind stress. As a result, horizontal net flow in the longshore direction and, in case of close coast, wind-induced vertical circulation in the cross-shore direction is generated. The shore-normal component of the surface wind stress causes set-up or set-down of the mean water level at the shore. The proximity of the shoreline causes surface currents with shore-normal components to rapidly develop shore-normal pressure gradient, which leads to formation of an onshore or offshore bottom current (Figure 12) (Niedoroda, et al., 1985). The Coriolis effect can also result in additional set up of the water level or cause a set down depending on the orientation of the coastline relative to the wind. In case when the wind is directed parallel to the coast, a longshore current is generated. The vertical distribution of the wind-generated current largely differs from the current, generated by a water level gradient. The highest flow velocities occur near the surface rapidly decreasing in the downward direction (Figure 13). During storms the wind stress may have an important effect on the residual longshore current. The morphological impact of this longshore current, however, is limited due to relatively small velocities near the bottom, where the highest sediment concentrations are observed.

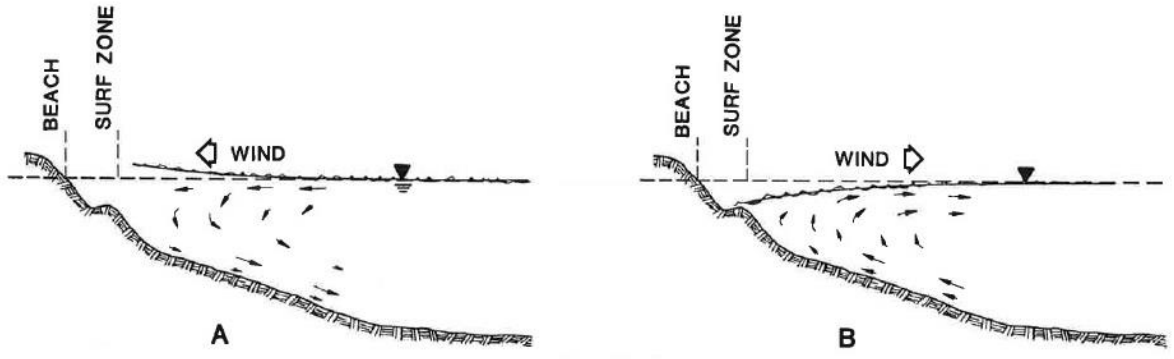

Figure 12 Cross-shore and vertical wind-driven currents in the friction-dominated zone: a. downwelling; b. upwelling (Niedoroda et al., 1985)

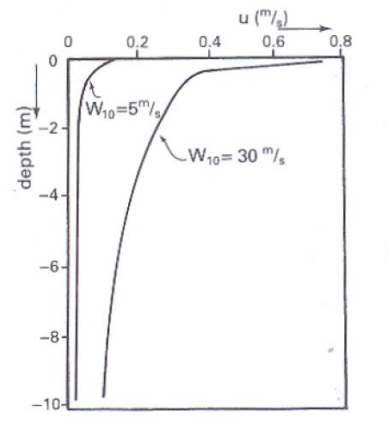

Figure 13 Typical velocity distribution for wind-driven current (Van Rijn, 2013)

DENSITY-DRIVEN CURRENTS

Density-driven currents are related to spatial density gradients of the fluid-sediment mixture due to variations of temperature, salinity and/or sediment concentration. Density variations induced by salinity in the coastal zone are most commonly the result of lower density fresh water river outflow into saline sea water characterized with higher density. The presence of this salinity gradient leads to formation of horizontal and vertical circulation. The density gradient effect is most pronounced in the near-bed region increasing onshore near-bed velocities during flood and reducing offshore near-bed velocities during ebb. As a result, a landward near-bed residual current is generated, which may cause a net landward transport of sediments, while near the water surface residual flow is in the seaward direction (Van Rijn, 2013). For the Dutch coast the major source of fresh water is the outflow of the rivers Rhine, Meuse and Scheldt. Most of the water is discharged through Schaar van Oude Doel, Maassluis and Haringvlietsluizen in the Delta area in the southwestern part of the Dutch coast, and through Ijmuiden in the central part of the Holland coast. However, significant part of the water from the Rhine is also flowing into the lake IJssel, from which it is discharged into the North Sea though the outlet sluices of the Afsuitdijk. These sluices, located near Den Oever and Kornwerderzand, are also shown in Figure 4, which can also impact hydrodynamics at the Ameland tidal inlet.

2.2.3 LOWER SHOREFACE SAND TRANSPORT PROCESSES

The sediment transport in the coastal zone can be divided in current- and wave-related. Current-related sediment transport corresponds to the mean currents such as tide-, wind- and density driven currents carrying the sediments in the direction of the main flow. Wave-induced transport processes are related to the oscillating and mean current generated in the wave boundary layer by high frequency waves. According to Van Rijn (1997), the sediment transport mechanisms related to waves include:

- wave orbital motion stirring sediment particles generating a suspension with large near-bed concentrations and increasing bed shear stress
- longshore-directed transport due to generation of longshore wave-driven current due to breaking waves
- net offshore-directed transport due to generation of a net return current (undertow) in the near-bed layers balancing the onshore mass flux
- bound long waves, which can be pictured as a local set down in water level where traveling in a wave group the short waves are small and set up where the waves are high, resulting in offshore flow where the wave are high and onshore – where they are low and net offshore sediment transport.

- wave asymmetry effect, which is expressed in sharpening of wave crests and flattening of wave trough and higher wave orbital velocities in the wave propagation direction then in the opposite direction, resulting in the net sediment transport in the wave propagation direction.
- net onshore directed transport due to generation of a Longuet-Higgins streaming current in the wave boundary layer

At the moment, the study of Van Rijn (1997) is the main study on the net annual sediment transport on the lower shoreface of the Dutch coast. In this study a sand budget model was developed for the Holland coast from Den Helder to Hoek van Holland between +3 and -20 m NAP based on computed sediment transport gradients in longshore and cross-shore direction and additional source/sink due to dredging and nourishment. Input sediment transport rates were computed using one-dimensional hydrodynamic and sediment transport model UNIBEST (Van Rijn et al., 1994) consisting of 3 sub-modules: wave propagation, vertical flow structure and sand transport models. The wave propagation model was used to derive the wave conditions at 20 and 8 m water depth based on offshore measurements. Vertical flow structure model was used to compute the vertical distribution of the flow velocities based on input depth-average velocity, wave and wind conditions and fluid density gradient taking into account the effects of wave breaking, Longuet-Higgins streaming and Coriolis effect. The sediment transport model computed bedload using the transport function of Ribberink (1997) using input currents and wave velocity data computed by the wave model. Suspended sediment transport was computed based on time-averaged velocity and sediment concentration profile (Van Rijn, 1993). Tidal-average sediment transport rates were calculated for a set of schematized wave and corresponding current conditions. The yearly transport was then determined as a sum of the tidal-average values weighted by the percentage of occurrence of each specific wave conditions.

Using this model, longshore and cross-shore sediment transport rates were computed at four cross-shore profiles: 14, 40, 76 (Noordwijk) and 103 km from Den Helder. As a result of the sensitivity tests, the dominant sediment transport mechanisms were determined (Table 2). From this table it can be seen that at 20 m water depth the net yearly transport is mainly determined by the fluid density gradient. It was concluded that the net onshore-directed bedload transport was dominant at 20 m, while the net suspended load transport was directed offshore. In the Table 3 the results of net annual sediment transport estimates are given for all four considered cross-sections, from which the average net onshore transport can be seen for three out of four locations at 20 m water depth, while at 8 m there is barely any net sediment transport, however, it can be also noted from the table that the uncertainty margins are rather large, such that the net transport can be high in either onshore or offshore direction.

Table 2 Contribution of various hydrodynamic processes to cross-shore transport rate (Van Rijn, 1997)

Process	Contribution to the cross-shore transport rate (in m^3/m/year)	
	depth = 20 m	depth = 8 m
Wave velocity asymmetry effect	0	15
Bound long wave effect	0	-15
Longuet-Higgins streaming effect	0	15
Reduced (50%) return current effect (related to breaking waves)	0	25
Fluid density gradient effect	10-25	10

Table 3 Best estimates of yearly-averaged total transport rates at a depth of 20 m and 8 m in profiles 14, 40, 76 and 103 (Van Rijn, 1997)

Cross-shore profile	Yearly-averaged total load transport (m^3/m/year)			
	cross-shore		longshore	
	depth = 20 m	depth = 8 m	depth = 20 m	depth = 8 m
14 Callantsoog	5±10	0±10	75±30	150±60
40 Egmond	15±10	0±10	60±25	135±50
76 Noordwijk	10±10	0±10	35±15	85±45
103 Scheveningen	0±10	0±10	25±15	65±40

2.2.4 CURRENTS AND SEDIMENT TRANSPORT NEAR TIDAL INLETS

The currents and the sediment transport mechanisms, which were described above, particularly return current due to wave- and wind-driven water level setup on the coast will be present mainly when the coast is closed. In case of the Ameland tidal inlet, however, these patterns cannot be applied. In this case waves will start breaking on the outer delta resulting in a net flow in the direction of the wave propagation, while the cross-shore component of the wind will also drive currents in or out of the Wadden Sea. However, the water level setup will still be present on the barrier islands of Ameland and Terschelling, which may lead to development of the water level gradient between the North Sea and the Wadden Sea, leading to an increased water inflow trough the inlet during rise of the storm (filling of the Wadden Sea basin) and outflow – after the storm (emptying). This, along with more large scale exchange between the North Sea and the Wadden Sea might also affect the currents on the lower shoreface. The impact of different forcing mechanisms on the currents and their relative importance for the net annual sediment transport on the lower shoreface of the Ameland tidal inlet will be analysed in the following chapters using the measurement from the KG2 field campaign as well as by the means of hydrodynamic and sediment transport modelling.

3. DATA AND METHODOLODY

In this section of the report, the data on currents, collected during the KG2 field campaign at the Ameland tidal inlet will be described in detail, including configuration of the measurement frames, their locations and ADCP measurement settings. Besides that, processing of the data will be described as well as the approach and methods that will be used for the data analysis. After that, an offline sediment transport modelling approach proposed by Deltares (Grasmeijer, 2018) will be presented as well as its components: TSAND model for calculating sediment transport rates, DCSM-FM hydrodynamic model (Zijl et al., 2018) for providing input currents, and Wave Transformation Tool (de Fockert et al., 2011) for determining the wave conditions. After that, procedure, which will be used to analyse applicability of the offline approach for the lower shoreface of the Ameland tidal inlet will be discussed. This will include additional validation of the hydrodynamics in the DCSM-FM model, which in its turn will also allow to analyse the effect of waves on the lower shoreface currents, and assessment of the input data impact on predicted sediment transport rates. Finally, approach that will be used to assess contributions of different physical mechanisms, such as Longuet-Higgins streaming, Stokes drift, wave velocity asymmetry and wind-driven currents, for the sediment transport on the lower shoreface will be presented.

3.1 FLOW VELOCITY DATA FROM THE KG2 FIELD CAMPAIGN

The KG2 measurement campaign at the Ameland tidal inlet consisted of two stages: during the first stage of the campaign measurements were conducted in the tidal inlet channel and at the upper part of the outer delta. For this, five measurement frames were deployed on August 29 and retrieved on October 9, 2017. During the second stage, measurements were conducted on the lower shoreface of the Ameland tidal inlet, where three measurement frames were placed at water depths of approximately 20, 16 and 11 m (Figure 14) for the period from November 8 until December 11 of 2017.

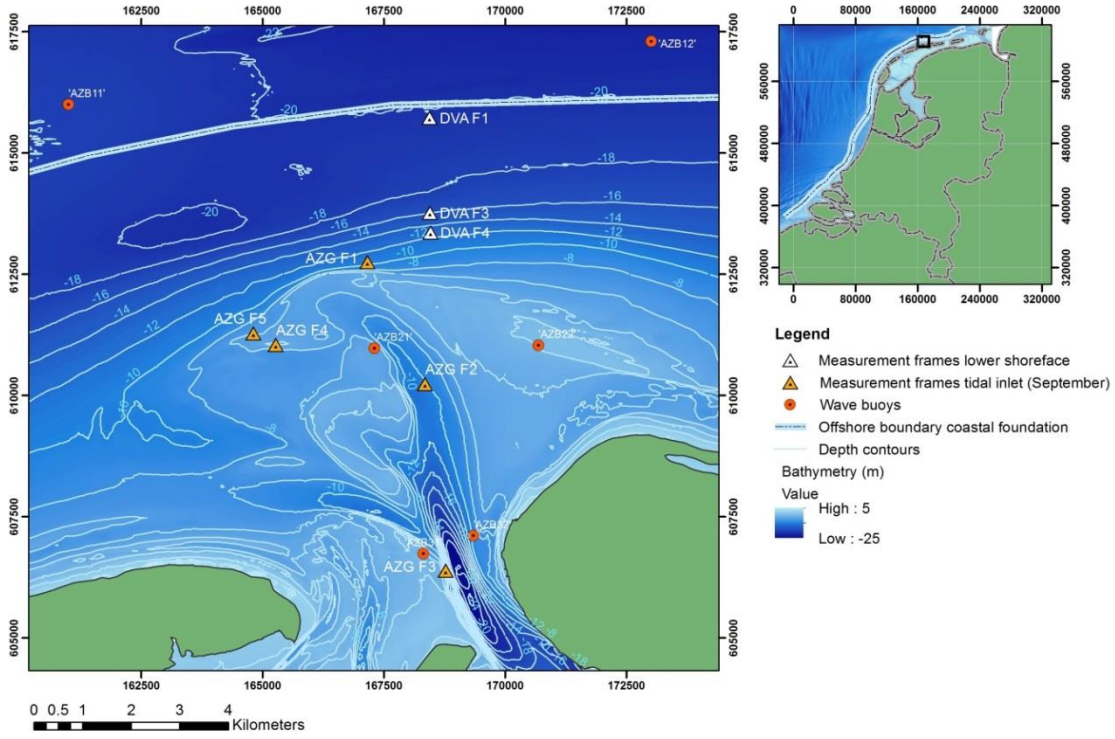

Figure 14 Locations of the measurement frames during the field campaigns at Ameland tidal inlet

Within the scope of this master thesis project, which focuses on studying of the hydrodynamic and sediment transport processes on the lower shoreface, analysis of the velocity measurements from the frames of the November campaign was performed, i.e. DVA F1, F3 and F4 .

3.1.1 INSTRUMENTS AND FRAMES CONFIGURATION

All the frames were equipped by several instruments for measuring different hydrodynamic and sediment transport characteristics. The overview of all the velocity measuring instruments along with position of their sensors above the bed is given in the Table 4 and configuration of the frame DVA F3 is shown in Figure 15. All the frames during field campaign, except frame DVA F4, were equipped by an upward and downward looking acoustic Doppler current profilers (ADCP) for recording the currents, two acoustic Doppler velocimeters (ADV) connected to four optical backscatter sensors (OBS) to measure wave orbital velocities and suspended sediment concentration. Besides that, frames were also equipped by multiparameter probe (MPP) for salinity, three-dimensional sonar ripple profiler (3DSRPLS) for small scale sea-bed bathymetry and optical laser diffraction instrument (LISST) for suspended load transport measurements. Frame DVA F4 on the lower shoreface due to the lack of instruments did not include ADV and OBS, instead, it was equipped by additional downward looking ADCP. For the velocity measuring instruments, position of the sensors above the bed, given in the table, does not correspond to the positon where the velocity itself was measured, these locations depend on the instruments settings, which will be presented below.

Table 4 Frames configuration and position in [m] of the instrument sensor above the bed

Instruments	Frame		
	DVA F1	DVA F3	DVA F4
ADCP upward	2.30	2.30	2.30
ADCP downward	0.48	0.47	0.48
extra ADCP downward	-	-	1.15
ADV1	0.65	0.65	-
ADV2	0.35	0.35	-

Figure 15 Frame configuration (photo from: Mol (2018))

3.1.2 VELOCITY MEASUREMENT SETTINGS

As the main focus of this project is on flow velocity measurements, measurement settings for ADCP and ADV instruments for all the frames will be described in detail. In the upper part of the water column velocities were measured by an upward looking ADCP TRDI WHM 600 or 1200 kHz in cells of 0.5 – 0.8 m. Blanking distance, which is the distance between the sensor of the instrument and the first measurement cell, was 0.5 – 1 m, which means that velocity measurements were available from 3.3 – 3.8 m above the bed. These measurements were done in bursts of 1 hour with 2250 measurements per burst and frequency of 1.25 Hz, which for every burst resulted in 30 minutes of continuous velocity recording and 30 minutes gap without measurements. Measurement settings for upward looking ADCP are presented in Table 5.

Table 5 Measurement settings for upward looking ADCP instruments during lower shoreface measurement campaign

Frame	DVA F1	DVA F3	DVA F4
Instrument	TRDI		
Type	WHM600		WHM1200
Blanking distance [m]	0.8		
Distance between bins [m]	0.8	1	0.5
Number of bins	34	0.8	0.5
Burst length [sec]	3600	30	34
Sampling frequency [Hz]	1.25		
Measurements per burst	2250		

Velocities near the bed were measured by Nortek Aquadopp HR in 13 cells of 0.03 m and in burst of 30 min with 6960 measurements per burst and frequency of 4 Hz, yielding for every burst 29 min of continuous measurements and 1 min gap without measurements. Measurement settings for downward looking ADCP are presented in Table 6.

Table 6 Measurement settings for downward looking ADCP instruments during lower shoreface measurement campaign

Frame	DVA F1	DVA F3	DVA F4
Instrument	Nortek		
Type	Aquadopp HR		
Blanking distance [m]	0.05		
Distance between bins [m]	0.03		
Number of bins	13		
Burst length [sec]	1800		
Sampling frequency [Hz]	4		
Measurements per burst	6960		

ADV instruments were available only for two frames (DVA F1 and DVA F2) and had the same settings at both of them: two ADV instruments at each frame measured flow velocities at 0.19 and 0.49 m from the bed in bursts of 30 min with 28640 measurements per burst and frequency of 16 Hz, resulting in continuously recorded velocities for 29 min 50 s with 10 s gap without measurements in every burst. These settings for ADV instruments are also presented in Table 7.

Table 7 Measurement settings for ADV instruments

	ADV1	ADV2
Instrument	Nortek	
Type	Vector	
Distance from the bed sensor [m]	0.65	0.35
Distance from the bed measurement [m]	0.49	0.19
Bursts [sec]	1800	
Frequency [Hz]	16	
Measurements per burst	28640	

Servicing of the frame DVA F3 was performed on November 16 around 14:00 for about 1 hour. During this servicing the frame was retrieved and then redeployed again within 10 meters from its original position. Positions of the instruments and their settings were not changed. Servicing on frames DVA F1 and F4 was not performed.

3.1.3 DATA OVERVIEW

With the frames locations, configuration of the instruments on the frames and their settings given above, the available velocity measurements data from the Ameland tidal inlet field campaign can be summarized in a cross-shore coastal profile shown in Figure 16. The bed level, which is presented on the figure, was determined from the interpolated Baseline bathymetry data set. From this figure it can be seen how the frames are distributed over the shoreface profile. Except for the gap of 2.3 – 2.8 m between upward and downward looking ADCP instruments, velocity measurements cover almost the entire water column with more detailed data being available for the 0.5 m layer near bed. Within this layer also ADV instruments were located, which recorded flow velocities at higher frequency. However, as the focus of this project is on currents and not on wave orbital velocities and because for large parts of the data from the ADVs were missing, these measurements were not used in the analysis. Besides that, it was found during the data processing that the upward looking ADCP at frame DVA F4 did record velocities only until November 29, so at this frame full velocity profile can be analysed only for a period of 20 days, instead of 32 days at frames DVA F1 and F3.

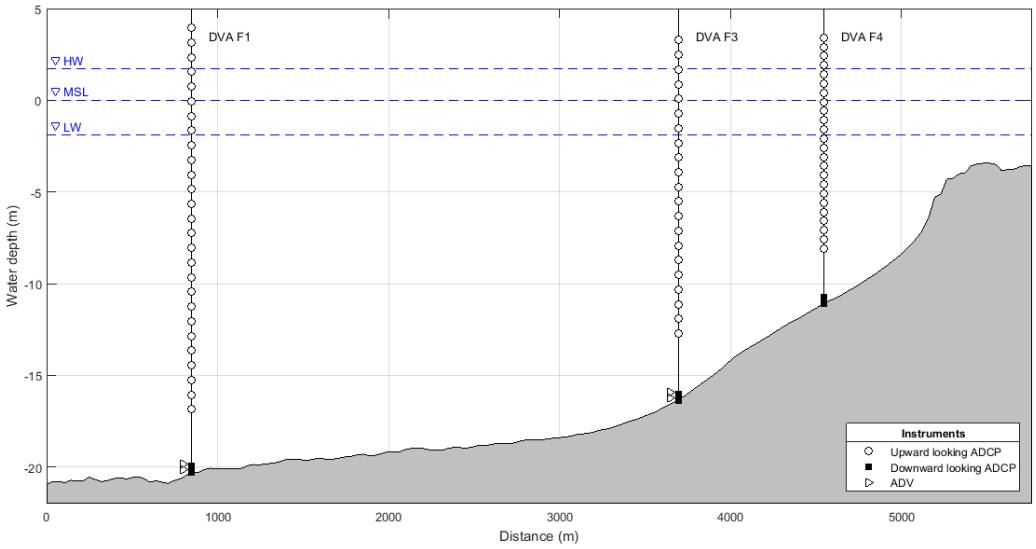

Figure 16 Cross-shore coastal profile at the Ameland tidal inlet with locations of velocity measurements

3.2 PROCESSING AND ANALYSIS OF THE DATA

3.2.1 DATA PROCESSING

Prior to the analysis of the currents, some initial processing had to be performed on the raw velocity data that was obtained from the ADCP instruments. This included removing outliers from the data and transformation of the measured velocities from instrument coordinates into geographic coordinates. Raw data processing was done by Floris de Wit, TU Delft PhD student working within the scope of SEAWAD research project. For despiking a MATLAB function based on the phase-space method by Goring and Nikora (2002) (Mori et al., 2007) was applied in order to find outliers, which were then replaced by linearly interpolated values. Coordinates conversion was done using heading values, which represent deviation between ADCP's main axis orientation and magnetic north and are recorded by the instrument along with the velocities. In geographic coordinates, velocities are presented in east-north-up plane (ENU).

For the analysis of the currents on the lower shoreface the most convenient way is to distinguish between longshore and cross-shore components of the currents. In case with the lower shoreface of the Wadden coast the coastline is interrupted and for the location offshore of the tidal inlet the longshore and cross-shore directions are harder to define as there is no "coast" in the usual sense. From the bathymetry and from the orientation of the dominant tidal currents, which will be demonstrated in the following chapter (Figure 35), it can be seen that away from the ebb-tidal delta the both have an orientation approximately west-east. Towards the shallow water both bathymetry and currents have a small inclination in the clockwise direction, but, for convenience, within this report, currents in west-east direction will be referred to as longshore currents and cross-shore currents will correspond to the currents is south-north direction. Positive values will denote currents to the east and to the north for longshore and cross-shore currents respectively. True current direction can be within 10 degrees from the measured direction as correction of the data for compass deviation has not been carried out. It can be corrected using the heading correction data, however, it is available only for frames F1 and F3 but not for frame F4.

All the results, presented in the following sections of this report, are obtained for the measured flow velocities averaged over a period of 10 minutes. The time-averaging was done by integrating the velocities over the 10-minute time periods. For short periods with missing data, velocities were linearly interpolated and if the velocities were measured for less than half of the time during period of averaging, these time moments were excluded from the analysis. Depth-average velocities are obtained by integrating these 10-minute average velocities over the water column including measurement from both upward and downward looking ADCP instruments.

3.2.2 METHODS TO ANALYSE RESIDUAL CURRENTS

In order to estimate residual currents and investigate smaller low frequency variations, high frequency tidal currents need to be removed from the data. This can be done using several different methods: by integrating currents over tidal cycle, by determining dominant tidal components from harmonic analysis and subtracting predicted tidal current from original data or by applying certain low-pass filter to the data in either time or frequency domain. These methods and their limitations are analysed below in more detail in order to determine which of them is most suitable to apply to the available lower shoreface velocity data. The aim is to obtain time-series of residual currents both depth-averaged and at different distances from the bed, as well as the vertical structure of residual currents. Subsequently, it will be studied how are these are affected by wind and wave conditions, how these change in cross-shore direction and these imply for the sediment transport on the lower shoreface.

INTEGRATION OVER TIDAL CYCLE

One of the methods how residual current can be determined is by integration of the instantaneous currents over a tidal cycle. However, the main disadvantage with method is that it is not clear what should be taken as the duration of the tidal cycle. In the paper of Duran-Matute and Gerkema (2015) several possible definitions are given for analysing residual flow in a multiple-inlet system of the Wadden Sea. For the currents on the lower shoreface, tidal cycle duration can be taken either as constant value corresponding to the dominant tidal component, which in case of the Dutch coast is M2 (12 h 25 m), time between alternate mean water level crossings and time between alternate moments of slack water. However, there are several issues that limit application of this method for available velocity measurements. From the data it can be seen that tidal cycle duration is varying, so using constant value might be inaccurate. Also, during storm events currents can be significantly distorted, which is especially important for the currents in Y direction and in the part of the water column near the bed, where they are relatively low. Because of this, it becomes hard to identify the tidal pattern and, consequently, calculate the residual velocity. Besides that, moments of slack water slightly vary over the water column, which does not allow constructing a residual current profile for a particular moment in time.

LOW-PASS FILTERING IN TIME DOMAIN

Another method that can be used to damp high frequency tidal motions is application of a certain weighted average low-pass filter to the original velocity time-series. These filters are based on sequence of $(2\mathrm{m}+1)$ weight factors:

$$W_{-m}, W_{-(m-1)}, \dots, W_{-1}, W_0, W_1, \dots, W_m \quad (1)$$

which have to satisfy two requirements: weight factors have to be symmetric ($\mathrm{W}_{-\mathrm{m}} = \mathrm{W}_{\mathrm{m}}$) and sum of all the values has to be equal to one. The output signal after applying the low-pass filter is then determined as:

$$y(t_n) = \sum_{k=-m}^{m} W_k x(t_{n+k}) \quad (2)$$

where $y(t_n)$ – filtered signal at time moment t_n, which is equal to a sum of $(2\mathrm{m}+1)$ weight factors multiplied by unfiltered signal values x for time moments from t_{n-m} to t_{n+m}. Different low-pass filters can be distinguished based on the following characteristics: time length of the filter, which is equal $2\mathrm{m} * \Delta\mathrm{t}$ and cut-off frequency, which defines the transition between stopband at high frequencies and passband at low frequencies. Overall performance of a particular low-pass filter can then be estimated using the filter response factor, which indicates the output amplitude of the signal of particular frequency when an input signal of the same frequency has unit amplitude. In literature large number of the low-pass filters with different properties can be found, an overview of different filter types is given in the papers of Thompson (1983) and Shirahata et al. (2016). One of the most commonly known low-pass filters is the of Godin (1972), which consists of successive use of a 24-hour running mean applied on the data time-series once and a 25-hour running mean applied twice. This filter performs well for removing diurnal, semidiurnal and shorter-period components, but it has a very slow transition from stopband to passband, which results in significant reduction in the output residual currents for periods between several days and a week (Shirahata et al., 2016). Better results for estimating residual current are observed for 241-hour-long low-pass filters based on “120i913” filter of Thompson (1983), which show entire removal of semidiurnal and diurnal tidal components and a very sharp transition from stopband to passband. However, for the available velocity time-series from Ameland inlet these filters are not applicable as it is only about 33 days long and 241-hour-long filter will result in data loss for 5 days at each end of the time-series, which accounts for almost one third of the entire data set. Because of that, based on the overview of Shirahata et al. (2016), 119-hour-long Lanczos-cosine filter with Hanning window and cut-off frequency of 40 hours “119Hanncos40h” was selected as a best alternative to compare

with other methods for estimating the residual currents. This filter also shows good results in filtering high frequency variation and data loss is twice smaller than for "120i913" filter, however, the transition between stopband and passband is then less steep. For the sake of comparison, Godin low-pass filter will also be used as it is one that is most well-known.

LOW-PASS FILTERING IN FREQUENCY DOMAIN

An alternative way to eliminate high-frequency tidal signal from the measured data is to convert it to a frequency domain using Fourier transform, from which residual currents can be found by applying a low-pass filter on data in frequency domain. In general, data filtering in the frequency domain can be described by the following equation:

$$Y(f) = R(f)X(f) \tag{3}$$

where $X(f)$ is the output of Fourier transform applied to the original data $x(t)$ multiplied with a frequency response factor $R(f)$ to obtain $Y(f)$. Filtered time series $y(t)$ is then recovered through an inverse Fourier transform. Frequency response factor $R(f)$ in this expression is defined in order to eliminate selected ranges of frequencies from the data. For an ideal low-pass filter, all the coefficients above selected cut-off frequency are set equal to zero and below – to one. This, however, causes ringing through the entire data set (Figure 17) and, to avoid that, frequencies are reduced from unity to zero over a range of frequencies (Walters and Heston, 1982). Besides that, Fourier transform treats the data outside the record as if it were zero and these abrupt changes from zero to nonzero values at the beginning and end of the time series can also cause ringing in the filtered data (Gibbs phenomenon) (Thompson and Emery, 2014). This effect can be reduced by applying a tapper function to the initial data time series, however, still certain part of data must be discarded at both ends of the resulting time series. A disadvantage of this method is that the amount of discarded data, unlike when low-pass filter is applied in time domain, is not well defined. For the analysis of the available data from the Ameland tidal the approach presented in the report of Burau et al. (1993) was followed by applying a cosine bell tapper to 40 hourly data points on each end of the data record (Figure 18a), which is approximately 10% of the time series. The data, affected by the taper, was then removed from the filtered results. Also, a cosine taper between specified stop frequency of 30 hours and pass frequency of 40 hours was used in order to reduce the effect of ringing in the filtered results (Figure 18b). Stop frequency of 30 hours was chosen in order to completely exclude diurnal and semi-diurnal tidal variation from the time series. In order to assess sensitivity of the results to different stop and pass frequencies, filtered currents were calculated for values from 25 to 40 hours with 10 hour transition to pass frequency, which all appeared to be very close to each other and it was decided to keep the value of 30 hours for the stop frequency.

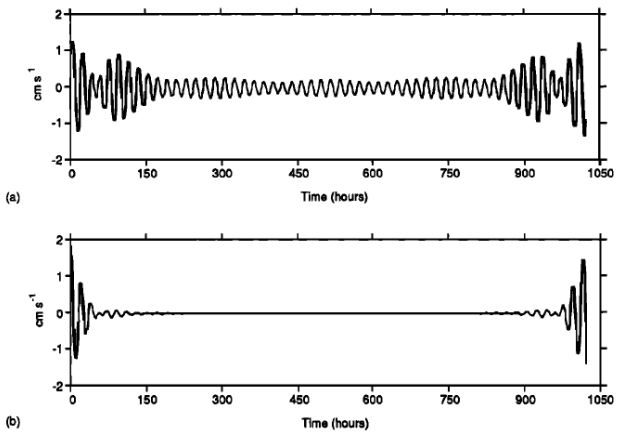

Figure 17 Example of ringing effects in the artificial time series (frequency of 0.05 cph) after applying Fourier transform low-pass filter with more sharp (a) and more gradual (b) transition between the stop and pass frequency (Forbes, 1988)

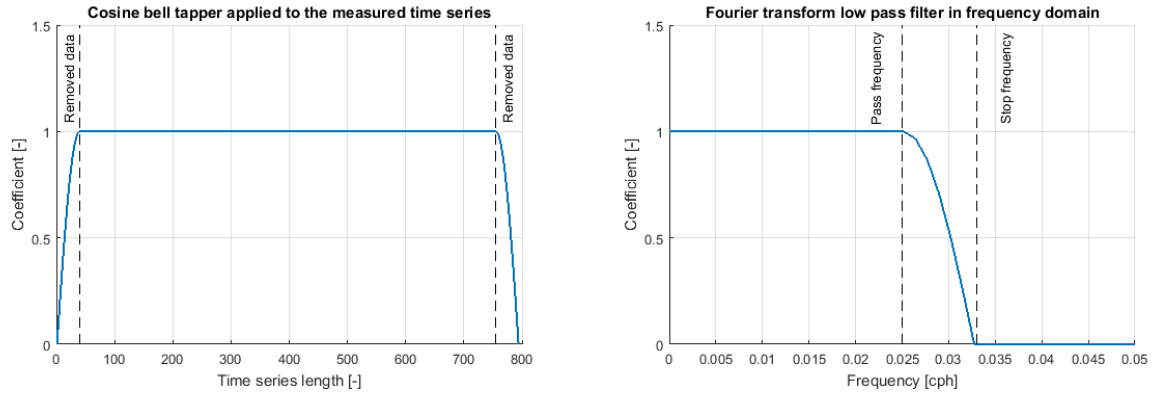

Figure 18 Fourier transform filter functions: cosine bell tapper applied to the time series (a) and low-pass filter in frequency domain (b)

HARMONIC ANALYSIS

Also, residual current can be found by determining the dominant tidal constituents at particular frequencies and then subtracting harmonically predicted time series from the original data. In order to apply this method, T_TIDE package for MATLAB was used (Pawlowicz et al., 2002). In this package, amplitudes and phases of different astronomical and shallow-water tidal constituents, arranged in descending order of their equilibrium amplitudes, are estimated based on the least square fit. After the fit has been performed, various corrections are applied and statistically significant constituents are selected based on 95 % confidence intervals and signal-to-noise ratio. Detailed description of this package is given in the paper of Pawlowicz et al. (2002). The main distinction of this method in comparison with Fourier transform low-pass filter, which eliminates all variation from the data above certain frequency, is that filtering only tidal components at particular frequencies allows to retain high-frequency residuals. However, a problem with this method is that the number of constituents that can be estimated from velocity time series depends on the record length, as for shorter time series frequencies of some major constituents are very close to each other and the confidence intervals for their solutions will be very large. Inclusion of tidal constituents in the analysis in T_TIDE uses the Rayleigh separation equation:

$$|\sigma_1 - \sigma_2|T > R \tag{4}$$

where σ_1 and σ_2 - frequencies, T – record length and R – Rayleigh constant, which is typically set to 1. Because of this, for frames F1 and F3, at which recorded velocity time series had a length of 33 days, it was possible to estimate amplitude and phase of 35 tidal constituents, while for the frame F4, at which upward looking ADCP recorded only for 21 days, the number of estimated constituents was limited to 17. Besides the number of constituents, record length also determines the accuracy of the estimated components as for short time series confidence intervals for minor components can become very broad. These two factors can be particularly important for the results of the tidal signal filtering by using harmonic analysis. Some results of harmonic analysis results from T_TIDE will also be presented in the following chapter.

COMPARISON OF DIFFERENT METHODS

Comparison of residual current estimates, determined using different methods that were described above, are shown in Figure 19. Also, assessment of filter performance and comparison between different filters can be done based on the filter response factor, which can be calculated as relation between filtered and original data in frequency domain. Frequency response factors of different filtering methods are presented in Figure 20. From these figures it can be seen that Godin filter indeed has a very slow transition between stopband and

passband and because of this residual current variation is significantly reduced compared to the "119Hanncos40h" and Fourier transform filters, which have much sharper cut-off. Residual currents determined using these two filters are very close, Fourier transform filter is characterised by slightly lower attenuation of the low-frequency variations then "119Hanncos40h" due to slightly lower cut-off frequency and sharper transition from stopband to passband. With both filters there is some data loss at both sides of time-series, but for Fourier transform filter this loss is smaller, 3.3 days instead of 5 for "119Hanncos40h" filter. Also, this figure illustrates well the high frequency residuals that remain in the residual signal if the method based on T_TIDE harmonic analysis. As a result, considering everything mentioned above about different methods, Fourier transform filter was selected for further analysis of the measured currents as it provides better generalization of the residual current.

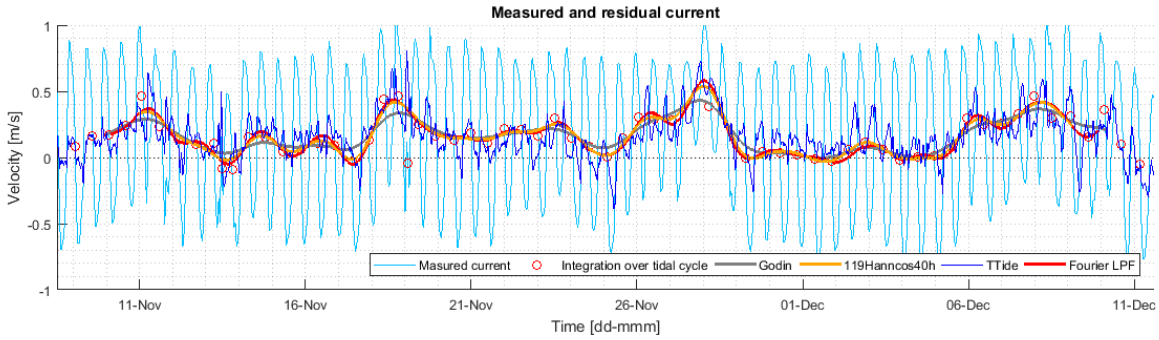

Figure 19 Comparison between different methods for estimating residual current (longshore velocity at frame F3, 6.9 m from the bed)

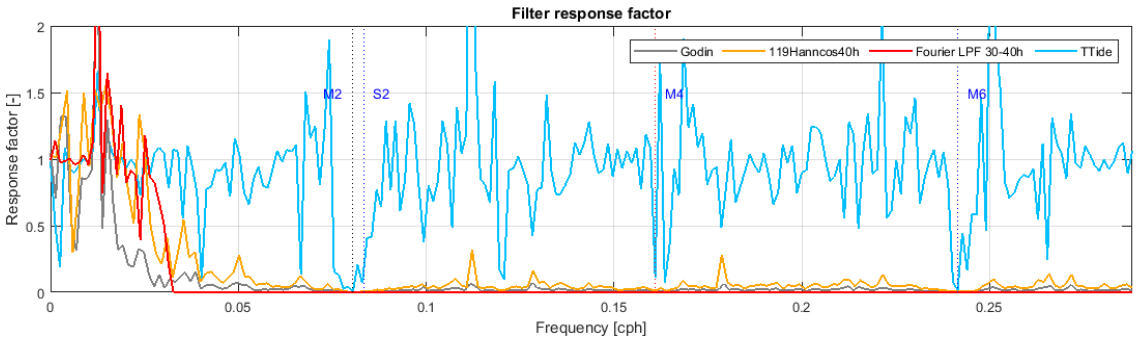

Figure 20 Frequency response of different filtering methods (longshore velocity at frame F3, 6.9 m from the bed)

3.3 OFFLINE SEDIMENT TRANSPORT MODELLING APPROACH AND TSAND MODEL

In order to assess annual sediment transport rates on the Dutch lower shoreface a so-called offline approach, proposed by Grasmeijer (2018), will be used. Within this approach, bed load and suspended sediment transport is computed using the TSAND model with current profiles and wave conditions as input. The main advantage of this method is that it is relatively fast and allows to assess relative importance of different physical mechanisms for sediment transport on the lower shoreface. This can be done by providing the transport model with different input for the currents, wave conditions or by changing analytical expressions for wave skewness, asymmetry and wave-induced streaming within the transport model itself. In the following section, the TSAND transport model will be described. After that, the methods to obtain the transport model input currents and wave conditions will be presented.

The TSAND model is a simplified sand transport model developed by Grasmeijer (2018) for tidal flow with waves based on detailed sediment transport formulations of Van Rijn (2007a,b) for suspended and bed load sediment transport, which have been extensively verified and are implemented in the Delft3D model.

3.3.1 SUSPENDED LOAD TRANSPORT

Current-related suspended sand transport in the model is calculated from integration of velocity and sand concentration profile over water depth:

$$q_{s,c} = \sum_{a}^{h} (u c_{sand})\, dz \tag{5}$$

where a – reference height above the bed, h - water depth, z – height above the bed, u – current velocity and c_{sand} – sand concentration, which is represented as:

$$c_{sand} = c_{a,sand} \left[\left(\frac{h-z}{z} \right) \left(\frac{a}{h-a} \right) \right]^{ZS} \tag{6}$$

with $c_{a,sand} = 0.15 p_{sand} f_{silt} (d_{50}/a)(T^{1.5}/D_*^{0.3})$ – reference sand concentration withp_{sand} – fraction of sand, $f_{silt} = d_{sand}/d_{50}$ – silt factor (= 1 if $d_{50} > d_{sand}$), d_{50} – mean particle diameter, $D_* = d_{50}\left((s-1)g/v^2\right)^{1/3}$ – dimensionless particle size, T – dimensionless bed shear stress parameter (Van Rijn, 2007b) and ZS – dimensionless suspension number of sand. Suspension number in this expression is determined as follows:

$$ZS = \frac{w_{sand,0}}{\beta k u_{*,cw}} + 2.5 \left(\frac{w_{sand,0}}{u_{*,cw}} \right)^{0.8} \left(\frac{c_{a,sand}}{c_0} \right)^{0.4} + \left(\frac{\rho}{\rho_{fresh}} - 1 \right)^{0.4} \tag{7}$$

where $w_{sand,0}$ – fall velocity of a single sand particle based on mean diameter based on formula of Van Rijn (1993), $\beta = 1 + \left(w_{sand,0}/u_{*,cw} \right)^2$ – coefficient with maximum of 1.5, $k = 0.4$ – von Karman constant, $u_{*,cw} = \left(u_{*,c}^2 + u_{*,w}^2 \right)^{0.5}$ – bed shear velocity due to currents and waves, $u_{*,c} = \left(\tau_{b,c}/\rho \right)^{0.5}$ and $u_{*,w} = \left(\tau_{b,w}/\rho \right)^{0.5}$ – current- and wave-related bed shear velocity respectively $c_0 = 0.65$ – maximum bed concentration, ρ – water density and $\rho_{fresh} = 1000\ kg/m^3$ – density of fresh water. Current- and wave-related bed shear stress is computed as:

$$\tau_{b,c} = \frac{0.16\rho (v_{10})^2}{\left(\log(30 * 0.1h/k_{s,c}) \right)^2} \tag{8}$$

$$\tau_{b,w} = 0.25 \rho f_w U_w^2 \tag{9}$$

where $f_w \exp\left(-6 + 5.2 \left(A_w/k_{s,w} \right)^{-0.19} \right)$ – wave-related friction coefficient, $k_{s,c}$ and $k_{s,w}$ – current- and wave-related roughness, which are determined using roughness predictor of Van Rijn (2007b), v_{10} – velocity magnitude at $0.1h$, U_w – peak near-bed orbital velocity and A_w – peak near-bed wave orbital excursion.

Suspended sediment transport due to wave asymmetry in the direction of wave propagation is calculated using the following equation:

$$q_{s,w} = \gamma_s \frac{U_{w,for}^4 - U_{w,back}^4}{U_{w,for}^3 + U_{w,back}^3} * \int_o^h c_{sand}\, dz \tag{10}$$

where $\gamma_s = 0.1$ – coefficient for wave-related transport, $U_{w,for}$ and $U_{w,back}$ – near-bed peak orbital velocities in the wave direction and in the opposite direction, which are computed using method of Isobe-Horikawa modified by Grasmeijer (2003) using the following expression:

$$\frac{U_{w,for}}{\hat{U}} = 0.5 + \left(\left(\frac{U_{w,for}}{\hat{U}}\right)_{max} - 0.5\right)\tanh\left(\frac{\left(\frac{U_{w,for}}{\hat{U}}\right)_a}{\left(\frac{U_{w,for}}{\hat{U}}\right)_{max}}\right) \quad (11)$$

where $\hat{U} = 2rU_w$ – sum of the $U_{w,for}$ and $U_{w,back}$, which is defined as peak near-bed orbital velocity U_w multiplied by a factor $r = -0.4 * H/h + 1$. This equation is solved for $U_{w,for}$ using maximum skewness $\left(U_{w,for}/\hat{U}\right)_{max}$ and $\left(U_{w,for}/\hat{U}\right)_a$ defined as follows:

$$\left(\frac{U_{w,for}}{\hat{U}}\right)_{max} = -2.5 * \frac{h}{L} + 0.85 \quad (12)$$

$$\left(U_{bw,for}/\hat{U}\right)_a = -5.25 - 6.1\tanh\left((-0.0049(t_1)^2 - 0.069t_1 + 0.2911)u_1\right) \quad (13)$$

with $t_1 = T_p\sqrt{gh}$ and $u_1 = \hat{U}/\sqrt{gh}$, where T_p – peak wave period. Velocity in the opposite direction is then determined using expression $U_{w,back} = \hat{U} - U_{w,for}$. Time duration over the wave period when the orbital velocities are in the direction of wave propagation t_{for} and in the opposite direction t_{back} are then determined using expressions $t_{for} = (U_{w,back}/(U_{w,for} + U_{w,back})) * T_p$ and $t_{back} = T_p - t_{for}$.

3.3.2 BED LOAD TRANSPORT

The bed load transport in TSAND model was computed using method based on quasi-steady approach by Van Rijn (2007a), in which net bed-load transport is determined by time-averaging over the wave period of the instantaneous transport rate as:

$$q_b = \int_o^{T_p} q_{b,t}\, dt \quad (14)$$

where $q_{b,t}$ – intra-wave time-dependant bedload transport, which is related to the – intra-wave time-dependant bed shear stress as:

$$q_{b,t} = \gamma\rho_s f_{silt} d_{50} D_*^{-0.3}\left(\frac{\tau_{b,cw,t}}{\rho}\right)^{0.5}\left(\frac{\tau_{b,cw,t} - \tau_{cr}}{\tau_{cr}}\right)^n \quad (15)$$

where $\gamma = 0.5$ and n are calibration coefficient, ρ_s – sediment density, s – relative density, v – kinematic viscosity, τ_{cr} – critical bed shear stress and $\tau_{b,cw,t}$ – intra-wave time-dependent grain-related shear stress due to both waves and currents, which is calculated as:

$$\tau_{b,cw,t} = \rho f_{cw} U_{\delta,cw}^2 \quad (16)$$

where $U_{\delta,cw}$ – intra-wave near-bed velocity at the edge of wave bottom boundary layer and f_{cw} – grain friction coefficient due to currents and waves. This coefficient is defined by the following expressions:

$$f_{cw} = \alpha\beta f_c + (1 - \alpha)f_w \quad (17)$$

$$f_c = 8g/\left(18\log\left(\frac{12h}{k_{s,grain}}\right)\right)^2 \quad (18)$$

$$f_w = \exp\left(-6 + 5.2\left(\frac{A_w}{k_{s,grain}}\right)^{-0.19}\right) \quad (19)$$

where f_c and f_w denote current- and wave-related grain friction coefficients with $\alpha = u_c/(u_c + U_w)$ – relative strength of wave and current motion, u_c – depth-average current velocity, β – vertical velocity profile structure coefficient, $k_{s,grain} = d_{90}$ – grain roughness.

Intra-wave near-bed velocities at the edge of wave bottom boundary layer $U_{\delta,cw}$ are determined using the current velocity and values of $U_{w,for}$ and $U_{w,back}$, which were explained in the previous section. To calculate intra-wave velocities, first, wave time t_{wave} is determined by dividing peak wave period into 200 time steps. For these moments, time series of wave orbital velocities are calculated using following expressions:

$$\begin{aligned} u_{wave} &= U_{w,for} * \sin\left(\frac{t_{wave}}{t_{for}}\pi\right) && for\ t_{wave} < t_{for} \\ u_{wave} &= -U_{w,back} * \sin\left(\frac{t_{wave} - t_{for}}{t_{back}}\pi\right) && for\ t_{wave} \geq t_{for} \end{aligned} \tag{20}$$

These velocities are then added to the current velocity to obtain the total intra-wave velocity $U_{\delta,cw}$.

3.3.3 LONGUET-HIGGINS STREAMING

In the model there is an option to analytically compute streaming velocity based on the model of Davies et al. (1999) at the edge of wave boundary layer, which, in case if this option is activated in TSAND, is added to the current velocities at the reference level, which are used to compute bedload transport. This streaming velocity $\overline{U}_\delta$ is computed using the following equations:

$$\begin{aligned} \overline{U}_\delta &= -\frac{\left(U_{\delta,w}\right)^2}{c} && for\ \frac{A_{\delta,w}}{k_{s,w}} \leq 1 \\ \overline{U}_\delta &= \left(-1 + 0.875\log_{10}\left(\frac{A_{\delta,w}}{k_{s,w}}\right)\right)\frac{\left(U_{\delta,w}\right)^2}{c} && for\ 1 < \frac{A_{\delta,w}}{k_{s,w}} \leq 100 \\ \overline{U}_\delta &= 0.75\frac{\left(U_{\delta,w}\right)^2}{c} && for\ \frac{A_{\delta,w}}{k_{s,w}} > 100 \end{aligned} \tag{21}$$

where c – wave celerity, $U_{\delta,w}$ – peak wave orbital velocity and $A_{\delta,w}$ – peak wave orbital excursion at the edge of bottom boundary layer.

3.4 TSAND TRANSPORT MODEL INPUT

As it was already mention above, input data for the transport model consists out of two major parts: wave conditions and currents. For the period when the KG2 field campaign on the lower shoreface took place, measured currents and wave conditions can be used to determine sediment transport, but in this case model results are limited to the 1 month period when the frames were installed and to their locations. In order to analyse sediment transport and its variability over a longer period in time and at different locations, and also to investigate dominant processes that can cause sediment transport on the lower shoreface, model results have to be used to obtain flow and waves input to the transport model. For these reasons, in the approach of Grasmeijer (2018) wave transformation table (de Fockert et al., 2011) is used to determine wave conditions and 3D Flexible Mesh Dutch Continental Shelf Model (3D DCSM-FM) (Zijl et al., 2018) is used to provide input flow conditions, which allows to estimate sediment transport at any location along the Dutch coast for any period for which model output is available. In this section of the report both wave transformation table and 3D DCSM-FM model will be described in more detail and results of 3D DCSM-FM model validation by currents that were measured during KG2 field campaign at Ameland tidal inlet will be presented.

3.4.1 WAVE TRANSFORMATION TABLE

Wave transformation table is a program for MATLAB, it was developed at Deltares by de Fockert et al. (2011) within the Building with Nature project and it allows to transform wave time series from permanent measurement stations located offshore of the Dutch coast to an arbitrary location nearshore. It is based on

wave time series measured at the stations IJmuiden, Eierlandse Gat and Europlatform in the period from January 1979 to December 2000. From this data a set of wave conditions was derived that was used to force a SWAN model in stationary mode, the results of which were then used to generate wave transformation matrix. This matrix consists of multiplication factors that specify the relation between the offshore and nearshore significant wave height and wave period and additional factors for the transformation of the wave direction and surge. The user input to the model is limited to XY coordinates of the output location nearshore, which should be located within the model domain, and begin and end time for the period of transformation. As a result, it provides time series for significant wave height, peak wave period, mean wave direction and surge at the closest grid cell to the specified location with a time step of 3 hours. At the Ameland tidal inlet grid size in the cross-shore direction increases seaward from 250 m near the inlet itself up to 700 m near the -20 m depth contour. In Figure 21 comparison between wave characteristics, measured by AZB11 wave buoy at approximately 20 m water depth, and wave transformation tool output. From this figure it can be seen that predicted significant wave height and wave direction values are very close to the measured data, while measured peak wave period is often higher compared to the wave transformation tool results, which can be caused by inaccuracies in measurements.

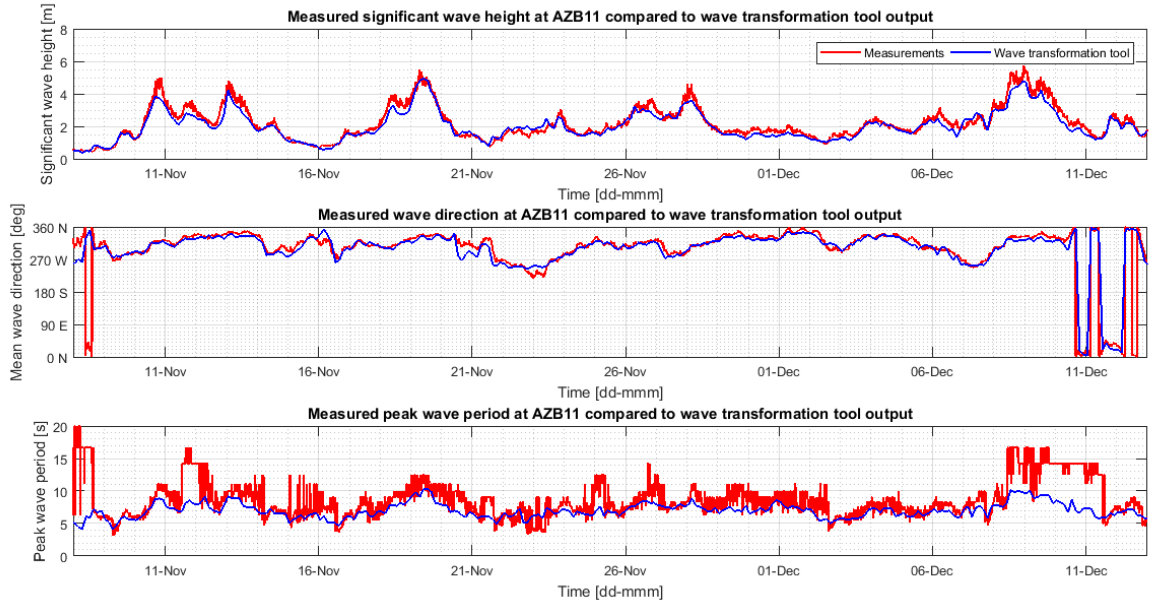

Figure 21 Measured wave conditions at wave buoy AZB11 compared with conditions predicted using wave transformation table for the period of the KG2 field campaign

3.4.2 DCSM-FM MODEL

The 3D DCSM-FM model was developed in D-HYDRO Flexible Mesh at Deltares by Zijl et al. (2018) based on previous generation WAQUA DCSMv6 model. It is a three-dimensional hydrodynamic model that covers the entire north-western part of the European continental shelf (Figure 22). The main advantage of this model compared to its predecessors is that it allows to better match resolution with relevant local spatial scales by using coarser grid at deeper areas and finer resolution at shallower areas near the coast, which leads to a factor 4 reduction in computational time. Model was developed with two grid configurations: “1 nm” and “0.5 nm”, the name of configuration corresponds to the highest horizontal grid resolution that is present in the model (“nm” stands for nautical mile, 1 nm equals approximately 1.8 km, 0.5 nm – 0.9 km). The network is refined in three steps by a factor 2 at approximately 800, 200, 50 and 12.5 m depth contour except for the

southern North Sea, where the area of highest resolution was expanded for better representation of this region in the model. The resulting network of 0.5 nm model configuration is also shown in Figure 22. For the vertical schematization sigma-layer approach was used, in this approach water column is divided into a fixed number of layer independent of the local water depth, which allows to have higher vertical resolution in shallow areas. For both 1 nm and 0.5 nm model configurations 20 layers with a uniform thickness of 5% were used.

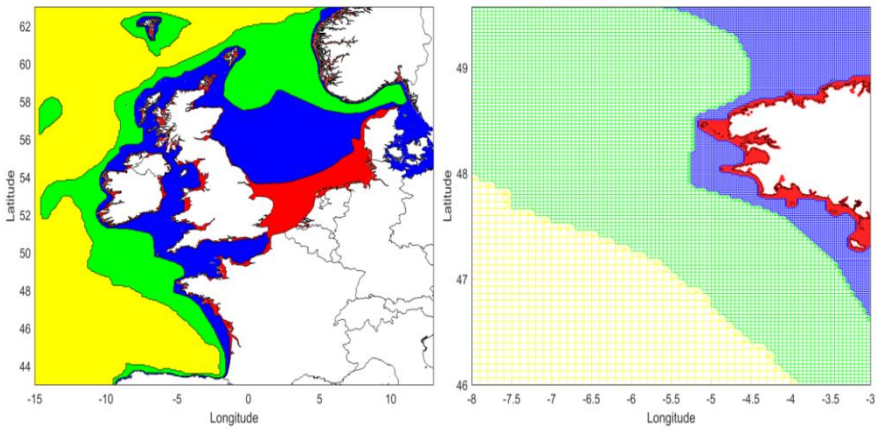

Figure 22 Overview (left) and detail (right) of 3D DCSM-FM model network (grid size: yellow – 4 nm, green – 2 nm, blue – 1 nm, red – 0.5 nm) (Zijl et al., 2018)

Bathymetry for the most part of the model was derived from gridded bathymetric dataset of the European Marine Observation and Data Network (EMODnet) and for the areas near the Dutch coast Baseline bathymetry data was used. Bathymetry points within the cell size radius of were averaged to determine model bathymetry at net nodes. Velocity points in the model are located on the grid cell edges and their depth is determined as the average between the adjacent net nodes. Water level points, at which output from the model observation points is given, are located on cell faces and their depth is determined as the maximum water depth among surrounding edges.

The 3D DCSM-FM model forcing includes meteorology, which is defined by air pressure and wind speed and direction on the surface, and river discharges flowing into the model domain. Processes, that are resolved in the model include salinity and temperature effects, however, model does not include wind-induced waves and, as a consequence, wave-driven contribution to the currents. For the input fresh water river discharges in the model, a database of climatological monthly mean discharges, predicted from European hydrological model E-HYPE, was used. For 6 out of total 895 E-HYPE locations, which include Den Oever, Haringvlietsluizen, Ijmuiden, Kornwerderzand, Maassluis and Schaar van Oude Doel and are most important for the Dutch coast, predicted discharges were replaced by the measured data for all the years. For the meteorological surface input wind speed and direction at 10 m above the surface and air pressure output from HIRLAM model version 7.2 was used, which has 11 km spatial resolution and hourly temporal interval. In Figure 23 comparison between meteorological characteristics measured at KNMI station Hoorn (Terschelling) and the data from HIRLAM database is presented. From this figure it can be seen that for air pressure and wind direction for most of the period HIRLAM prediction is very close to measured values, while for wind speed for this particular station it shows some overestimation by approximately 2 – 4 m/s. This might be caused by the fact that station Hoorn (Terschelling) is located on land, where wind speed is reduced due to friction, and this effect might be poorly captured in the HIRLAM model due to its coarse resolution. Small overestimation in wind speed of about 2 m/s is observed also for several other stations located offshore of the study area.

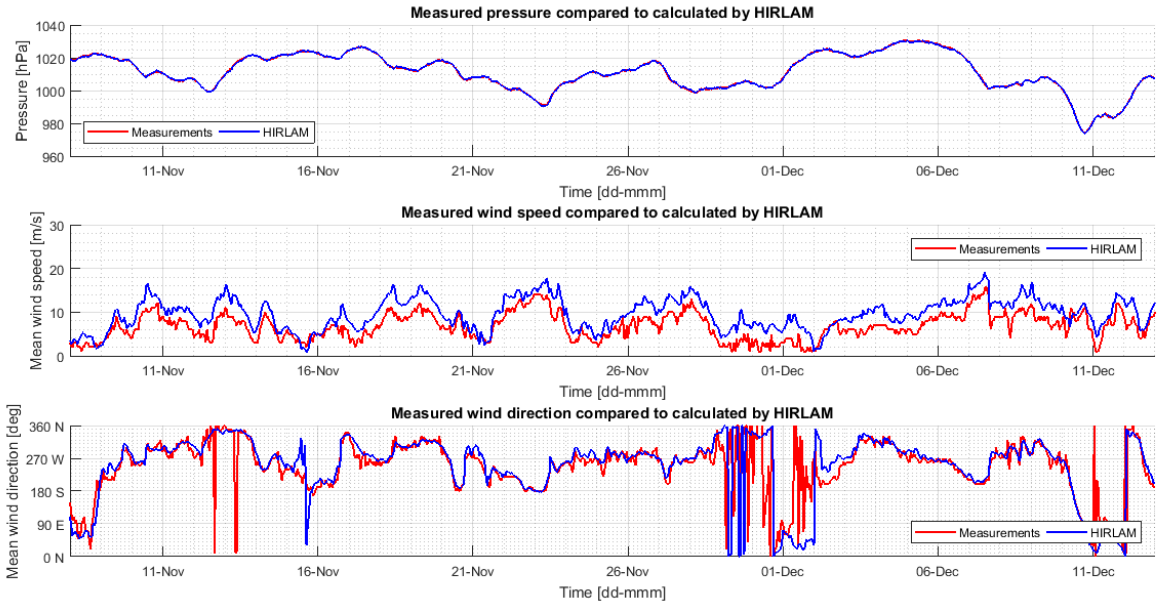

Figure 23 Measured meteorological characteristics at station Hoorn (Terschelling) compared with model input forcing derived from HIRLAM 7.2 for the period of the KG2 field campaign

The 3D DCSM-FM model was chosen for deriving input flow conditions for calculating sediment transport rates on the lower shoreface for several reasons. First of all, this is relatively fast 3D model that covers the entire Dutch coast, which means it includes all the locations of the KG2 field campaign so it can be validated by the new measurements and also allows to assess net annual sediment transport on the lower shoreface at multiple locations along the coast. Considering the computational time, on Deltares h6 cluster using 5 nodes with 4 cores each, 1 nm model configuration with maximum time step of 200 seconds requires 29 hours for 1 year of simulation, while 0.5 nm configuration with maximum time step of 120 seconds needs 79 hours for the same period. For spin-up from uniform initial conditions a simulation period of 1 year is used. Another advantage of the model is that it also includes effect of salinity on currents, which might be particularly important for the sediment transport, especially at the area of Holland coast. Besides that, an important factor is that DCSM model has already been used for several other studies.

Some validation of the model has also been done previously, including validation on water levels, temperature, salinity and flow velocities. Some of the validation results are also presented in the memo of Zijl et al. (2018). For the flow velocities validation was performed for the data from two buoys that recorded velocity profile at 23 and 24 m water depth offshore of Egmond. This data was compared with the output from both model configurations and it has shown that timing of the peak velocities is well reproduced by the model, but velocity magnitude is slightly overestimated. Best results were observed for depth-average values with RMSE between 0.06 and 0.09 m/s depending on the location and model configuration, while for currents near the bottom and near the water surface were reproduced less accurately with RMSE of 0.12 – 0.2 m/s. Also, some validation has been done on lower shoreface currents from KG2 campaign at Ameland tidal inlet, but it only included depth-average velocity magnitude and direction from upward looking ADCP. This comparison already showed that model gives relatively good results for the most seaward frame with RMSE for velocity magnitude of 0.08 m/s, while at two other frames velocity magnitude is systematically underestimated and RMSE equals 0.12 and 0.15 m/s. From the timings of the moments when the largest mismatch between data and the model is observed a conclusion was made that its cause is not tidal, but a more detailed analysis of the reasons for this mismatch was not carried out.

One of the main shortcomings of the model is its coarse resolution. In Figure 24 1 nm model configuration grid is shown along the bathymetry for the Ameland tidal inlet and it can be seen that, due to rather steep bed

slope on the seaward side of the ebb tidal delta, this grid cell covers the range of water depths from around 18 to 8 m and. As a result, the lower shoreface frames F3 and F4 in the model are located within the same grid cell, while from the measurements we can clearly see that current at these locations are significantly different. In Figure 25, which shows model grid for refined 0.5 nm configuration, two frames are located in different cells, but still single cell covers a range of water depths from 8 to 14 m. Because in the model bed level of the cell is defined as the lowest level of the cell edges, for the lower shoreface bed level in the model output will almost always be lower than real bed level at any location within the cell. From Table 8 it can be seen that for the frame F1 bed level in the model is closest to the measured data, as at this location slope is rather mild, while at two other locations there is considerable difference for both model configurations. For frame F4 there is significant improvement between 1 nm and 0.5 nm model configurations, but difference still remains very large. Another problem, which can result from the model resolution being too low, is that the Ameland tidal inlet itself is described in the model only by 3 cells in 1 nm version and by 6 cells in 0.5 nm version. Same is also the case for all other tidal inlets, which might result in the model not reproducing accurately large scale water exchange between the North Sea and the Wadden Sea.

Table 8 Deviation between measured bed level and bed level for the model velocity output

Frame	F1		F3		F4	
Bathymetry	Bed level [m]	Difference from measurements [m]	Bed level [m]	Difference from measurements [m]	Bed level [m]	Difference from measurements [m]
Measurements	-20.4	-	-16.4	-	-11.1	-
Model 1 nm	-20.2	0.2	-17.8	-1.4	-17.8	-6.7
Model 0.5 nm	-20.5	-0.1	-18.3	-1.9	-14.5	-3.4

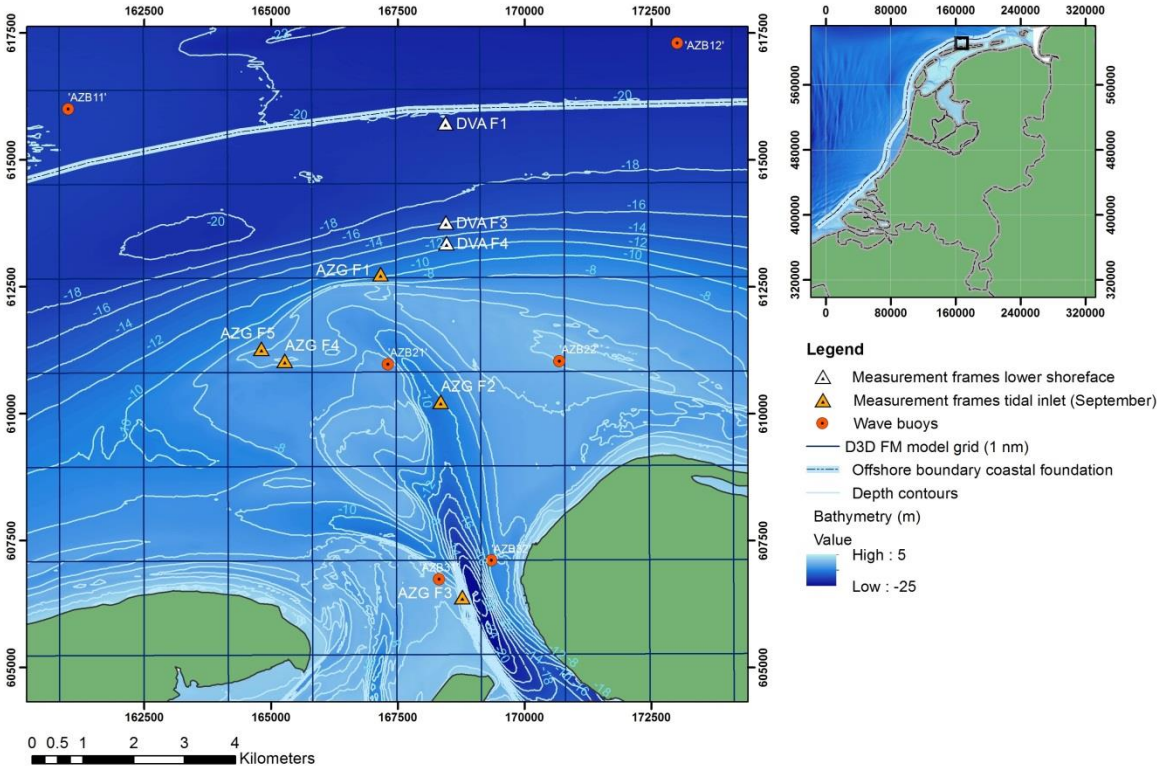

Figure 24 Model grid of DCSM-FM 1 nm configuration at the Ameland tidal inlet and locations of the KG2 frames

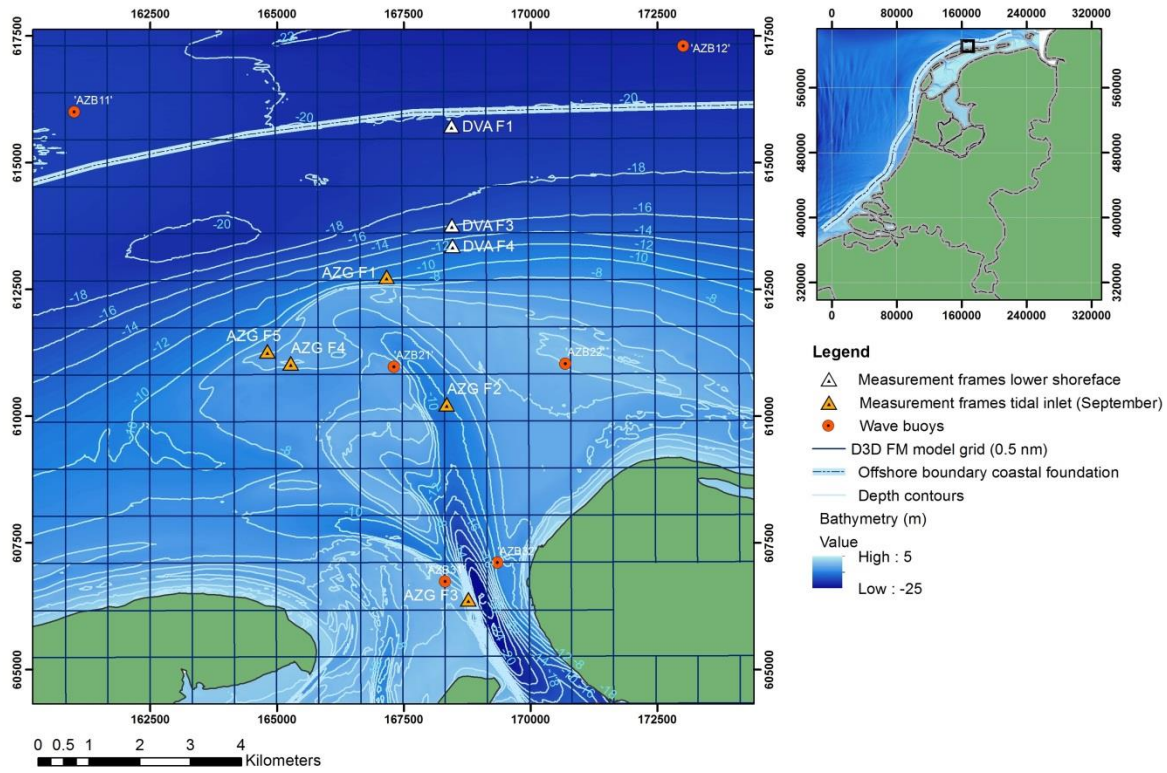

Figure 25 Model grid of DCSM-FM 0.5 nm configuration at the Ameland tidal inlet and locations of the KG2 frames

Also, in the model version that was used during validation by Zijl et al. (2018), discharge measurements for the freshwater inflow locations at the Dutch coast were not yet available for the year 2017. Because of that, less accurate monthly mean discharges, derived from E-HYPE database, were used, which might have resulted in additional mismatch when comparing modelled and measured currents from the KG2 frames at the Ameland tidal inlet. In the memo of Zijl et al. (2018) suggest to redo the validation once measured discharges become available as the outflow of the IJsselmeer may play significant role for the currents in area of interest. Another important factor, which can potentially lead to inaccuracy in predicted currents on the lower shoreface, is the fact that wave-driven currents are not included in the model simulation. These currents, which develop due to wave induced Stokes drift and near-bed streaming as well as wave breaking, are particularly important at shallower water. During storm events their influence can extend towards the lower shoreface as well. Such events do not occur frequently, but still they can play an important role for the sediment transport processes.

3.5 DELFT3D MODEL OF THE AMELAND TIDAL INLET

Parallel with the offline sediment transport modelling approach (Grasmeijer, 2018), which is used to analyse net annual sediment transport over the entire Dutch coast, within the scope of the of the KG2-DV subproject of Deltares a detailed model is developed for the area of the Ameland tidal inlet. The work on the model is performed by Kees Nederhoff, Reinier Schrijvershof, Pieter Koen Tonnon and Jebbe van der Werf and as of November 2018 the work is still in progress. Because of that, only a draft report on the model setup, calibration and validation is available (Nederhoff et al., 2018), however, there already are some model results, which will be also used in this master thesis report as they can help to interpret the results of the data analysis and the DCSM-FM model validation.

This detailed model of the Ameland tidal inlet, unlike the DCSM-FM model, includes the effects of waves on currents as it is a coupled Delft3D-FLOW and SWAN model and it directly computes the sediment transport using the full formulations of Van Rijn (2007a, b). Besides that, this model has much finer resolution in the area

of interest compared to the DCSM-FM, with resolution of the Delft3D-FLOW varying from 50 m near the tidal inlets to 350 m at the outer parts of the model domain (Figure 26). The SWAN grid has a factor 2 coarser resolution compared to the Delft3D-FLOW everywhere, except the area near the Ameland tidal inlet (red line in Figure 26), where a second nested SWAN domain is used with the same resolution as the Delft3D-FLOW. Currently, a 2DH version of the model is used, which assumes logarithmic velocity profile neglecting vertical distribution of the offshore-directed undertow and density-driven currents in order to maintain reasonable computational times and because these currents are not expected to be important for the offshore part of the Ameland tidal inlet (Nederhoff et al., 2018).

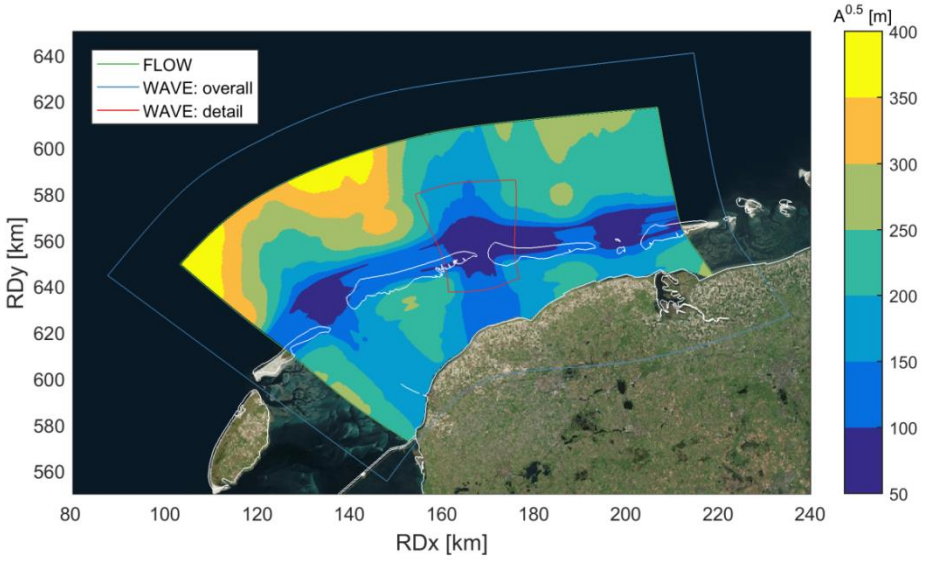

Figure 26 Extent of the model grids with the resolution of the FLOW grid indicated as the length [in m] of the grid cells (Nederhoff et al., 2018)

For the meteorological forcing of the model also a HIRLAM model dataset with resolution of 3 to 16 km was used. Boundary conditions of the model on water levels were derived from the DCSMv6ZUNOv4 model (Zijl et al., 2013), which allows to account for large-scale tidal and meteorological processes. Wave conditions at the boundaries were derived from the stations Schiermonnikoog-Noord (SON) and Eierlandse Gat (ELD). Calibration of the model was done in order obtain the best results for the year of 2017 using water level data form stations Terschelling Noordzee, Nes, Wierumgronden and Holwerd and wave data from 'AZB' buoys in the Ameland tidal inlet (Figure 4 in Chapter 2). Calibration of the currents was performed using the KG2 data from the September campaign at the Ameland tidal inlet. This data included discharges through the tidal inlet, measured on September 1, 5 and 19, currents from the measurement frames AZG F1, F3 and F4, located on the ebb-tidal delta and in the tidal inlet channel (Figure 14), and from the frames, that were installed in September on the watershed of the Ameland tidal inlet. Water levels were calibrated by applying a correction on the astronomical boundary conditions and varying Van Rijn roughness predictor and waves – by increasing the measured wave energy density at the boundaries and by changing the wave breaking formulations. The results of the calibration have shown that the calibrated model reproduces measured water levels with RMSE of 10 cm, velocities with RMSE of 15 m/s in the inlet and 10 m/s on the watershed. Waves at the offshore wave buoy AZB11 are reproduced with RMSE of 20 cm for wave height, 0.5 s for period and 20 degrees for direction. As a result, the model was concluded to be suitable for using the model further to study hydrodynamics and sediment transport on the lower shoreface of Terschelling and Ameland tidal inlet (Nederhoff et al., 2018).

3.6 MODELLING METHODOLOGY

In the previous sections all the components of the offline sediment transport modelling approach (TSAND, DCSM-FM and Wave Transformation Tool) were described in detail together with the coupled Delft3D and SWAN model of the Ameland tidal inlet, which is also developed at Deltares within the KG2-DV project. In this section a detailed methodology, which was used in order to answer the research question on the validity of the offline sediment transport modelling approach for predicting the sediment transport rates on the lower shoreface of the Ameland tidal inlet, will be presented. This will include description of particular steps that were taken for the validation of the hydrodynamics in the DCSM-FM model using the standard water level measurements as well as current and discharge measurements from the KG2 field campaign and for the analysis of the computed sediment transport rates. Also, methodology that was used for the analysis of the net annual sediment transport on the lower shoreface of the Ameland tidal inlet and contribution to the net transport of different physical mechanisms, such as wind-driven currents, wave-induced Longuet-Higgins streaming, wave velocity asymmetry and Stokes drift, will be presented in this section

3.6.1 VALIDATION OF THE OFFLINE SEDIMENT TRANSPORT MODELLING APPROACH

As it was partly mentioned in the Section 3.4.2, some validation of the DCSM-FM model by the KG2 lower shoreface currents at the Ameland tidal inlet was presented in the report of Zijl et al. (2018). However, it included only visual comparison of the depth-average velocity magnitude and direction, derived based only on the upward looking ADCP measurements, calculating the goodness of fit statistics for depth-average velocity magnitude and comparison of the time-average velocity magnitude profiles. Because of that, additional model validation was performed within this master project. Because the original DCSM-FM model resolution is low, the Ameland tidal inlet channel is described by only 3 grid cells in the 1 nm version and 6 cells – in 0.5 nm, while the offshore ebb-tidal delta slope, which is located between 10 and 20 m water depth, in certain areas is covered by only 1-2 grid cells (Figure 24 and Figure 25), in order to assess the effect of resolution on the model results at the Ameland tidal inlet, a refinement was done for the area of the Wadden Sea and the lower shoreface of the Wadden coast. Grid resolution in this area was increased by a factor 2, so in this report this new model version will be referred to as 0.25 nm model. New model grid in the study area is shown in Figure 27. In order to prevent the model from becoming unstable, maximum time step was also reduced from 120 to 60 seconds, which, along with increased number of grid cells, resulted in an increase of computational time from 79 up to 144 hours for 1 year of simulation. Besides refining the grid, bathymetry in the area offshore of the tidal inlet also was updated with the most recent data, as 1 nm and 0.5 nm versions at this location used bathymetry data from 2011, which was replaced by the bathymetry measurements, performed in 2017. Comparison of these two datasets is presented in Figure 28. From this figure it can be seen that significant changes occurred over a 6 years period. Old main ebb channel became shallower and the ebb-tidal delta near the area where the measurement frames were located moved seaward, leading to even larger steepening of its seaward slope. This new model version was also then validated with the same data as 1 nm and 0.5 nm models in order to compare how these changes in the bathymetry affect the model results. Besides that, an additional 0.5 nm model run was also done with updated bathymetry in order to assess the sensitivity of the results to only this factor.

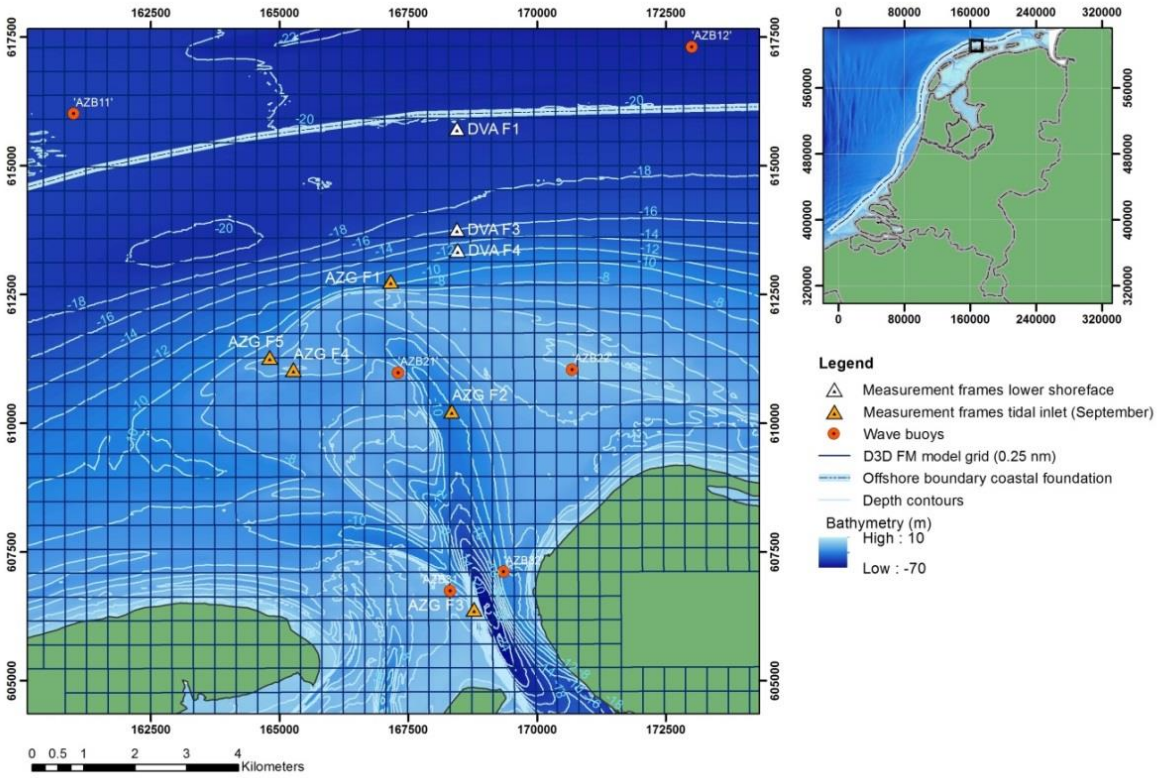

Figure 27 Grid of 3D DCSM-FM model locally refined at the Ameland tidal inlet

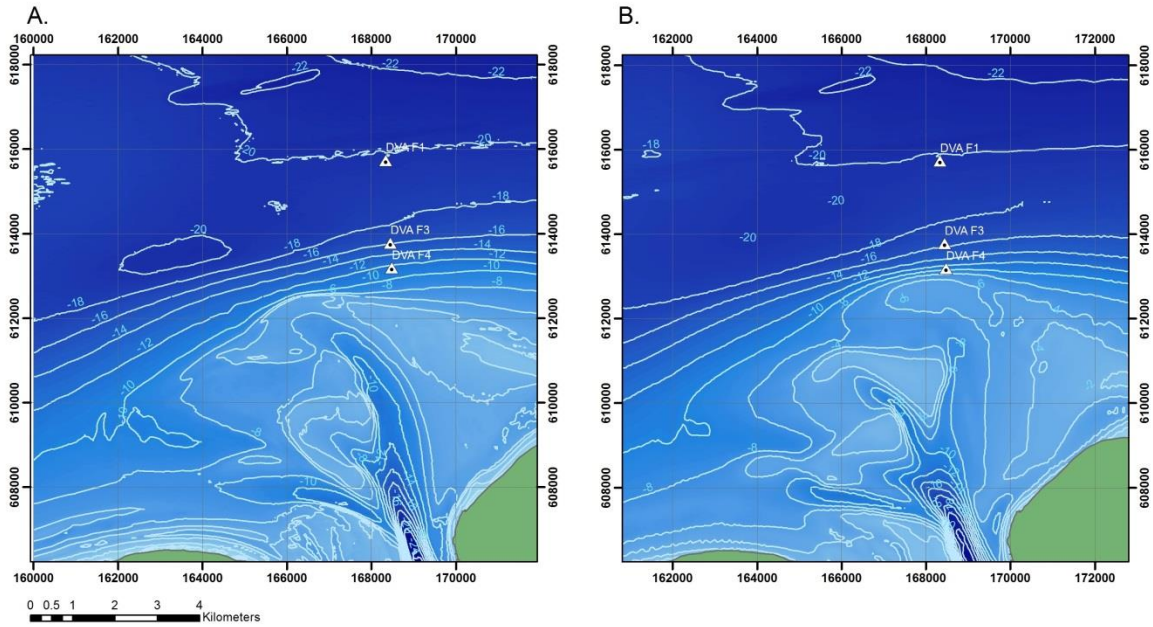

Figure 28 Comparison between bathymetry at the Ameland tidal inlet for year 2011 (A) and 2017 (B)

The results of different model versions were validated first by comparing measured and modelled water levels at stations Terschelling Noordzee and Nes, which are located in the North Sea and in the Wadden Sea respectively. The Terschelling Noordzee station was included in the validation of the model done by Zijl et al. (2018), while the station Nes previously was not taken into account. Validation of the water levels at both these stations, however, is needed in order to understand how well the exchange between the North Sea and the Wadden Sea is captured in the model, as this process can play an important role for the hydrodynamics on

the lower shoreface. Validation of the water levels was done by computing goodness of fit statistics, such as correlation coefficient (R), unbiased root-mean-square error (uRMSE) and bias, for both stations and for different model versions. For water levels uRMSE was used instead of ordinary RMSE, similarly to the report of Zijl et al. (2018), because the vertical reference of the model is not clearly defined as different systems are used in the EMODnet (LAT and MSL) and Baseline (NAP) bathymetry datasets. To analyse how well the model reproduces water level variation due to tidal action dominant tidal constituents were determined using T_TIDE and measured and modelled surge water levels were determined using Fourier transform low-pass filter. Besides water levels, exchange between the North Sea and the Wadden Sea was also validated by the discharges through the tidal inlet, which were measured for a one full tidal cycle during calm conditions three times within the KG2 field campaign in September 2017.

After that, the DCSM model was validated by the measured currents from the KG2 field campaign at the lower shoreface of the Ameland tidal inlet. Unlike the validation of Zijl et al. (2018), velocities were divided into two components in the longshore (east – west) and cross-shore (north – south) direction similarly to how the measured currents are analysed. Besides that, measured currents from the downward looking ADCP instruments were used together with the data from the upward looking ADCPs. The validation included calculating the goodness of fit statistics for the total currents as well as for only tidal currents determined from the measured and the modelled currents using T_TIDE in order to analyse how well only tidal currents are reproduced in the model. Statistics for the total currents were calculated for depth average currents and at several different layers in order to assess variation of the results depending on the distance above the bed. Velocity profiles were analysed for periods of calm and storm conditions in order identify the effect of storms on the measured velocity profiles and to analyse how well they are reproduced by the model. To analyse non-tidal variation in the currents, residual currents were determined for the modelled currents using Fourier transform low-pass filter and time-average velocity profiles in the longshore and the cross-shore direction were calculated. Based on the validation results for the water levels and the currents, a choice was made on which of the DCSM model versions will further be used for the analysis of the sediment transport on the lower shoreface. Additionally, in order to analyse the importance of wave-induced contribution to the currents on the lower shoreface and effects of the resolution on the DCSM-FM model results, measured depth-average currents were compared with the DCSM results and with the results of the detailed Delft3D model for the Ameland tidal inlet with and without waves, which also allowed to get a better understanding of the data.

At the next stage, the measured and modelled currents along with the wave conditions derived from the Wave Transformation Tool were provided to the TSAND sediment transport model in order to calculate the net longshore and cross-shore sediment transport rates over the period of the KG2 field campaign and analyse the effect of the data-model mismatch on the results. After that, the net sediment transport in the longshore and cross-shore direction was computed for different significant wave height classes in order to analyse corresponding transport magnitude and direction for every class and to identify which conditions contribute the most to the mismatch between the total net sediment transport in the longshore and the cross-shore direction. Contributions of the bedload and suspended load to net transport was also computed for the measured and the modelled currents in order to assess their role for the sediment transport on the lower shoreface and their role in the mismatch between the net transport results for the modelled and the measured currents. Finally, in order to make a conclusion about the validity of the offline sediment transport modelling approach for the lower shoreface of the Ameland tidal inlet, transport rates predicted for the period of the KG2 field campaign from the measured currents were compared with yearly cross-shore and longshore transport rates derived from the DCSM model currents. Sensitivity of the results to varying mean grain diameter was analysed by calculating sediment transport rates for the period of the field campaign and net annual sediment transport with the grain diameter values of 200, 250 and 300 µm.

3.6.2 SEDIMENT TRANSPORT PROCESSES

In order to analyse contributions of the Longuet-Higgins streaming, Stokes drift and wave velocity asymmetry to the net annual sediment transport on the lower shoreface, sediment transport rates were calculated using TSAND for the period of the field campaign and for each year between 2013 and 2017 with and without these processes included. Calculating sediment transport rates and contribution of different mechanisms for the period of the field campaign from the measured and the modelled currents was done in order to analyse the effect that wave-driven currents have on the results and, based on that, determine if the conclusions about different processes can be made for the net annual sediment transport rates based only on the modelled currents. To assess the effect of the Longuet-Higgins streaming, additional current velocities were calculated using the equation (21) presented in the Section 3.3.3, which were then added to the input currents for calculating the bedload sediment transport. The additional suspended sediment transport due to wave asymmetry was computed using the equation (10), which was presented in the Section 3.3.1. The potential additional transport due to Stokes drift was calculated by adding a Stokes drift velocity profile, determined using the equation (25) in the Section 6.2 to the velocities that are used for computing suspended sediment transport. To analyse the contribution due to wind-driven currents, an additional 0.5 nm DCSM model run without wind was made for the year of 2017. Only one year was taken due to limitations in time, as one full year with a spin-up period required about 8 days of simulation, and in the amount of model simulations that can be done at the same time.

4. DATA ANALYSIS RESULTS

In this section of the report the results of the velocity data analysis will be presented. First, it will include a brief look into wind and wave conditions, measured during the period of the field campaign, in order to relate wind speed and direction with the observed waves and to distinguish storm events that can potentially affect the currents on the lower shoreface. After that, tidal and residual currents on the lower shoreface will be analysed along with their vertical structure in order to investigate how currents vary in time, at different distances from the bed and between different locations in cross-shore direction. Based on this, a conclusion will be made on how the currents on the lower shoreface are influenced by storms and whether wave-induced currents are observed in the data for the period of measurements.

4.1 WIND AND WAVE CONDITIONS

In order to investigate the effects of storm events on the currents, additional data over wind and waves is necessary. In this section characteristics of the wave and wind conditions that were observed at the Ameland tidal inlet during KG2 field campaign will be given as well as their correspondence to regular wind and wave conditions, which were analysed in Chapter 2. Wind data for the period of the field campaign was taken from the KNMI weather station #251 Hoorn (Terschelling) and wave characteristics were derived from the wave buoy 'AZB11', which is located to the west of the most seaward frame of the field campaign at water depth of about 20 m. Locations of the weather station and wave buoy are shown in Figure 4 in Chapter 2.

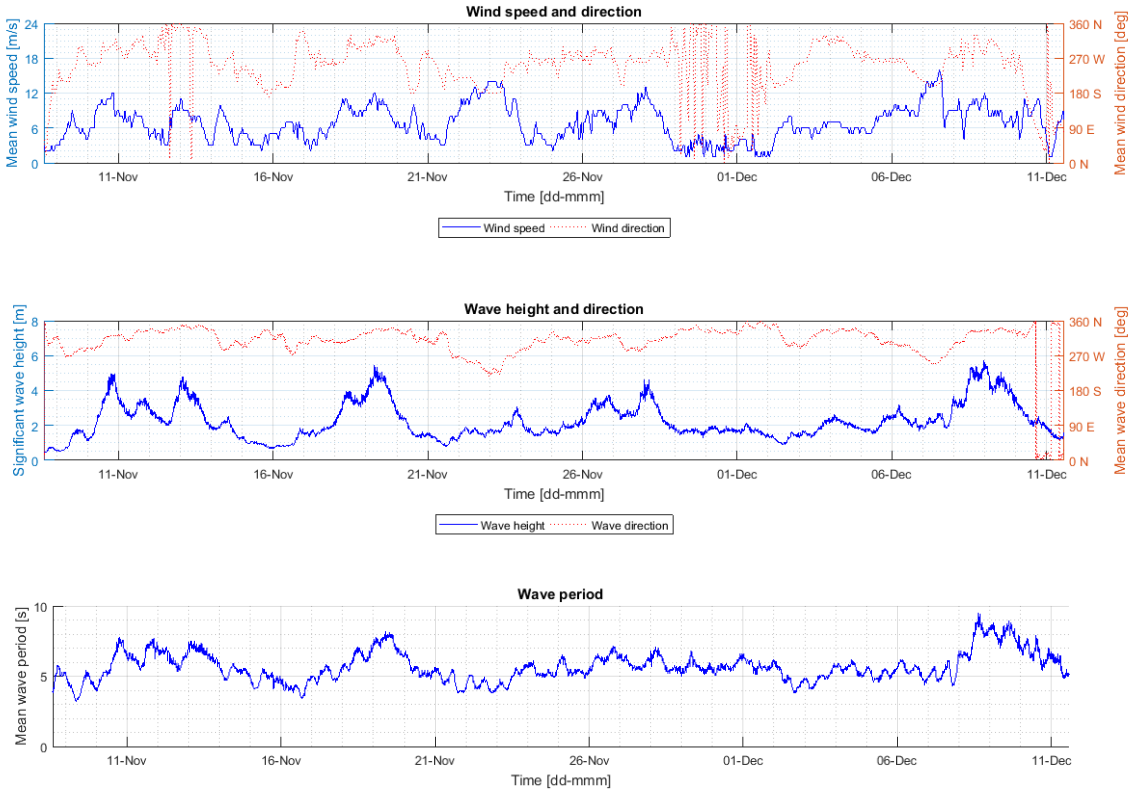

Figure 29 Wind and waves characteristics during November 2017 field campaign at Ameland tidal inlet

Time series of wind and waves characteristics during the period of the field campaign are presented in Figure 29. From the graph of wave height and direction it is possible identify several storm events over this time interval when the wave height can exceed 4 m. These events occurred on 10, 13, 18-19, 28 November and 8-9

December. For the yearly average statistics (Table 1 in Chapter 2) these wave height values correspond to events with approximately 1% exceedance frequency. However, for the KG2 measurement period wave height of 3.75 m is exceeded 10% of the time and 1% exceedance frequency corresponds to wave height of 5 m. From comparing it with the yearly distribution of the wave's statistical characteristics (Figure 6 in Chapter 2) it can be concluded that the measurement period can also be characterised as stormier than it is on average in November and December.

From the wind conditions in Figure 29 and Table 9, which shows an average wave height corresponding to a certain combination of wind speed and direction, we can see that highest waves are observed when strong wind of more than 8 m/s is coming from the west and north-west. Figure 30 shows that waves approach the coast mainly from northwest and the highest waves were originating from north-northwest. In Figure 31, which relates observed significant wave height and mean wave period, we can see that during field campaign high waves were mainly observed together with high wave periods, which means that the role of swell waves is not very large. Between the storm events periods of relatively calm conditions are observed, during these periods wave height mostly did not exceed 2 m. Lower wave heights are mainly related to the periods with lower wind speed, however, wind directions also plays a role here. It can be seen that winds with velocities larger than 8 m/s coming from the south or south-southwest, which was observed from 22 to 24 November and on 7 December, only resulted in wave heights of about 2 m.

From the wind rose, which is presented in Figure 30, as well as from the Table 9 we can see that most frequently observed wind direction at the Ameland tidal inlet during the field campaign was from the west. North-western wind, which results in the highest waves, was observed much less frequently and the strongest wind was observed for directions between south and southwest. Comparing it to the yearly wind rose (Figure 5 in Chapter 2) we can see that over the year wind is much more variable and ratio of winds coming from the west and northwest is much smaller. This, along with previous conclusions on the wave conditions, shows that the period when the field campaign took place is characterised by very different conditions from yearly-average and therefore conclusions obtained from this data set cannot be directly extrapolated to other periods of the year.

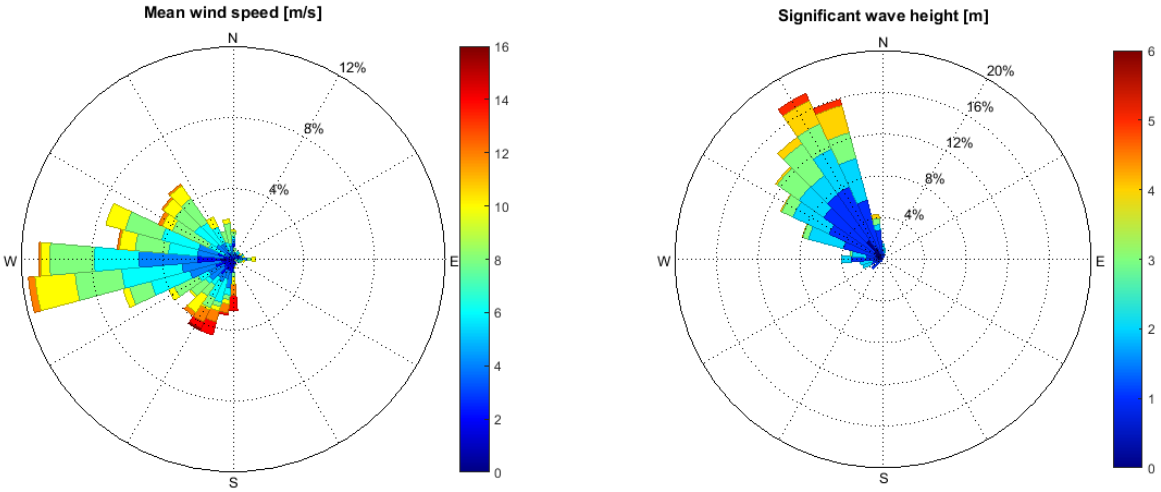

Figure 30 Wind and waves roses during November 2017 field campaign at Ameland tidal inlet

Table 9 Average significant wave height in [m] for different combinations of wind speed and directions during KG2 field campaign and in brackets – occurrence of these wind conditions in [%] (coloured cells denote most frequently observed wind conditions: orange – more than 10% and yellow – between 5 and 10%)

Wind direction	Wind speed [m/s]			
	0 - 4	4 - 8	8 - 12	12 - 16
N	1.8 (2.0)	2.3 (1.4)	3.7 (2.3)	-
NE	1.1 (1.3)	1.8 (1.2)	2.5 (0.6)	2.4 (0.3)
E	1.0 (2.5)	1.5 (1.2)	2.0 (0.8)	-
SE	1.3 (1.0)	2.1 (0.1)	2.2 (0.5)	-
S	1.2 (2.4)	1.0 (3.2)	2.0 (1.6)	1.8 (3.3)
SW	1.2 (3.8)	1.4 (5.7)	1.9 (5.8)	2.1 (1.4)
W	1.7 (4.1)	2.1 (21)	3.1 (14)	3.9 (0.3)
NW	1.8 (2.0)	2.2 (7.4)	4.0 (8.5)	4.8 (0.3)

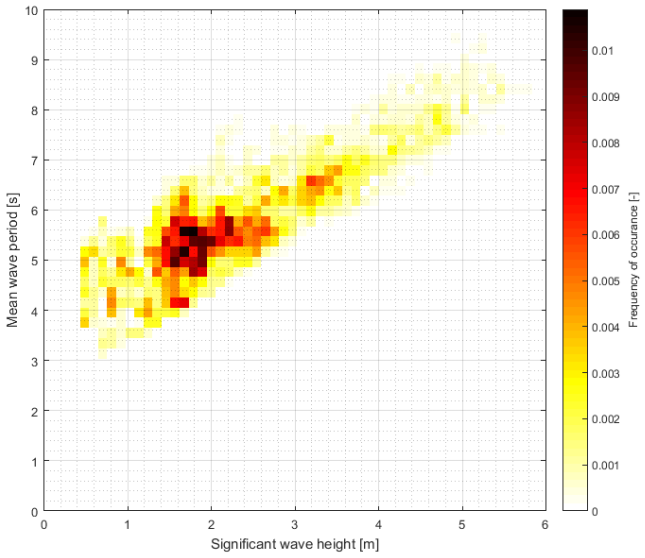

Figure 31 Correlation between significant wave height and mean wave period during the period of KG2 field campaign at wave buoy AZB11

4.2 TIDAL CURRENTS

First of all, depth-average longshore and cross-shore currents time series were analysed for all three frames on the lower shoreface, which are presented on the Figure 32 along with wave height and direction. From this figure it can be seen that currents at the lower shoreface follow a semidiurnal (M2) tidal pattern and that velocity in the longshore direction has a much larger M2 amplitude at all three frame locations in comparison with the currents in cross-shore direction. Besides that, from a closer look of the currents (Figure 33), certain variation can be seen between different locations along the lower shoreface during calm and storm conditions. During calm conditions peak flood velocities in both cross-shore (northward positive) and longshore (eastward positive) directions are very close to each other, while during ebb at shallower frames F3 and F4 smaller westward current can be observed in longshore direction and higher offshore current – in cross-shore direction. During storm events we can see that difference between currents in the longshore direction at shallower and deeper locations significantly increases. This can be seen for the storm events of November 11-

13, 18-20 and 26. However, this is not always the case as for November 27-28 velocities at the deepest frame F1 are also shifted eastward and match velocities at frames F3 and F4. Meanwhile, cross-shore currents, which during regular conditions vary within 0.1 – 0.2 m/s in onshore or offshore direction at all three frames, during storm events do not show a regular tidal pattern and are directed more towards the coast with peak velocities reaching 0.5 m/s. In general, at these peaks onshore velocities increase towards shallow water, however, for certain events, such as on November 19, almost equal velocities at all three lower shoreface frames can be noted.

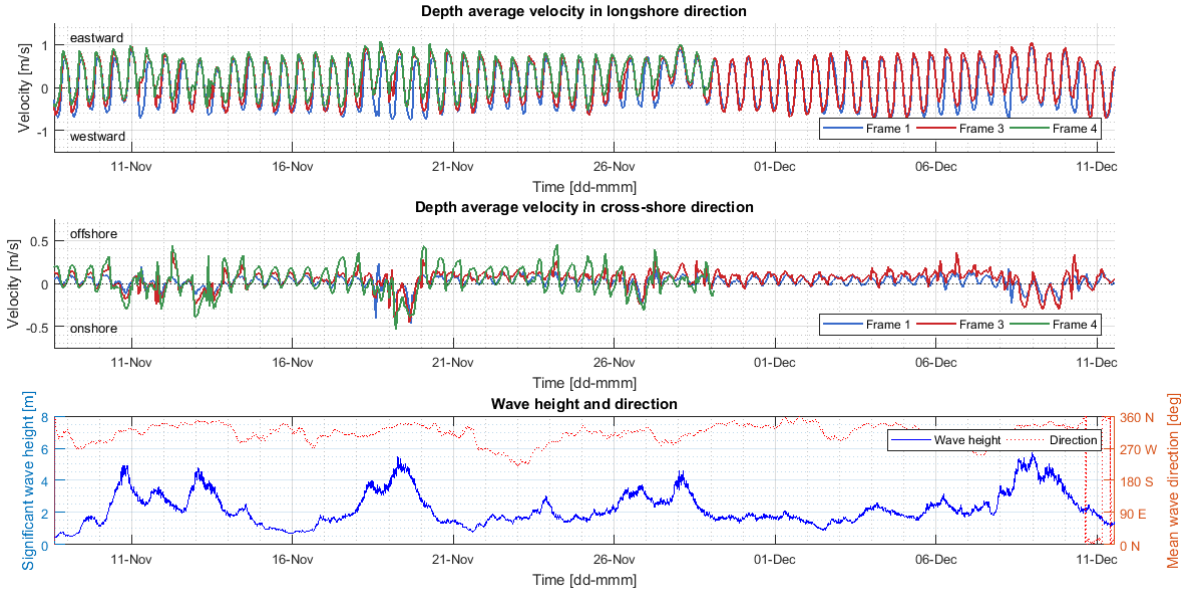

Figure 32 Depth-average currents in longshore and cross-shore direction at the lower shoreface frames

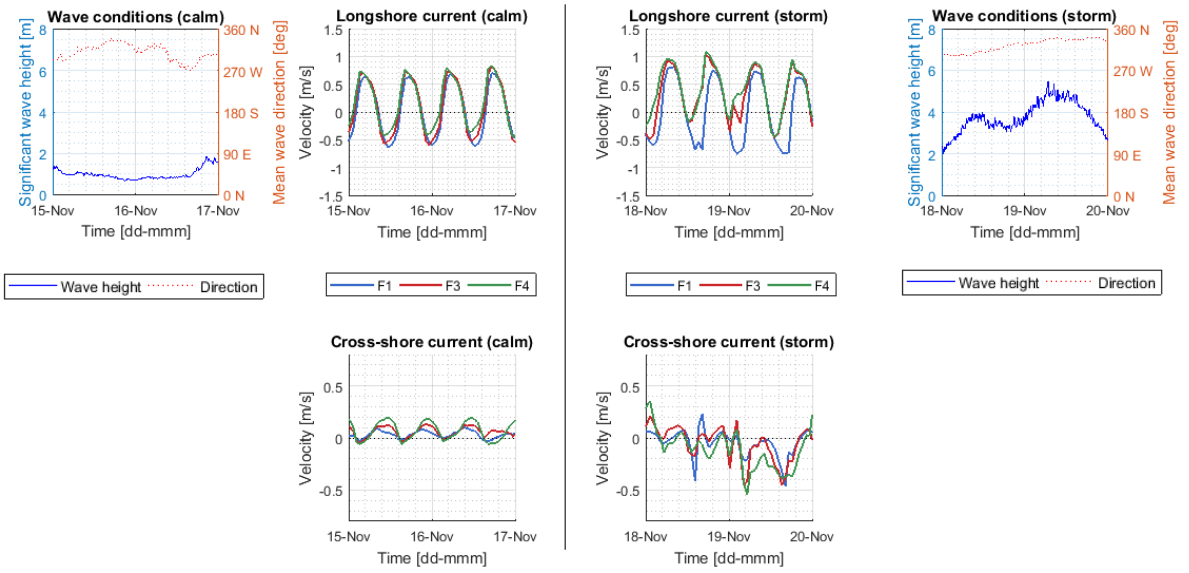

Figure 33 Close-up of depth-average currents in longshore and cross-shore direction during calm (left) and storm conditions (right)

To investigate tidal currents in more detail, they can be converted from time domain into frequency domain by the means of Fourier transform (Figure 34). From this figure it can be seen that, indeed, for all three locations currents are dominated by semidiurnal tides at a frequency of approximately 0.08 cycles per hour. At the frequency of principle lunar semidiurnal tidal component M2 velocity amplitude is roughly the same at frames

F1 and F3 and equals 0.55 m/s in longshore and 0.04 m/s in cross-shore direction. At shallower located frame F4 velocity amplitude at this frequency increases to 0.12 m/s in cross-shore direction, and decreases with approximately the same amount for longshore direction relative to frames F1 and F3. Also, for frames F1 and F3 velocities in both longshore and cross-shore direction there are two other smaller peaks visible at both sides of the M2 peak, which correspond to principle solar and lunar elliptic semidiurnal tidal components S2 and N2 with periods of 12 hours and 12 hours 40 minutes respectively. In transformed velocities at frame F4, however, there is only one peak present that corresponds to M2 constituent, which can be caused by the fact that record length at F4 is shorter than at F1 and F3, only 21 days instead of 33, which results in lower number of frequencies that are distinguished in Fourier transform. Besides that, a small increase in velocity amplitude of order 0.01 – 0.02 m/s for frame F4 can be seen on the left side the graph, which corresponds to low frequency variations in currents. This is not a large increase on itself, but it can be important for residual currents, which mainly correspond to these frequencies.

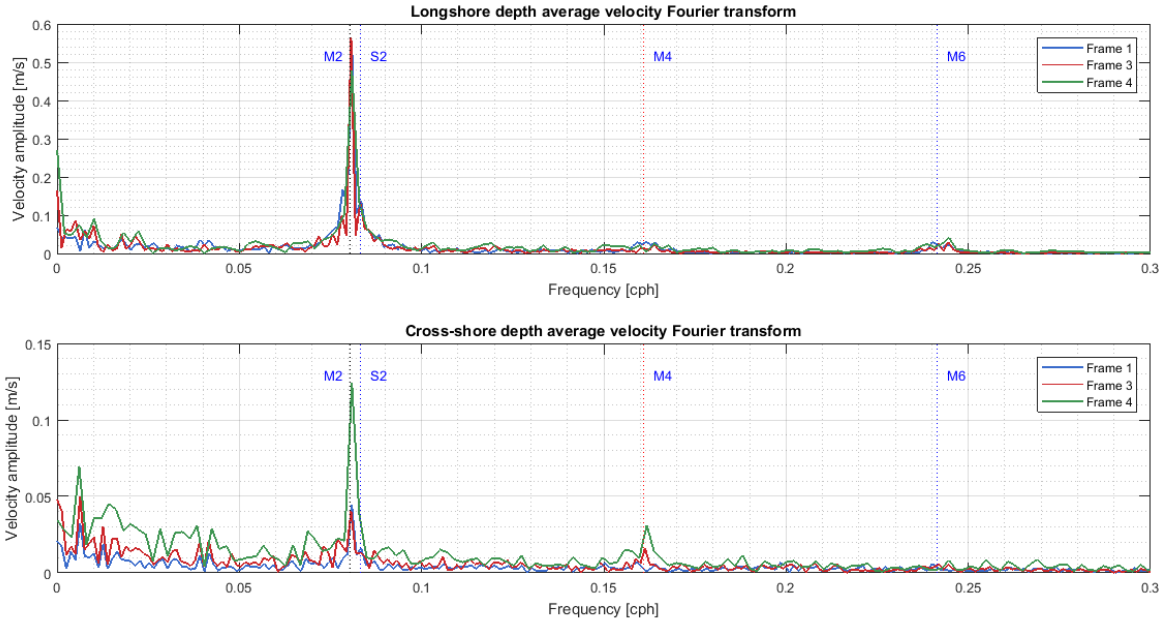

Figure 34 Fourier transform of depth-average currents in in longshore and cross-shore direction at the lower shoreface frames (frequency in "cph" = cycles per hour)

In order to convert measured velocities into independent harmonic constituents with known tidal frequencies harmonic analysis was performed using T_TIDE. Estimated characteristics of tidal ellipses for depth-average current constituents with semi major axis velocity larger than 0.05 m/s at frames F1, F3 and F4 are presented in Table 10, Table 11 and Table 12 respectively. From these tables it can be seen that M2 component current with a period of 12 hours 25 minutes is dominant for all the frames and is directed mainly longshore, moving towards shallower water its magnitude slightly decreases and small rotation of the tidal ellipse is observed causing an increase in cross-shore velocity amplitude, which is also shown in Figure 35. Second most significant component at all the frames is S2 with a period of 12 h, which has a magnitude of 0.15 – 0.20 m/s over the major axis and, similarly to M2, slightly deviates from the longshore direction at the shallower frame. Because of shorter record length at frame F4 several tidal components could not be estimated for this location, including lunar elliptic semidiurnal component N2, which has a period a period of 12 hours 40 minutes and is quite significant at the frames F1 and F3 with 0.13 and 0.11 m/s respectively on the major axis, this issue can also be seen from the Fourier transform results in Figure 34.

Table 10 Ellipse characteristics for main tidal components at frame F1

Tidal constituents	Period [hours]	Major axis [m/s]	Minor axis [m/s]	Direction [deg]	Phase angle [deg]	Rotation
M2	12.4	0.58	0.05	0.4	218	Clockwise
S2	12.0	0.15	0.01	3.2	265	Clockwise
N2	12.7	0.13	0.00	2.9	202	Clockwise
L2	12.2	0.06	0.01	177	36.0	Clockwise
MU2	12.9	0.05	0.00	177	157	Clockwise
O1	25.8	0.05	0.01	11.5	161	Clockwise
MSF	354	0.05	0.01	7.9	168	Counter clockwise

Table 11 Ellipse characteristics for main tidal components at frame F3

Tidal constituents	Period [hours]	Major axis [m/s]	Minor axis [m/s]	Direction [deg]	Phase angle [deg]	Rotation
M2	12.4	0.55	0.03	0.3	204	Clockwise
S2	12.0	0.15	0.01	0.4	241	Clockwise
N2	12.7	0.11	0.01	5.4	200	Clockwise
NO1	24.8	0.07	0.02	8.6	9.27	Clockwise
MSF	354	0.07	0.02	2.3	131	Counter clockwise
MU2	12.9	0.05	0.01	0.4	330	Clockwise

Table 12 Ellipse characteristics for main tidal components at frame F4

Tidal constituents	Period [hours]	Major axis [m/s]	Minor axis [m/s]	Direction [deg]	Phase angle [deg]	Rotation
M2	12.4	0.50	0.03	13.4	195	Clockwise
S2	12.0	0.19	0.00	12.7	238	Clockwise
2MS6	4.09	0.05	0.01	3.7	148	Clockwise

The rest of the components are relatively small around 0.05 – 0.07 m/s and less and their ellipses mostly have an orientation close to longshore. Besides magnitude and phase, T_TIDE also allows to estimate 95% confidence intervals of both those characteristics for all tidal components. For most of them confidence intervals for amplitude is about 0.01 m/s for both cross-shore and longshore currents, which is relatively small for the main constituents M2, S2 and N2, but it becomes more and more important components with lower amplitude. Phase error for the dominant components is also relatively small, for M2 tide it is less than 2 degrees for longshore and 5 to 10 degrees for cross-shore current. This error, however, also increases with decreasing constituent's current velocity amplitude and can reach 180 degrees.

Summarizing the results of harmonic analysis of depth-average currents on the lower shoreface it is possible to conclude that they are mainly dominated by major semidiurnal components and the record length allows to estimate them with relatively good accuracy. But, even though it is possible to determine characteristics of 35 and 17 tidal constituents, because of short record length for most of them, except the main tidal constituents M2 and S2, confidence intervals for amplitude and phase are still quite large. Besides that, for even shorter record at frame F4 harmonic analysis for several constituents cannot be performed, including N2, which could be estimated for the longer records at frames F1 and F3 and has shown to have quite large amplitude.

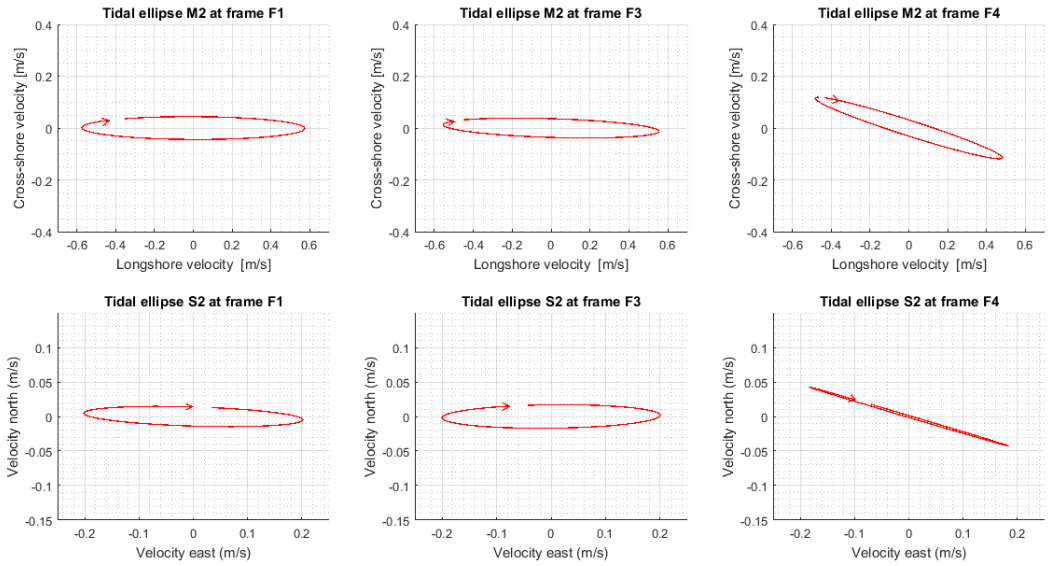

Figure 35 M2 and S2 tidal ellipses for depth-average currents at the lower shoreface frames

4.3 RESIDUAL CURRENTS

In this section residual currents, that were obtained using the Fourier transform low-pass filter described in Section 3.2, will be analysed. In Figure 36 depth-average residual currents in longshore and cross-shore direction are presented for all the frames. From this figure it can be seen that, in general, longshore residual currents are directed to the east at all three locations and are dominant over the cross-shore residual currents. Moving from deep to shallow water, the longshore residual current increases and also influence of storms becomes more significant. It can be seen that during the periods with higher waves the longshore residual current at a water depth of 20 m almost does not change, while closer to the coast, at water depths of 16 and 11 m, it shows an increase of 0.2 – 0.4 m/s when the observed wave height reaches 3 – 4 m and can reach 0.5 m/s. In its turn, direction of the cross-shore residual current varies depending mainly on wind and waves conditions. From the figure it can be seen that during calm periods, when the wave heights are less than about 2 m, a small residual current directed away from the coast is observed, while during high waves the residual current is directed towards the coast. Similar patterns are observed for all three frames, but the magnitude of the current increases with decreasing water depth: during storm events larger onshore currents are observed at shallower frames, while after storms and during calm conditions there are higher offshore residual currents at shallower frames. Besides that, right after storm events (e.g. on November 20) an increased seaward current can be seen in the residual currents time series. This increase is particularly visible for the shallowest frame, for which after storms the highest offshore currents are observed. Possible explanation for this could be the process of emptying of the Wadden Sea through the tidal inlet after it is filled during storm. And presence of the residual onshore current during high waves at 20 m water depth suggests that its origin is not wave-driven only as at this water depth there should not be any wave breaking.

These patterns for all three frames in general can be seen for the storm events on November 11, 13, 19 and 26. However, around November 28, we can see that the longshore residual current at the deepest frame reaches nearly 0.5 m/s, which is almost the same as at the middle frame, which is not observed for any other storm event within the period with available data. Residual in cross-shore direction for the same time moment, meanwhile, also does not show any onshore current for all the frames, which is present for other events with comparable wave height. This can suggest that currents during this particular event are partly or entirely caused by different physical mechanisms then currents that are observed for other storm events.

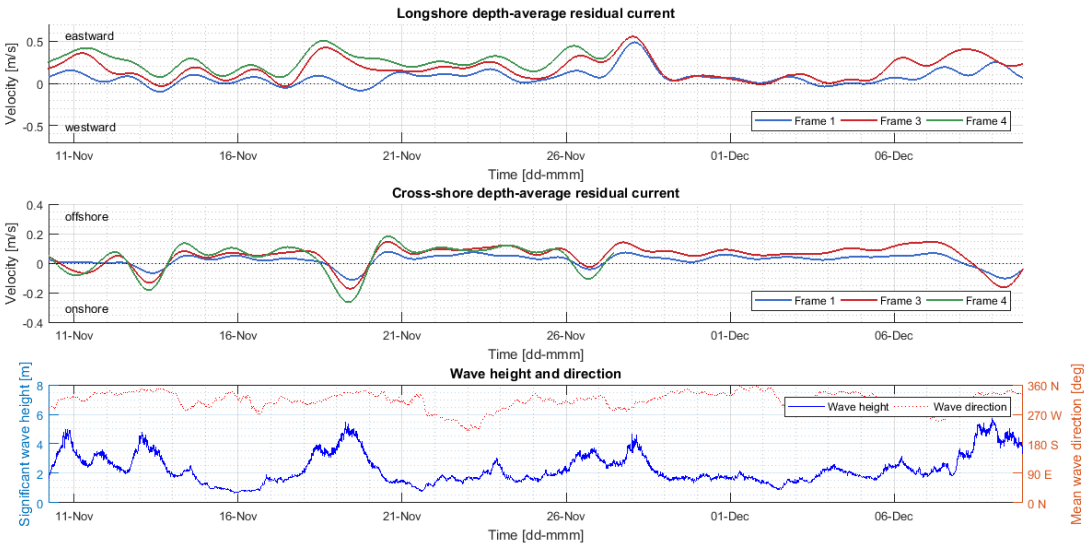

Figure 36 Longshore and cross-shore depth-average residual current at lower shoreface frames

Figure 37 shows the residual current profile scaled by the mean water depth for the period between November 8 and November 29. This time interval was taken for the sake of comparison as at frame F4 measurements in the upper part of the water column are available only for this period. From this figure it can be seen that in the longshore direction time-average current over the entire water column at all the frames is directed to the east and, similarly to the depth-average residual current, it increases towards the shallower water. The depth- and time-average velocity changes from 0.08 m/s at frame F1 to 0.28 m/s at frame F4. Vertical profile of the residual longshore current has more or less a logarithmic shape except for the upper part of the water column, where for all three frames an increased eastward longshore current is observed. For the cross-shore currents residual profiles combine landward currents during storm events and seaward currents during calm conditions. Current magnitude and its variation from deeper to shallower water is in general much smaller than for longshore currents, depth-average velocity is directed seaward and is about 0.02 m/s at frame F1 and 0.04 – 0.05 m/s at frames F3 and F4. However, the direction of current changes between different parts of the water column: near the bed flow residual current is very close to zero, in the middle part current magnitude increases reaching approximately 0.05 – 0.1 m/s in the seaward direction, while near the surface it is directed towards the coast, which, similarly to the increase in longshore current near the surface, has to do with the effects of Stokes drift due to waves and also tidal action.

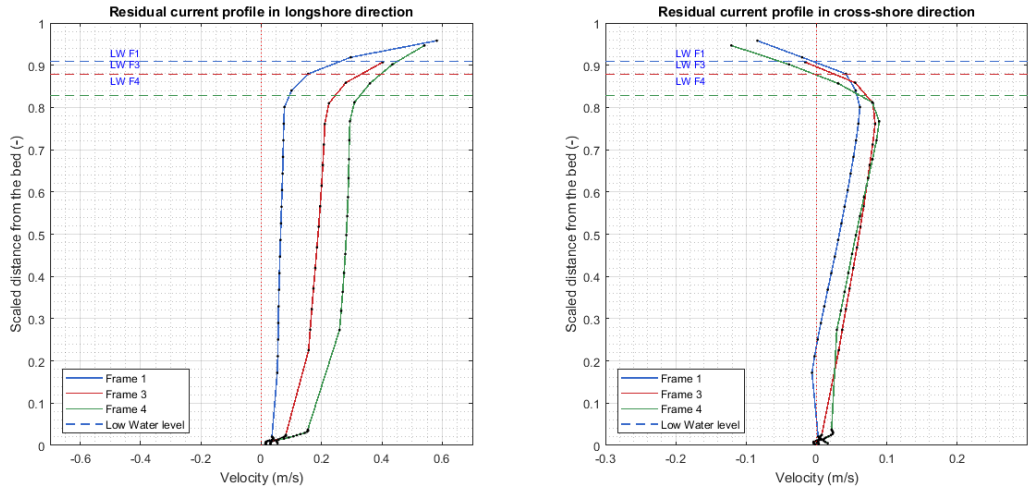

Figure 37 Longshore and cross-shore residual current profile at lower shoreface frames over a period between 8th and 29th of November

In order to analyse in more detail the influence of different wind and wave conditions on currents, residual velocity profiles were also made for several different periods of approximately 25 hours that corresponded to different, more or less steady wind and wave conditions. In total, for this purpose five time intervals were selected, which can be characterised as:

1. peak storm event, characterised by wave heights between 3.5 and 5.5 m and mainly north-western wind of 8 to 12 m/s (November 18-19);
2. period right after the peak storm event, during which an increased seaward current is observed for depth-average residual currents, wave height over this period decreases from 2.5 to approximately 1.5 m and wind speed is around 6 m/s with direction varying between western and southern (November 20-21);
3. period or strong southern wind with speed of 12 to 14 m/s and less than 2 m wave height (November 22-23);
4. calm period with wave heights less than 1 m and wind speed between 3 and 6 m/s (November 15-16);
5. storm event with strong 8-12 m/s wind coming from the west and 2.5 to 4.5 m waves, for which differences from other storm events were noted from the analysis of depth-average residual currents (November 27-28);

These periods are highlighted in the time series of water levels, wind speed and direction and wave characteristics, shown in Figure 38.

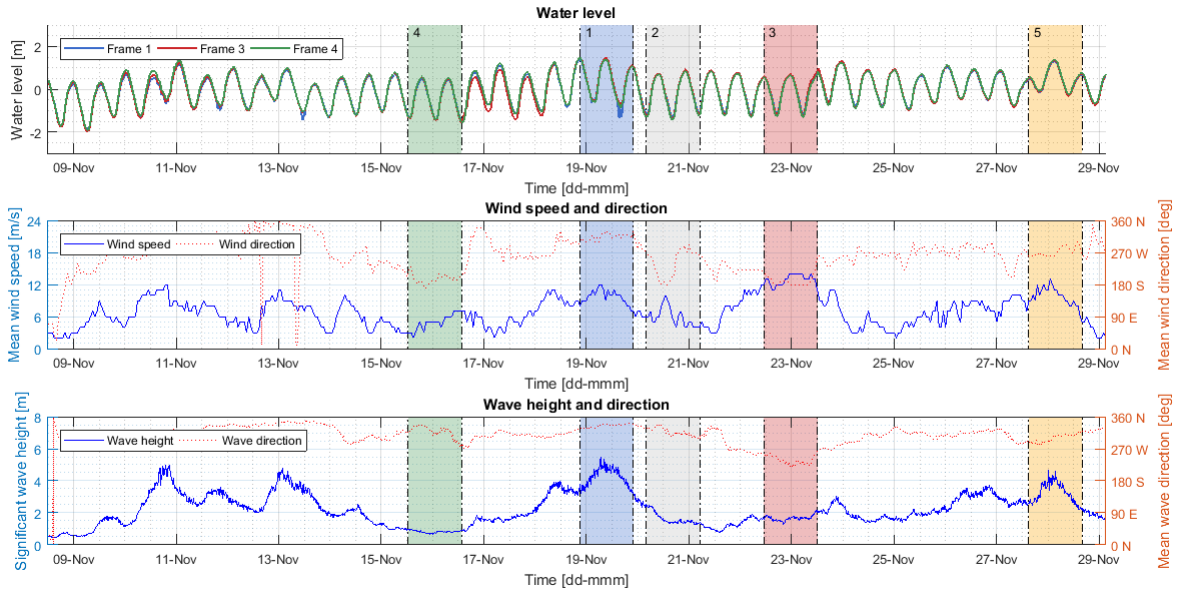

Figure 38 Selected periods for residual current profiles

The velocity profiles for the different time intervals for all the frames are shown in Figure 39. In general, these profiles confirm what was observed for depth-average residual currents. The main thing that can be noted here is that there are no signs of offshore return current (undertow) in the cross-shore direction at any of the frames during the storm event on 18-19 November (period 1). Instead, an onshore current can be observed for the entire water column, which increases towards shallow water and after the peak of the storm (period 2) it changes direction to offshore also over the entire water column. For all other periods cross-shore currents are also directed mainly offshore.

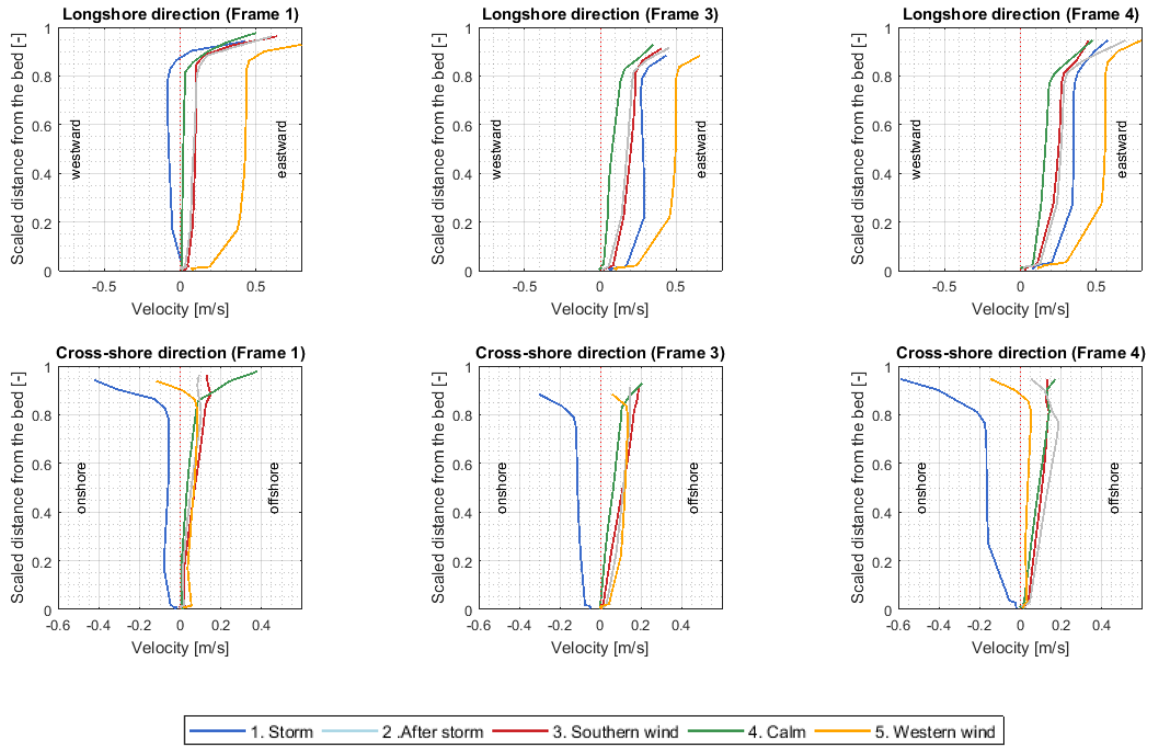

Figure 39 Residual current profiles in longshore and cross-shore directions for different wave and wind conditions

4.4 WATER LEVELS

Near the Ameland tidal inlet there are two stations that systematically measure water level: Terschelling Noordzee (TNZ), which is located in the North Sea offshore of Terchelling Island in middle between Vlie and Ameland tidal inlets, and Nes, located in the Wadden Sea near Ameland Island in the middle between Ameland and Frisian inlets (Figure 4 in Chapter 2). Measured water levels as well as filtered time series from those two stations are shown in Figure 40 along with wave conditions. In general, total water level is a result of combined action of tides, storm surge, which includes wind-driven and pressure contributions, and wave setup. From the filtered data it can be seen that, indeed, during storm events water levels at both locations can be up to 1 meter higher compared with calm conditions. Besides that, it can be seen that during storm conditions water level increases more at the station inside the Wadden Sea leading to higher water level difference between two stations. Because station Nes is located inside the Wadden Sea and the fact that it is basically closed by the Ameland Island from wind and waves during storm events in the North Sea suggest that role of local wave setup and wind-driven surge in water level variation at this location should be relatively small. Because of that it can be assumed that observed water level increase at Nes during storms is mainly caused by water inflow into the Wadden Sea, which develops during storms due to direct flow through the inlet due to wave- and wind-driven currents or due to water level increase in the North Sea and, consequently, water level gradient at the tidal inlet.

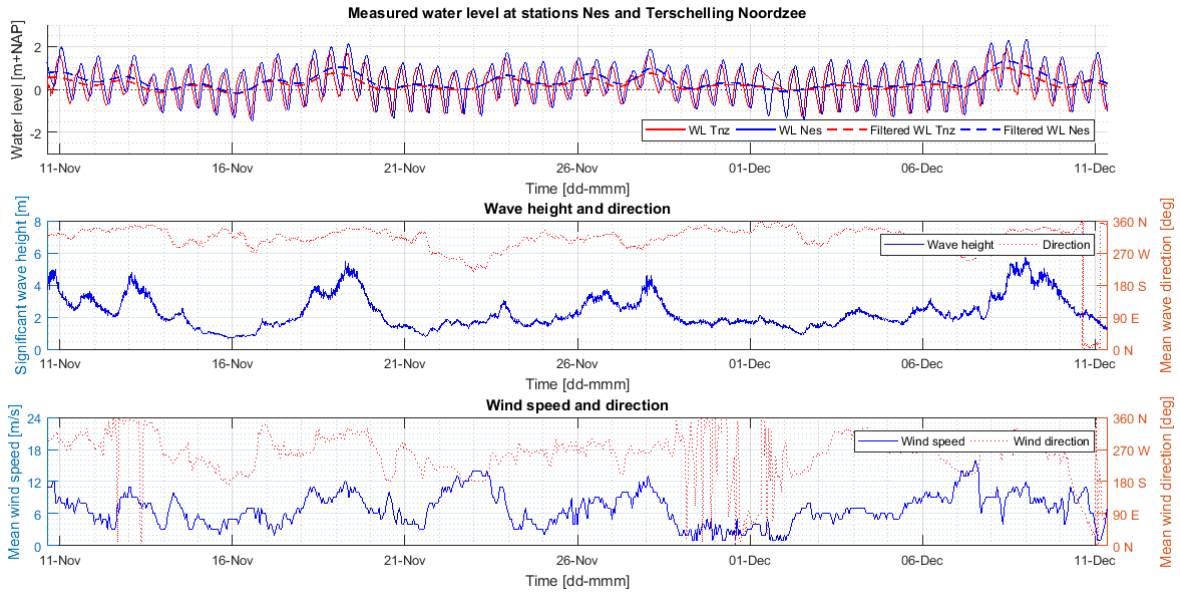

Figure 40 Measured and filtered water levels at stations Terschelling Noordzee (TNZ) and Nes

4.5 DISCUSSION AND CONCLUSIONS

The results of the data analysis can be summarized in the following points:

- Currents on the lower shoreface are mainly dominated by tidal action, however, they can be significantly altered by storm events, which especially can be seen from analyzing filtered current time series
- During calm conditions a small eastward longshore and seaward cross-shore residual current is observed, while during storms longshore current to the east increases and in cross-shore direction current changes direction to onshore over the entire water column. After the storm event usually there can be seen a slightly increased offshore current. These patterns are visible at all three locations that were analyzed, even at water depth of 20 m, and magnitude of theses currents in general increases towards shallower water.
- This type of currents in the cross-shore direction can result from exchange between North Sea and Wadden Sea. From the water level data it can be seen that in front of the Terschelling Island, surge water level can go up by almost 1 m compared to what is observed during calm conditions. Similar surge water level increase can be seen also at the water level station inside the Wadden Sea where the effect of wind and wave setup should be relatively small. This means that the water is flowing in through the tidal inlet during storm events, which can be caused by a combination of direct flow through the inlet due to wave- and wind-driven currents and water level setup on the barrier islands resulting in the water level gradients between two basins.
- For one of the storm events, different pattern in the currents was observed: at all three frames there was a strong longshore current to the east, while in cross-shore direction none of the frames showed an onshore current, which was present for all other events. Because of that, a hypothesis can be made that in this case currents are driven by different forcing mechanisms, in particular strong western wind.
- From the data it is hard to distinguish between different processes that contribute to the observed currents and better understanding can be obtained using also the results of hydrodynamic modelling, which will be discussed in the following chapters

5. VALIDATION OF THE OFFLINE SEDIMENT TRANSPORT MODELLING APPROACH

In this chapter of the report, the results of the offline sediment transport modelling approach validation for the lower shoreface of the Ameland tidal inlet will be presented. First, the results of the DCSM-FM model validation by the measured water levels, discharges through the tidal inlet and currents on the lower shoreface from the KG2 field campaign will be given and comparison will be done between model versions with different grid resolution. The effects of updating the model bathymetry at the Ameland tidal inlet on the results will be analysed. After that, the results of the detailed Delft3D model with and without the effect of waves will be presented and compared with the results of the DCSM model in order to assess the effects of model resolution and importance of the wave-driven currents on the lower shoreface. Finally, measured and the DSCM model currents will be used to calculate the sediment transport rates using the TSAND model and the mismatch in the total net transport and in the net transport for different wave conditions due to different currents input will be analysed. Contributions of bedload and suspended load will be presented for the period of the field campaign. In order to make a conclusion about applicability of the offline sediment transport modelling approach for calculating the net annual transport on the lower shoreface of the Ameland tidal inlet, the importance of the mismatch on a yearly time scale will be analysed by comparing the transport rates, calculated from the measured currents for the period of the field campaign, with the yearly sediment transport for 2017, determined from the DCSM model currents

5.1 DCSM-FM MODEL WATER LEVELS

In order to analyse how well the different model versions reproduce the hydrodynamics of the North Sea and the Wadden Sea in the area of the Ameland tidal inlet, first of all, modelled water levels were compared with the standard measurements that are conducted at stations Terschelling Noordzee (TNZ) and Nes, which were also analysed in Chapter 4. For this purpose, goodness of fit statistics were calculated for the time series of measured and modelled water levels for the year of 2017. These results are presented in Table 13 and there we can see that for both stations there is high correlation between the measurements and the model with correlation coefficient values exceeding 0.95. Also, it can be seen that for both stations there are high positive bias values, which means that the model on average overestimates the actual water levels. One of the explanations for the positive bias values could be the difference between two reference systems that are used in the model bathymetry: NAP and the Mean Sea Level (MSL). The NAP coordinates are used in the Baseline dataset, which is used to derive model bathymetry near the Dutch coast, while for the rest of the model domain the EMODnet bathymetry was used, which is relative to the Lowest Astronomical Tide (LAT) and was converted into relative to MSL for the DCSM-FM model. Because the conversion between the two reference systems is very complex and is not clearly defined, both of them were used at the same time for different areas. However, the MSL along the Dutch North Sea coast is between 0 and 0.1 m +NAP, while the model bias values in the calibrated 0.5 nm model version are about 0.35 m. This happens because the calibration of the model was done in order to obtain better results for the water level variation, while the mean water level was disregarded in the analysis. Because of that, in Zijl et al. (2018) the results of the model performance for the water levels were presented in a form of RMSE with preliminarily removed bias (uRMSE). From the Table 13 we can see that the values of uRMSE for the station TNZ in 2017 are the same as presented in Zijl et al. (2018) for the period from 2013 to 2015 and are equal 0.09 m for both 1 nm and 0.5 nm model versions. The station Nes was not included in the report of Zijl et al. (2018) and from the Table 13 we can see that uRMSE there is much higher: 0.21 m – for 1 nm and 0.18 for 0.5 nm model, which means the water level variation is captured better in the model outside of the Wadden Sea. The Figure 41 shows the comparison of the surge water levels between the measurements and the model. These water levels were derived by applying the Fourier transform low-pass filter, which was described in the Section 3.2, to the measured and modelled water levels at stations

TNZ and Nes with removed bias. From this figure we can see that all three model versions show very close results and at the station TNZ in the North Sea the surge water levels are reproduced well with all the peaks during storms matching with the data. For the station Nes, however, we can see that during storm events peak water level is underestimated by about 0.2 m. Because the water level inside the Wadden Sea increases during storms due to the water inflow from the North Sea, it means that in the model the exchange is not captured correctly as not enough water is flowing into the Wadden Sea.

The main patterns, such as higher bias and uRMSE and underestimation of the water level during storms inside the Wadden Sea, are identical for original 1 and 0.5 nm model versions and for the new 0.25 nm version. However, we can see different effect from refining the grid from 1 to 0.5 nm and from refining from 0.5 to 0.25 nm. After the first refinement there is only a small reduction in model bias and at TNZ station and small reduction in uRMSE and in bias at station Nes. After the second refinement correlation coefficients slightly decrease at both stations, while uRMSE increases and bias significantly drops. The increase in variation going from the model with 0.5 nm resolution to 0.25 nm is mainly related to different reproduction of the tidal wave in the model with higher resolution as surge water level almost does not change (Figure 41). The results of harmonic analysis of the water levels for the year of 2017, which are presented in Table 14, show that that there is a certain increase in water level amplitude of some of the main tidal constituents (particularly N2, M2 and S2) between the 0.5 nm and 0.25 nm model at both TNZ and Nes stations. Meanwhile, between 1 nm and 0.5 nm models there are only changes in amplitudes at station Nes located inside the Wadden Sea.

Table 13 Statistics of the data-model comparison for the standard water level measurements at stations Terschelling Noordzee and Nes for the year 2017 (colours: green – better then model with a factor 2 lower resolution, yellow – same, red – worse)

Station	Statistics	Model		
		1 nm	0.5 nm	0.25 nm
Terschelling Noordzee	R [-]	0.99	0.99	0.98
	uRMSE [m]	0.09	0.09	0.17
	Bias [m]	0.36	0.34	0.14
Nes	R [-]	0.97	0.97	0.95
	uRMSE [m]	0.21	0.18	0.24
	Bias [m]	0.43	0.35	0.16

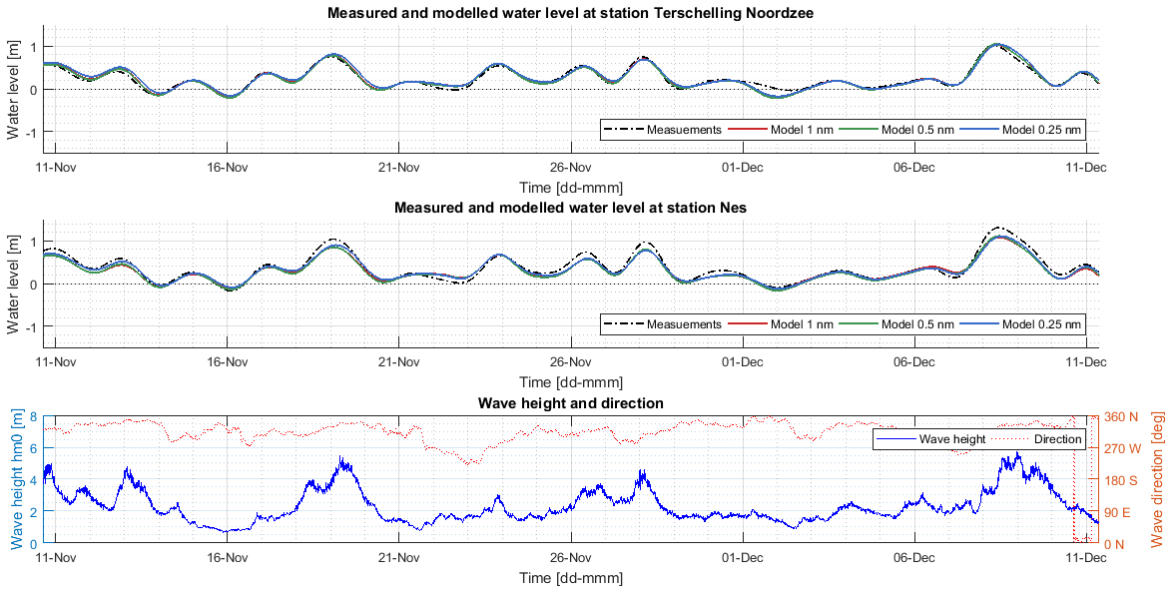

Figure 41 Measured and modelled surge water levels with removed bias at stations Terschelling Noordzee and Nes for the period of the KG2 field campaign

Table 14 Measured and modelled water level amplitude of the main tidal constituents calculated using T_TIDE at stations Terschelling Noordzee and Nes for the year 2017

Tidal constituents		Amplitude [m]							
		Terschelling Noordzee				Nes			
		Data	Model			Data	Model		
Name	Period [h]		1 nm	0.5 nm	0.25 nm		1 nm	0.5 nm	0.25 nm
O1	25.8	0.09	0.10	0.10	0.08	0.09	0.09	0.09	0.08
K1	23.9	0.08	0.08	0.09	0.08	0.07	0.08	0.08	0.07
N2	12.7	0.14	0.15	0.15	0.17	0.15	0.12	0.13	0.15
M2	12.4	0.87	0.90	0.90	0.97	0.93	0.78	0.85	0.93
S2	12.0	0.24	0.25	0.25	0.27	0.25	0.20	0.22	0.24
K2	12.0	0.07	0.08	0.08	0.08	0.07	0.06	0.07	0.07
M4	6.2	0.08	0.09	0.09	0.08	0.09	0.03	0.05	0.05

This difference in the model performance for the water levels results from the fact that 1 and 0.5 nm model versions were calibrated for the water level amplitude of the main tidal constituents outside of the Wadden Sea using different spatially varying roughness, while for the 0.25 nm model calibration settings of the 0.5 nm model were used. Different calibration of 1 and 0.5 nm models was done in order to account for the differences between real and model bathymetry, which come from the coarse model resolution. As it was already mentioned before, in order to obtain model bathymetry, measured bed level data was averaged within the area of one cell size around the grid node. Because of the coarse model resolution, tidal inlet channels in the model are always shallower than in reality and the difference increases with decreasing model resolution. Tidal inlet channels in general play very important role in hydrodynamics of the area as they conduct most of the flow that goes in and out of the Wadden Sea over a tidal cycle and this exchange also has an influence on propagation of a tidal wave along the North Sea coast. Because of that, in order to correctly reproduce the exchange and get more accurate representation of the water levels in the model, during the process of calibration lower friction was imposed in the model for inside of the Wadden Sea compared to the adjacent part of the North Sea. This was the case for both 1 nm and 0.5 nm models, but in the finer model friction

coefficients were set higher as the depth of the tidal inlet channels was higher and thus meaning lower resistance for the flow through the inlet. When the 0.5 nm model was refined in the area of the Wadden Sea, the inlet channels became even deeper. This means that the friction values, derived for 0.5 nm model, are too low for the 0.25 nm model, which results in overestimation of the water level amplitude and reduction of the mean water level.

Because of that, it can be concluded, that refinement of the model grid to 0.25 nm in the Wadden Sea requires a recalibration in order to properly compare its results. Because of the time limitations it was not possible to do this within current master thesis project and all the further analysis will focus only on original calibrated 1 and 0.5 nm model versions. Another factor for that choice is that the 0.5 nm model has significantly lower computation time compared to the 0.25 nm model (79 hours or 3.3 days against 179 hours or 6 days for one year of simulation), which is an important consideration for modelling the sediment transport over periods of several years and longer. The sensitivity of the model results to the bathymetry update will be analysed using the 0.5 nm model versions. In order to assess the effects of model resolution on the results, the detailed Delft3D model will be used along with the DCSM-FM model.

5.2 DCSM-FM MODEL DISCHARGES THROUGH THE TIDAL INLET

Besides water levels, exchange between the North Sea and the Wadden Sea in the DCSM-FM model can also be validated by comparing discharges through the Ameland tidal inlet in the model with discharge measurements that were conducted during September stage of the KG2 field campaign. Discharges through the Ameland tidal inlet were measured three times over a full tidal cycle on September 1, 5 and 19. In Figure 42 water levels along with observed wind and wave conditions during the periods of discharge measurements are presented. From this figure we can see that all three periods correspond to calm conditions as significant wave height during these intervals does not exceed 1 m.

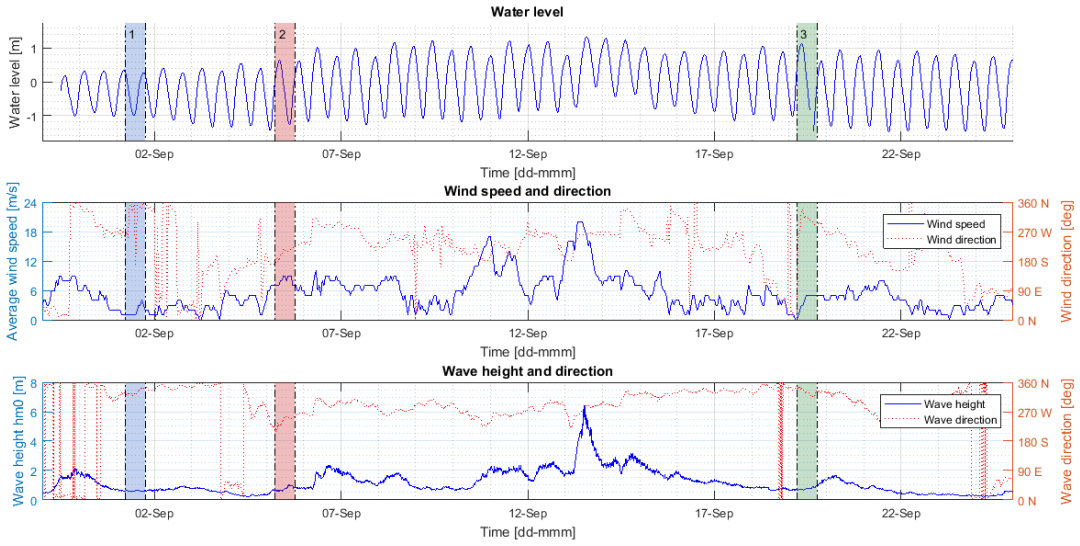

Figure 42 Water levels, wind and wave conditions during discharge measurements at Ameland tidal inlet: 1) 1 September; 2) 5 September; 3) 19 September

In Figure 43 time series of measured and modelled discharges through the tidal inlet during all three periods are presented and in Table 15 measured and modelled total flow in and out of the Wadden Sea over the periods of the discharge measurements is given. From it we can see that for all three periods in the DCSM model both inflow and outflow of the Wadden Sea are overestimated, which might be caused by higher mean water level in the model, and this overestimation is higher for the periods on September 5 and 19, which are characterised by higher tidal amplitude then the period on September 1.

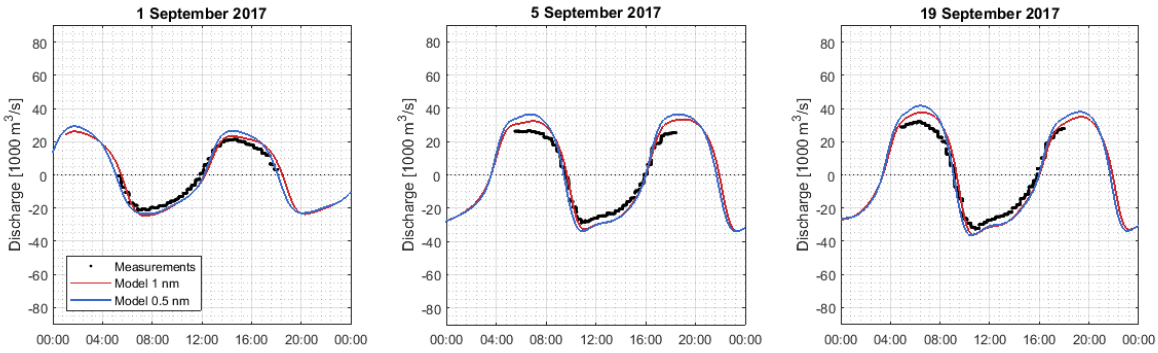

Figure 43 Comparison between measured and modelled discharges through Ameland tidal inlet

Table 15 Measured flow through the Ameland tidal inlet compared with the results of all three model specifications

Volume [million m^3]	1 September			5 September			19 September		
	In	Out	Sum	In	Out	Sum	In	Out	Sum
Measured	330	-339	-9	480	-449	31	544	-506	38
Model 1 nm	377	-405	-29	598	-523	75	641	-590	51
Model 0.5 nm	401	-424	-23	649	-562	87	683	-625	58

5.3 DCSM-FM MODEL LOWER SHOREFACE CURRENTS

5.3.1 TOTAL CURRENTS

In order to do a comparison on how do different model specifications perform for calculating the currents on the Ameland tidal inlet lower shoreface, several different statistical characteristics were calculated, including correlation coefficient (R), root-mean-square error (RMSE) and bias. These characteristics were calculated at for all three frames locations for currents at three different layers as well as for depth-average currents in longshore (Table 16) and cross-shore (Table 17) direction for all the available data (November 8 to December 13 at frames F1 and F3 and November 8 to 29 at frame F4) and for 1 and 0.5 nm versions of the DCSM-FM model. From these tables we can see that for the longshore current (Table 16) there is high correlation between measured and modelled currents with coefficients above 0.92 at all three locations for both model versions. The better correlation between modelled and measured currents is observed for the frame F1, which corresponds to the deepest location on the lower shoreface. For this frame correlation coefficient values are around 0.98 – 0.99 with RMSE of about 0.1 m/s and absolute values of bias lower than 0.02 m/s. Moving towards shallower water we can see that correlation coefficient slightly reduces and RMSE increases to 0.14 – 0.17 m/s at frame F3 and 0.19 – 0.27 at frame F4. Besides that, we can see that measured longshore velocities become typically underestimated by both model versions, as bias becomes negative and its absolute values increase from 0.05 – 0.1 m/s at frame F3 up to 0.14 – 0.19 m/s at frame F4.

For the cross-shore current (Table 17) we can see that correlation between the measurements and the model is much lower. Besides that, in this case there is no clear relation between correlation and location along the cross-shore profile, which was seen for the longshore currents. Lowest correlation for cross-shore currents is observed for frame F3 with coefficients between 0.13 and 0.34, while highest is observed for the frame F4 with the values of correlation coefficient within 0.56 – 0.62. At location of the frame F1 correlation coefficient for the cross-shore currents is between 0.45 and 0.56. RMSE values for the cross-shore currents increase from 0.06 – 0.08 m/s at frame F1 up to 0.1 – 0.16 m/s at frames F3 and F4, which is significant given that cross-shore

current velocities are in general quite low. The bias for cross-shore currents is also mostly negative and its absolute values vary within 0 and 0.05 m/s.

Comparing the results of model versions with different resolution we can see that there is a certain improvement going from 1 nm to 0.5 nm model, which can particularly be seen for the longshore currents at frame F4, where correlation coefficient increases from 0.92 to 0.96 and RMSE reduces from about 0.25 – 0.27 m/s to 0.19 – 0.22. For cross-shore most significant improvement can be seen for currents at frame F3, where correlation coefficient for depth-average velocities goes from 0.21 up to 0.34 and RMSE goes down from 0.15 to 0.1 m/s, while some small improvements are also observed at frames F1 and F4.

Table 16 Statistics of the data-model comparison for the longshore currents (depth-average and at three different layers) for three Ameland lower shoreface frames and three model versions (colours: green – better then model with a factor 2 lower resolution, yellow – same, red – worse)

Model	Statistics	Frame 1				Frame 3				Frame 4			
		Depth average	16 m	10 m	4m	Depth average	12 m	8 m	4 m	Depth average	8 m	6 m	4 m
1 nm	R [-]	0.99	0.98	0.99	0.98	0.97	0.97	0.97	0.96	0.92	0.93	0.92	0.92
	RMSE [m/s]	0.10	0.11	0.09	0.08	0.14	0.16	0.15	0.15	0.25	0.27	0.26	0.25
	Bias [m/s]	0.01	0.02	0.01	0.00	-0.05	-0.08	-0.07	-0.05	-0.15	-0.19	-0.19	-0.18
0.5 nm	R [-]	0.98	0.98	0.98	0.98	0.97	0.97	0.96	0.96	0.95	0.95	0.95	0.95
	RMSE [m/s]	0.09	0.11	0.10	0.09	0.14	0.17	0.16	0.16	0.19	0.22	0.22	0.22
	Bias [m/s]	-0.01	-0.01	-0.01	-0.01	-0.07	-0.10	-0.08	-0.07	-0.14	-0.17	-0.17	-0.17

Table 17 Statistics of the data-model comparison for the cross-shore currents (depth-average and at three different layers) for three Ameland lower shoreface frames and three model versions (colours: green – better then model with a factor 2 lower resolution, yellow – same, red – worse)

Model	Statistics	Frame 1				Frame 3				Frame 4			
		Depth average	16 m	10 m	4m	Depth average	12 m	8 m	4 m	Depth average	8 m	6 m	4 m
1 nm	R [-]	0.50	0.51	0.45	0.51	0.21	0.27	0.20	0.13	0.62	0.60	0.58	0.57
	RMSE [m/s]	0.07	0.08	0.07	0.08	0.15	0.16	0.15	0.15	0.13	0.16	0.14	0.13
	Bias [m/s]	-0.03	-0.01	-0.02	-0.04	-0.04	-0.01	-0.03	-0.04	-0.04	-0.01	-0.03	-0.04
0.5 nm	R [-]	0.54	0.45	0.45	0.54	0.34	0.34	0.26	0.24	0.62	0.61	0.59	0.56
	RMSE [m/s]	0.06	0.08	0.07	0.07	0.10	0.14	0.11	0.10	0.12	0.16	0.14	0.12
	Bias [m/s]	-0.01	-0.02	0.00	-0.03	0.01	0.05	0.03	0.00	-0.01	0.03	0.01	-0.01

Figures with comparison of the measured and modelled the longshore and the cross-shore current velocity time-series are presented in the Appendix A (Figure A.1, Figure A.2 and Figure A.3 corresponding to frames F1, F3 and F4). From these figures we can see that the mismatch between the data and the DCSM model is observed mainly during conditions with high waves. In order to assess how well does the model perform for predicting tidal variation in the currents a harmonic analysis was performed using T_TIDE for the measured and modelled velocities at the frames. From the calculated tidal constituents' characteristics, a predicted time-series of tidal velocities was constructed for both data sets, for which goodness of fit statistics were calculated. The results of these calculations for depth-average currents are presented below in Table 18. From this table

we can see that for only tidal currents there is much better correlation between the measurements and the model, especially for the currents in cross-shore direction. Correlation coefficients increase from about 0.6 up to 0.8 at frame F1 and 0.9 at frame F4 and from 0.2 – 0.35 to 0.3 – 0.5 at frame F3. RMSE is also significantly reduced, from about 0.06 to 0.03 m/s at frame F1, from 0.1 – 0.15 to 0.06 – 0.11 m/s at frame F3 and from around 0.13 to 0.05 m/s at frame F4, while bias at all the locations becomes almost equal zero. From this table we can once again see small improvement in model performance going from 1 nm to 0.5 nm resolution.

Table 18 Statistics of the data-model comparison for depth-average tidal currents in longshore and cross-shore direction for three Ameland lower shoreface frames and three model versions (colours: green – better then model with a factor 2 lower resolution, yellow – same, red – worse)

Currents	Statistics	Longshore			Cross-shore		
		Frame 1	Frame 3	Frame 4	Frame 1	Frame 3	Frame 4
1 nm	R [-]	1.00	0.99	0.96	0.79	0.30	0.92
	RMSE [m/s]	0.07	0.08	0.15	0.03	0.11	0.04
	Bias [m/s]	0.00	0.00	0.00	0.00	0.01	0.00
0.5 nm	R [-]	0.99	0.99	0.99	0.81	0.48	0.88
	RMSE [m/s]	0.06	0.07	0.05	0.03	0.06	0.05
	Bias [m/s]	0.00	0.00	0.00	0.00	0.01	0.00

In the Appendix B, figures with comparison between the measured 10-minute-average velocity profiles and the results of the 0.5 nm DCSM-FM model for several time moments over a tidal cycle are presented for calm (Appendix B.1) and storm (Appendix B.2) conditions. For the period of calm conditions on November 15 (Figure A.4, Figure A.5, Figure A.6 and Figure A.7 corresponding to the phases of peak ebb, flood, peak flood and ebb) we can see that for all the time moments measured and modelled velocities in both longshore and cross-shore direction are very close for all three lower shoreface frames. However, for the period of storm conditions on November 19 (Figure A.8, Figure A.9, Figure A.10 and Figure A.11 corresponding to phases of peak flood, ebb, peak ebb and flood), when the observed significant wave height reached 5 m, we can see that for the longshore direction currents in the model are more westward over the entire water column compared to the measurements, particularly at frames F3 and F4. For the cross-shore currents measured velocities at almost all the time and all the frames are directed onshore over the entire water column, while in the model current changes from offshore to onshore over a tidal cycle. On the Figure 44 a comparison between measured and modelled M2 and S2 tidal ellipses, which were constructed based on the T_TIDE analysis, is presented. From this figure it can be seen that in the model tidal velocities in the longshore direction are generally overestimated and at shallower frames F3 and F4 certain difference in the inclination of the measured and the modelled tidal ellipses can be observed, which could be related to differences between the real and the model bathymetry.

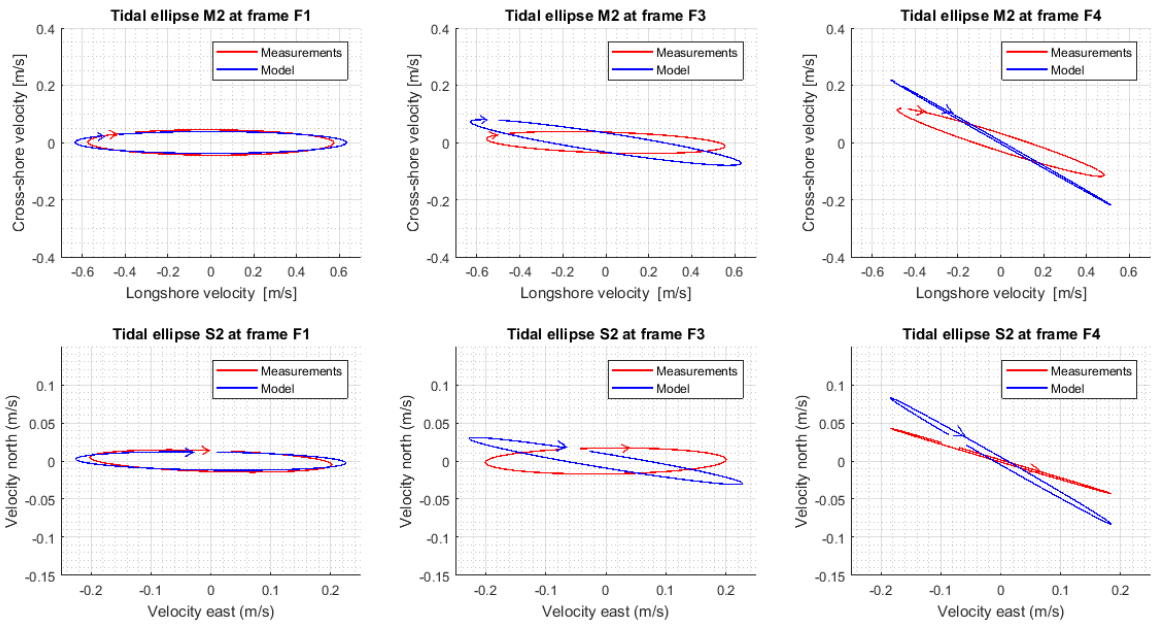

Figure 44 Measured and modelled M2 and S2 tidal ellipses for depth-average currents at the lower shoreface frames

5.3.2 RESIDUAL CURRENTS

In order to get better understanding of how well do different model versions reproduce non-tidal variation of the currents, residual currents were also calculated for the model output using the Fourier transform low-pass filter. In Figure 45 and Figure 46 comparison between depth-average residual velocities from different model versions and from the measured data in longshore and in cross-shore direction is presented. From these figures it can be seen that at frame F1 a good agreement can be seen between the measured and modelled currents in the longshore direction, while in the cross-shore direction a small onshore residual current, which can be observed in the measurements around storm events on November 11, 19 and 26 and December 9, is not present in the model results. As we move towards the coast and the water depth decreases, an increasing deviation between data and model results can be seen for both longshore and cross-shore currents during conditions with high waves. In the longshore direction measured depth-average residual current during storms can be up to 0.2 m/s higher than in the model results at frame F3 and even higher at frame F4, reaching 0.3 m/s during peaks of storm events. Besides that, with decreasing water depth deviation between measured and modelled currents in the longshore direction can be observed not only around most severe storm events, such as on November 11 and 19 when wave height reaches 4-5 m, but also for much lower waves, around 2 m at frame F4. As concerning the cross-shore currents, at shallower water measured landward residual flow during peaks of the storm events and smaller seaward flow afterwards are also not reproduced by the model and deviation between measured and modelled currents increases from about 0.1 m/s at 20 m water depth up to almost 0.3 m/s at water depth of 11 m during the moments of peak onshore flow. For the event on November 28, which stood out from the data analysis, model also shows quite different results for this period in comparison with other storm events. For this event model gives much higher velocities in longshore direction so the deviation from the data is much smaller and in cross-shore direction, as in the data, model does not show any onshore current. This suggests that the increased longshore current around that period was driven not only by the waves, which were smaller than during some other storm events that occurred during the KG2 field campaign, but mainly by the steady western wind, which was observed over a period of almost 6 days.

Comparing different model specifications we can conclude that, in general, both 1 and 0.5 nm model versions are very close to each other and give similar results in terms of reproducing the currents in storm conditions. The fact that model refinement did not result in significant changes suggests that the mismatch between the measured and modelled currents is not caused by inaccurate modelling of the exchange between the North Sea and the Wadden Sea system that comes from the lack of resolution and, consequently, too coarse bathymetry, but mainly results from absence of wave-induced currents in the model, which not only result in onshore and eastward longshore flow during storms driven by the radiation stress gradients, but also lead to the water level setup at the coast of the barrier islands of Ameland and Terschelling, which might also cause an increased current during storms due to pulling of the water through the inlet. This is also confirmed by the fact that at the deepest location of 20 m water depth modelled and measured currents in the longshore direction show very good agreement, which suggests that at this water depth waves of 5.5 m and less are not breaking as it is the only mechanism that is not included in the model and can result in mismatch between the measured and modelled currents in the longshore direction. However, in the cross-shore direction, a small onshore current is observed in the measurements and is not captured by the model. Because the wave breaking is not present at this water depth, this onshore current should be driven by another mechanism. This could be related to an effect of the tidal inlet "pulling" more water in during storms due to higher water levels due to wave and wind setup on the barrier islands and ebb-tidal delta, which affect also deeper water during severe storm events.

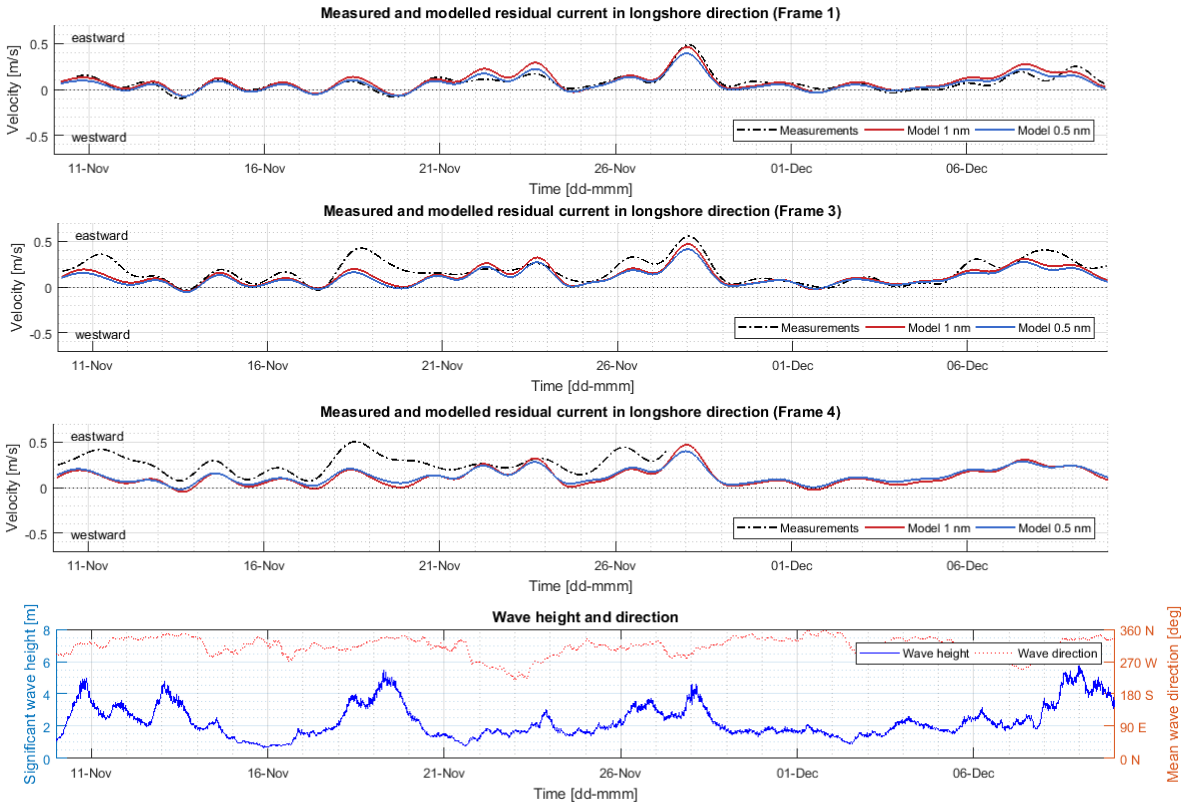

Figure 45 Measured and modelled (DCSM 1 and 0.5 nm) depth-average longshore residual currents at the lower shoreface frames

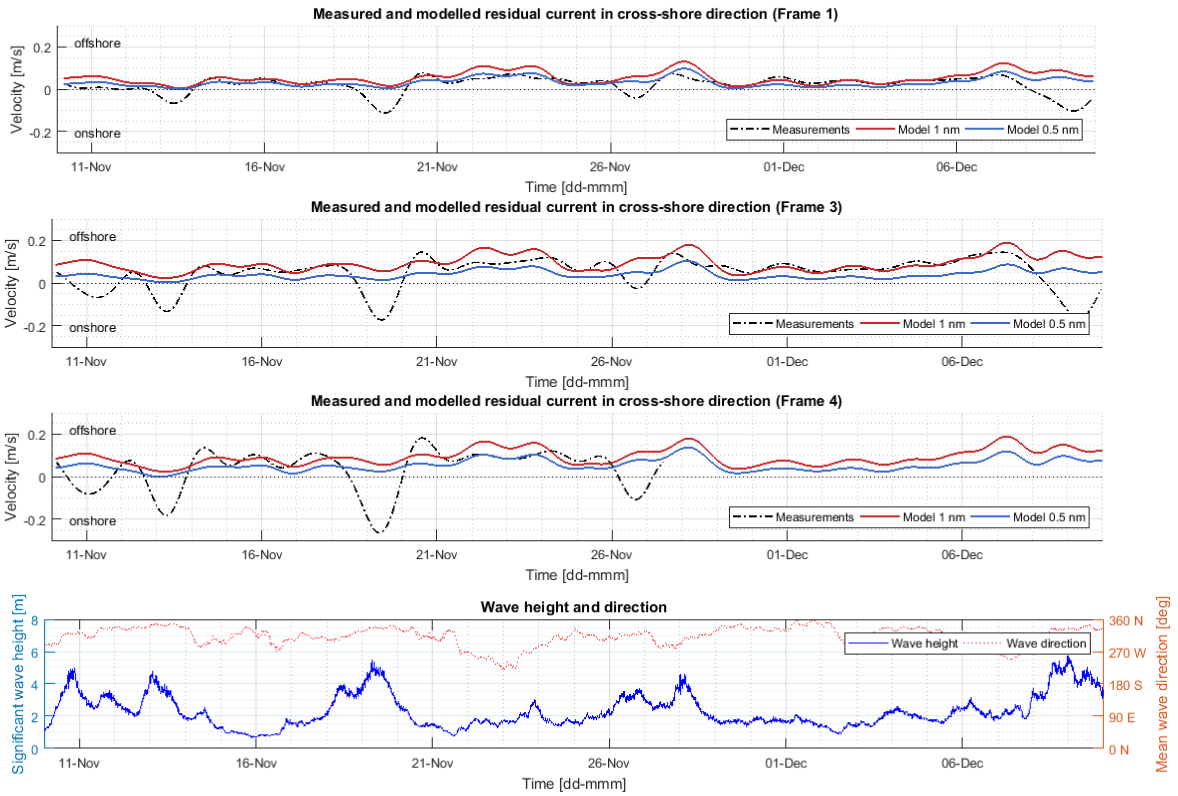

Figure 46 Measured and modelled (DCSM 1 and 0.5 nm) depth-average cross-shore residual currents the lower shoreface frames

5.3.3 TIME-AVERAGE CURRENT PROFILES

Also, time-average current profiles were compared for the measured and modelled currents in longshore and cross-shore direction. This comparison is presented for frames F1, F3 and F4 in Figure 47, Figure 48 and Figure 49 respectively. From these figures it can be seen that at the deepest frame modelled longshore currents are quite close to the measurements, some deviation can only be seen in the upper part of the water column. However, as it becomes shallower both 1 and 0.5 nm model show significant underestimation of the time-average longshore velocities, as measured currents are about 0.1 m/s higher at frame F3 and 0.15-0.2 m/s higher at frame F4. This mismatch results from absence of strong eastward current during storms in the model, which was also observed in residual current time series. For the currents at two shallower frames we can still notice that model results get slightly closer to the observed longshore currents with increasing model resolution, which is probably related to better representation of the actual bathymetry in the model. For the cross-shore direction we can see that the shape of the modelled average velocity profile is slightly different from what was observed in the data. According to the model, current is mainly directed offshore and the profile has more or less logarithmic shape with slightly more landward current near the surface and the profile shifts more offshore with decreasing water depth. Comparing it with the data we can see that, unlike modelled currents, measurements show much stronger onshore-directed current near the surface and slightly lower offshore average current near the bed.

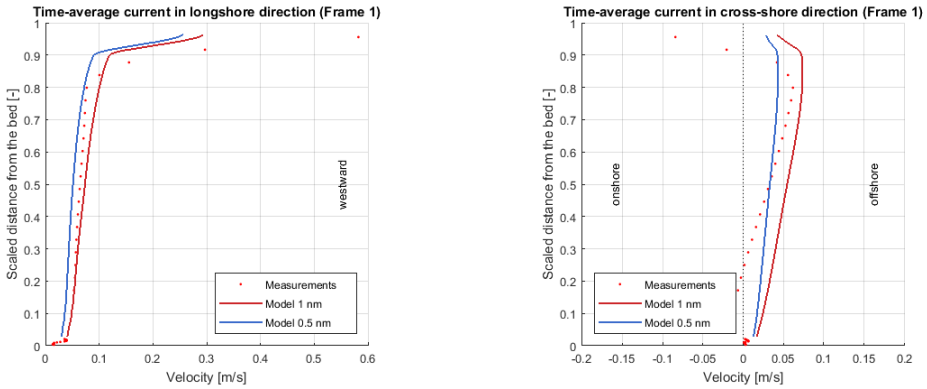

Figure 47 Measured and modelled (DCSM 1 and 0.5 nm) longshore and cross-shore residual velocity profile at frame F1

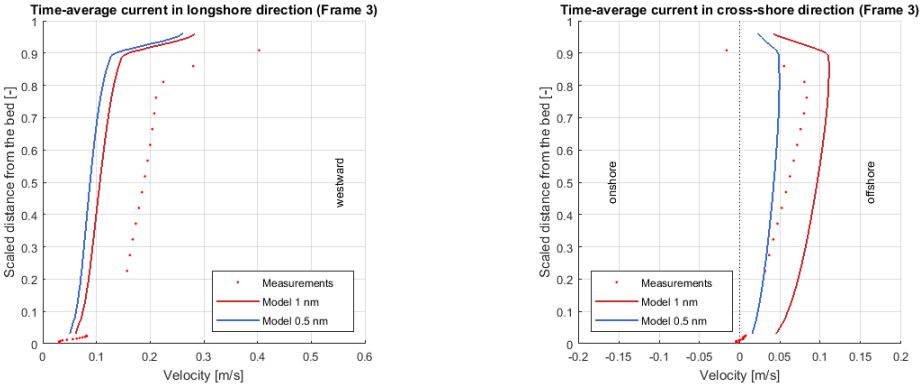

Figure 48 Measured and modelled (DCSM 1 and 0.5 nm) longshore and cross-shore residual velocity profile at frame F3

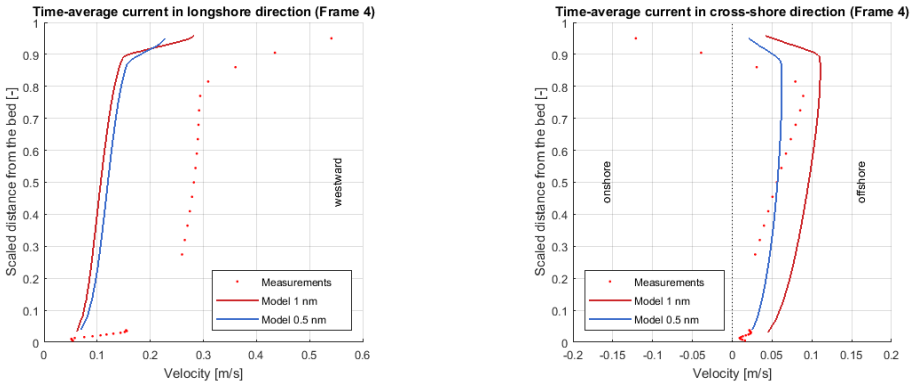

Figure 49 Measured and modelled (DCSM 1 and 0.5 nm) longshore and cross-shore residual velocity profile at frame F4

5.4.4 SENSITIVITY TO THE MODEL BATHYMETRY

Because in the calibrated 1 and 0.5 nm versions of the DCSM-FM model the older bathymetry data from 2011 is used for the area near the Ameland tidal inlet an additional model run was done with the bathymetry data from the year 2017, which was also used in the detailed Delft3D model, in order to assess sensitivity of the results. Comparison of the goodness of fit statistical characteristics for the 0.5 nm model versions with 2011 and 2017 bathymetry is presented in Table 19 for water levels and in Table 20 for depth-average currents for all three frames on the lower shoreface. From the first table we can see that change in the bathymetry leads to an improvement of the model performance, but the effect is relatively small. Correlation coefficients for both

water level stations as well as uRMSE value at station TNZ remain the same, while uRMSE at Nes and bias at both stations reduce by 0.01 m. From second table we can see that bathymetry effect on the model currents is also very small. Correlation coefficients for the longshore currents do not change, while for cross-shore currents it slightly increases at frames F1 and F4 and decreases at F4. Change in RMSE and bias is less than 0.01 m/s for all the frames except F4

Table 19 Sensitivity of the 0.5 nm DCSM-FM model water levels (September – December 2017) to the changed model bathymetry (colours: green – better then model with old bathymetry, yellow – same, red – worse)

Station	Statistics	Bathymetry	
		2011	2017
Terschelling Noordzee	R [-]	0.99	0.99
	uRMSE [m]	0.08	0.08
	Bias [m]	0.38	0.37
Nes	R [-]	0.98	0.98
	uRMSE [m]	0.16	0.15
	Bias [m]	0.36	0.35

Table 20 Sensitivity of the 0.5 nm DCSM-FM model currents to the changed model bathymetry (colours: green – better then model with old bathymetry, yellow – same, red – worse)

Bathymetry	Statistics	Longshore			Cross-shore		
		Frame 1	Frame 3	Frame 4	Frame 1	Frame 3	Frame 4
2011	R [-]	0.98	0.97	0.95	0.54	0.34	0.62
	RMSE [m/s]	0.09	0.14	0.19	0.06	0.10	0.12
	Bias [m/s]	-0.01	-0.07	-0.14	-0.01	0.01	-0.01
2017	R [-]	0.98	0.97	0.95	0.56	0.28	0.65
	RMSE [m/s]	0.10	0.14	0.18	0.06	0.11	0.15
	Bias [m/s]	-0.01	-0.06	-0.13	0.01	0.01	0.05

5.4 DELFT3D MODEL LOWER SHOREFACE CURRENTS

From the validation of the DCSM-FM model currents by the KG2 measurements from the Ameland tidal inlet lower shoreface it is possible to conclude that there definitely is a mismatch between the data and the model during storm events, which is observed even in cross-shore currents at 20 m water depth and which increases towards the shallow water. However, this mismatch can result not only from absence of wave-driven currents in the model, but also from incorrectly reproduced exchange between the North Sea and the Wadden Sea due to too coarse model resolution. And, as it was shown in the Section 5.1, the refinement of the DCSM model grid in the area of the Wadden Sea requires recalibration of the model, which was not done due to time limitations. Because of that, in order to analyse the effect of resolution and the role of wave-driven currents, the results of the detailed Delft3D model simulations with and without the effect of waves were used, which will be presented in the current section.

In the Figure 50, comparison between the depth average velocities according to the measurements, 0.5 nm DCSM-FM model and Delft3D model with and without waves are presented for the storm event, which occurred between 18 and 20 November of 2017. From this figure it can be seen that the Delft3D model with waves at least partially captures the measured currents during storms, particularly more eastward current

during flood at frames F3 and F4 in the longshore direction and onshore current at all three lower shoreface current in the cross-shore direction. The depth-average velocities from the Delft3D model simulation without waves, however, are nearly the same as from the DCSM-FM model.

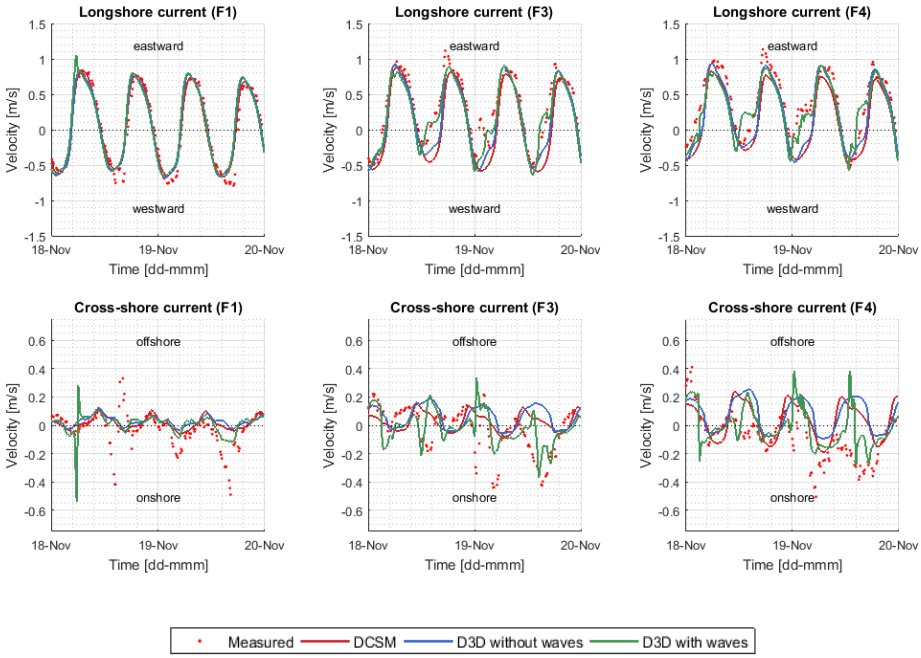

Figure 50 Measured and modelled (DCSM 0.5 nm, Delft3D with and without waves) depth-average currents in longshore and cross-shore direction at lower shoreface frames

In the Figure 51 and Figure 52, comparison between the depth-average residual currents is presented for the entire period of the KG2 field campaign. From the Figure 51, which shows the residual currents in the longshore direction, we can see that in the Delft3D model without waves depth-average residual velocity follows variation pattern as in the DCSM model, however, it has lower negative bias relative to the data, which is particularly visible at frames F3 and F4 during calm conditions and can be related to better representation of the actual bathymetry. For the storm events on November 11 and 18 it can be seen that Delft3D model with waves shows a small increase compared to the model without waves, but it also underestimates the measured current during the peak of the storm by 0.1-0.15 m/s at frame F3 and 0.15-0.2 m/s at frame F4. Different effect is observed for the event on November 28, for this period the DCSM model shows better results compared to the Delft3D model both with and without waves, while Delft3D model with waves shows the worst results compared to the data. And, because it was concluded previously that the longshore current increase during this period is largely wind-driven, an explanation for this could be that in the DCSM model the large scale effects of the atmospheric forcing (wind and pressure) over area of the North Sea and north-western part of the European continental shelf are directly resolved in the model. In the Delft3D model wind and pressure effects are also included. However, because its domain is limited only to several tidal inlets of the Dutch Wadden Sea, reproduction of the large-scale hydrodynamics also depends on the boundary conditions derived from the DCSMv6ZUNOv4 model (Zijl et al., 2013), which might be the source of this mismatch.

From the Figure 52, in which measured and modelled depth-average residual currents are presented, it can be seen that for the calm conditions the DCSM and Delft3D model results are very close to each other and to the data, with the Delft3D model giving slightly better results at the frames F3 and F4. For the storm events it can be seen that the Delft3D model with waves captures some part of the onshore residual flow, but still the mismatch with the data during peaks of the storms is relatively large: up to 0.1 m/s at frames F1 and F3 and 0.2 m/s at frame F4. After the storms mismatch between the data and the Delft3D model with waves is also observed in the residual offshore-directed current of about 0.05 m/s at frame F3 and 0.1 m/s at frame F4.

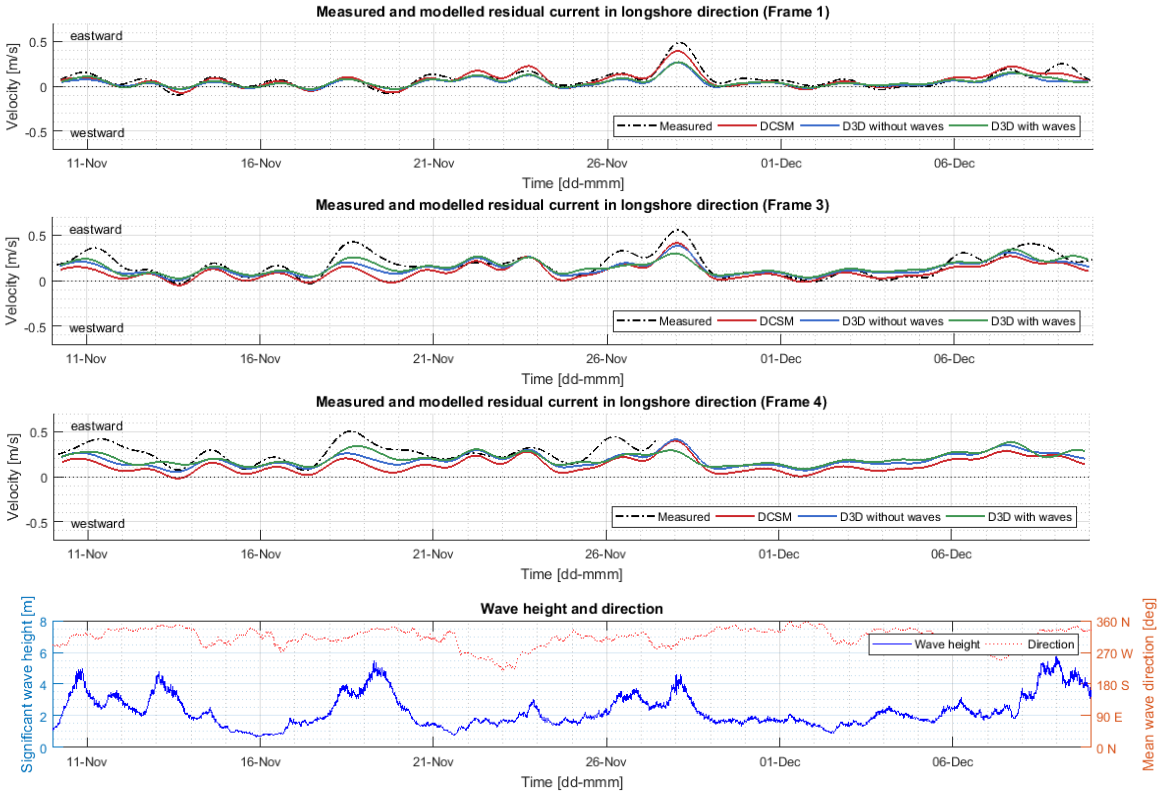

Figure 51 Measured and modelled (DCSM 0.5 nm, Delft3D with and without waves) depth-average longshore residual currents the lower shoreface frames

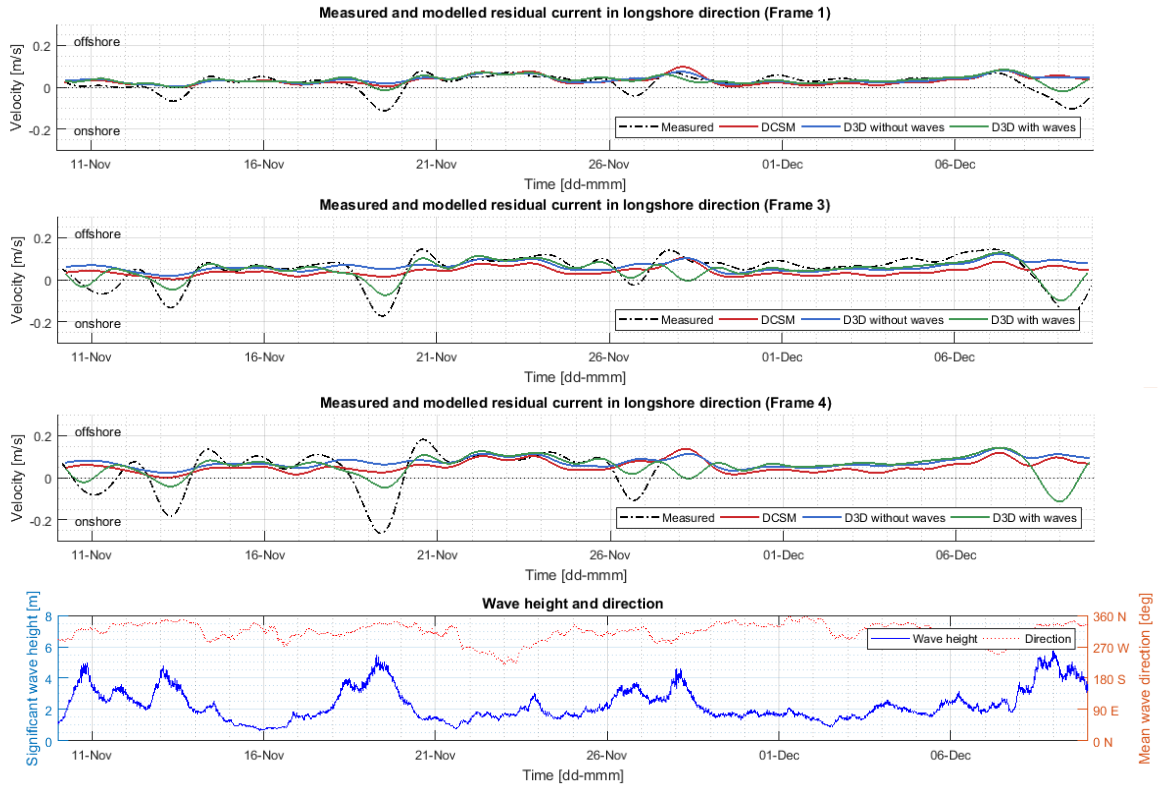

Figure 52 Measured and modelled (DCSM 0.5 nm, Delft3D with and without waves) depth-average cross-shore residual currents the lower shoreface frames

5.5 SEDIMENT TRANSPORT MODELLING

After validation of the DCSM-FM model with the new currents data from the KG2 field campaign, which has shown a certain mismatch between the data and the model, particularly during storm events, which increases at shallower water, the TSAND model was used to compute sediment transport rates at the locations of the measurement frames. In order to make a conclusion about the validity of the offline sediment transport modelling approach for analysing the net annual sediment transport on the lower shoreface of the Ameland tidal inlet, sediment transport rates for the period of the KG2 field campaign were calculated using different input, in particular measured and modelled currents, in order to assess the effect that observed data-model mismatch in currents has on the TSAND results. Computed sediment transport rates were then compared to the net annual values, calculated using only the modelled currents in order to evaluate the importance of the mismatch in predicted transport on a scale of a full year and make a conclusion about applicability of the method.

5.5.1 SENSITIVITY TO THE INPUT CURRENTS

To assess the influence of the input currents, total sediment transport rates in longshore and cross-shore direction calculated from modelled DCSM-FM currents were compared with the TSAND results obtained for the measured currents for the period from 9 to 29 November 2017. Input wave conditions were derived from the wave transformation matrix for the coordinates of the frames. Results are presented in Figure 53 for the 1 and 0.5 nm model versions. From this figure it can be seen that TSAND gives significantly different results for measured and modelled input currents. In the longshore direction for both measured and DCSM-FM currents the total sediment transport is directed to the east increasing towards shallow water. Results for different model versions for the longshore transport are more or less similar. For the deepest frame (F1) measured and modelled currents show the best agreement. The 0.5 nm model currents give total transport values very close to the one from the measured currents, while 1 nm model shows a small overestimation of the total longshore transport. The coarser 1 nm model input also gives slightly transport at F3 than at the shallower frame F4. This is because in this model these two frames are located within the same cell, so input currents for them are identical, while wave conditions derived from wave transformation tool are different. The wave height at the shallower frame is slightly lower, which results in smaller total transport. Transport rates, calculated from the 0.5 nm model, steadily increase towards shallow water, however, already at frame F3 values, obtained from the modelled currents, are slightly lower compared to the results for the measured currents and this deviation significantly increases at shallowest frame F4, at which modelled currents almost 4 times lower total transport than measured currents.

For the cross-shore direction it can be seen that absolute values of the total sediment transport are much lower, compared to the ones in the longshore direction. Besides that, using measured and modelled currents as input for TSAND gives different direction of calculated total cross-shore sediment transport. For the measured currents sediment transport is directed onshore at all three frames and significantly increases towards the shallow water. For DCSM-FM modelled currents, however, total transport shows only very small variation between deep and shallow water and the direction changes from offshore to onshore depending on location and the model resolution. The input currents from the 1 nm resolution model give offshore-directed sediment transport around 3 m^3/m at all three frames with the highest transport rates at frame F3 for the same reasons as for longshore currents. Currents from 0.5 nm model give small offshore transport of less than 1 m^3/m for frame F1 and towards frame F4 it changes to 2.7 m^3/m in the onshore direction, which is however much lower than TSAND gives for the measured currents.

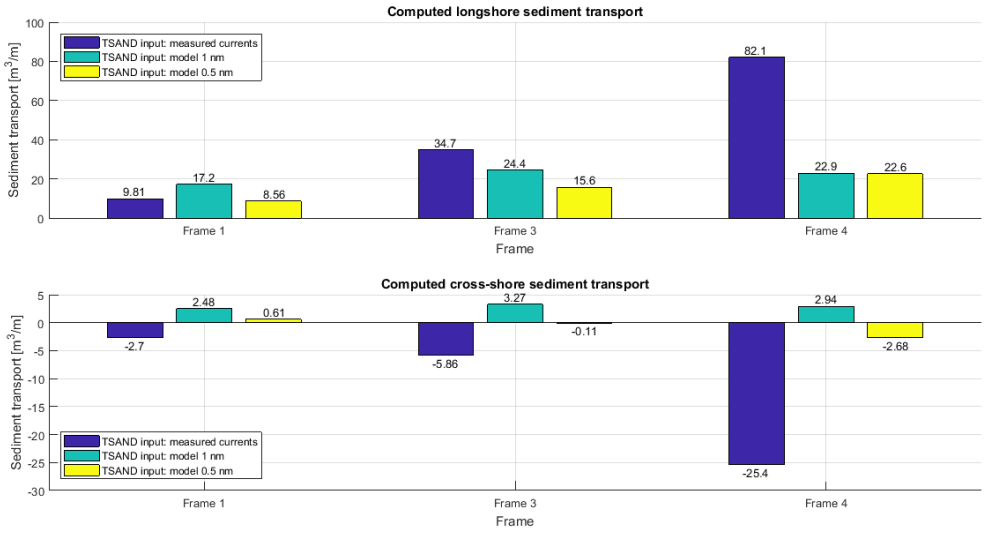

Figure 53 Integrated total longshore and cross-shore sediment transport, computed from measured and modelled currents at the KG2 frames locations for a period from 9-29 November 2017

These transport results for the period of the KG2 campaign correspond to the differences between measured and modelled currents, which were analysed in Section 5.3 and have shown that the DCSM-FM model underestimates the eastward longshore current at frames F3 and F4 and does not capture the landward cross-shore current at all three lower shoreface frames during storm events. The mismatch can be also seen in the predicted total sediment transport time series, which are presented in Figure 54 and Figure 55 for longshore and cross-shore direction respectively.

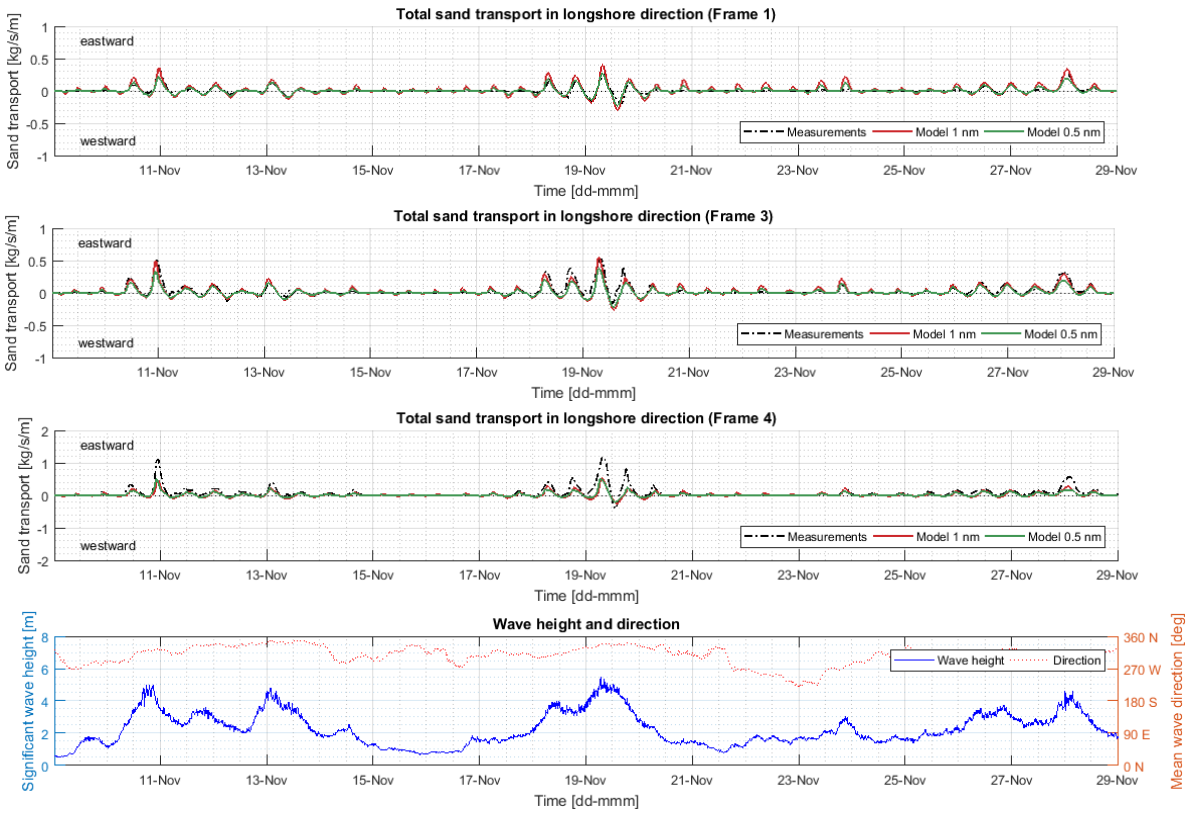

Figure 54 Total (bed and suspended load) transport time series calculated using TSAND from measured and modelled (1 nm and 0.5 nm models) currents in longshore direction

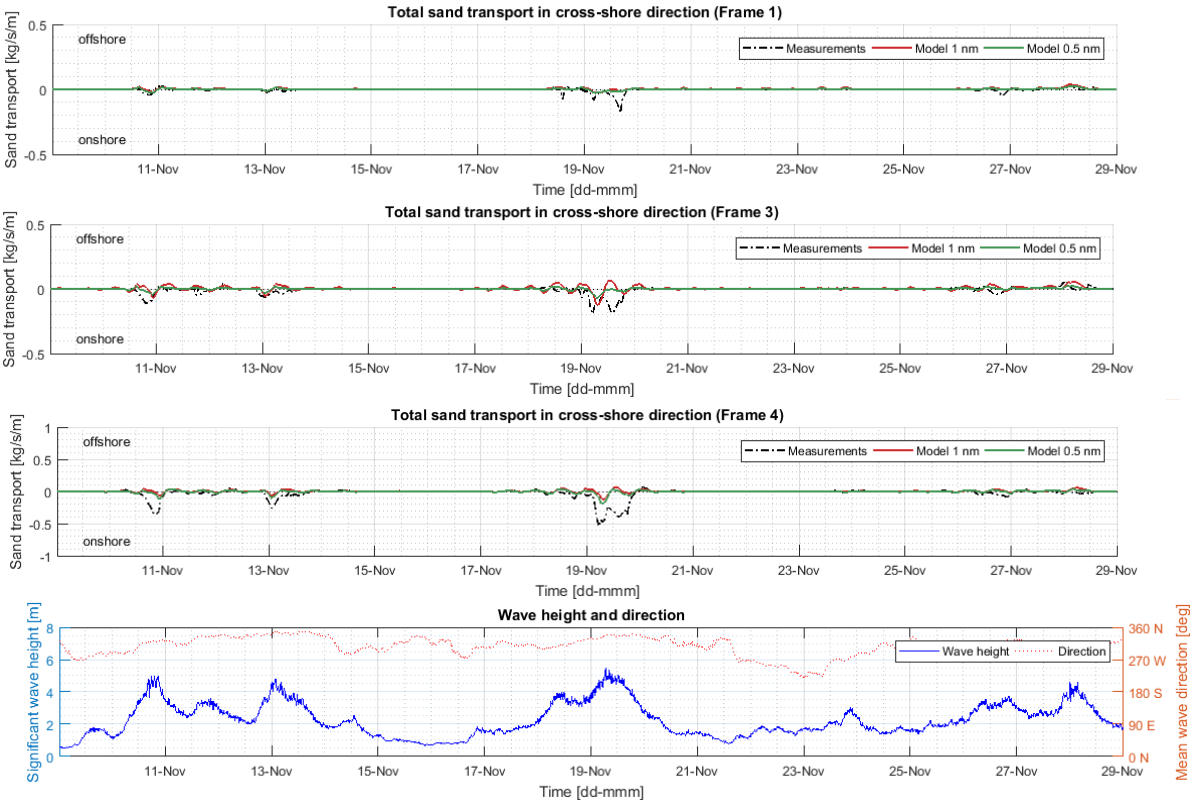

Figure 55 Total (bed and suspended load) transport time series calculated using TSAND from measured and modelled (1 nm and 0.5 nm models) currents in cross-shore direction

In the Figure 56 time-integrated sediment transport in the longshore and cross-shore direction divided into positive and negative contribution (eastward/westward for longshore and offshore/onshore for cross-shore) is presented for different classes of significant wave height. Wider and more transparent bars in the figure represent the transport calculated by TSAND from the 0.5 nm DCSM-FM model currents, while more narrow bright bars correspond to the transport rates determined from the measured currents. The net transport per wave class, which is a sum of the positive and negative bar, is presented as a dashed line for the transport calculated from the modelled currents and as a solid line for the transport rates calculated from the measured currents. From this figure it can be seen that at deeper water (frame F1) positive and negative transport as well as the net transport, calculated from the measured and modelled currents, are close for all the wave classes of the longshore transport and for waves lower than 2.5 m for the cross-shore transport. For waves higher than 2.5 m, measured currents start to give onshore-directed net transport, while for modelled currents the net transport is still in the offshore direction, which changes to small onshore transport only for waves higher than 4 m. Moving towards shallow water general picture for the cross-shore transport per wave classes remains the same. However, deviation is observed for low waves as measured currents give higher offshore transport rates compared to the modelled currents and this deviation starts to be visible for lower wave heights as it becomes shallower: for wave height of more than 1.5 m at frame F3 and more than 0.5 m at frame F4. Wave height values when the modelled currents start to show an onshore transport reduces with decreasing water depth (from 4 m at frame F1 to 3.5 m at F3 and 3 m at F4) and the net sediment transport values also increase, but the deviation from the transport calculated from the measured currents, which is observed for high waves, still increases towards the shallow water.

For the longshore transport it can also be seen that the deviation the TSAND results for the measured and modelled currents increases towards the shallow water. But, compared to the cross-shore transport, the wave class for which the highest deviation is observed is significantly different. For the cross-shore net transport the highest deviation can be seen for the waves between for the wave class of 4 to 4.5 m, which were observed

only about 2.5% of the time. For the longshore transport, however, the highest deviation is observed for waves of 2-2.5 and 2.5-3 m, which in total are observed for approximately 28% of the time. This corresponds to what is observed from the time series of the total sediment transport in the cross-shore (Figure 55) and longshore (Figure 54) direction as in the first case sediment transport is observed only at the moments of storm peaks, while in the second case it is also observed over the storm increase and decrease. This happens because in the longshore direction tidal currents are much stronger with velocities varying from about -0.8 to 1 m/s, while in cross-shore direction absolute velocity values reach 0.5 m/s only during high waves . As a result, in the longshore direction bed shear stress values are higher compared to the ones in the cross-shore direction even when the waves are relatively low, which results in significant sediment transport being present for longer periods of time.

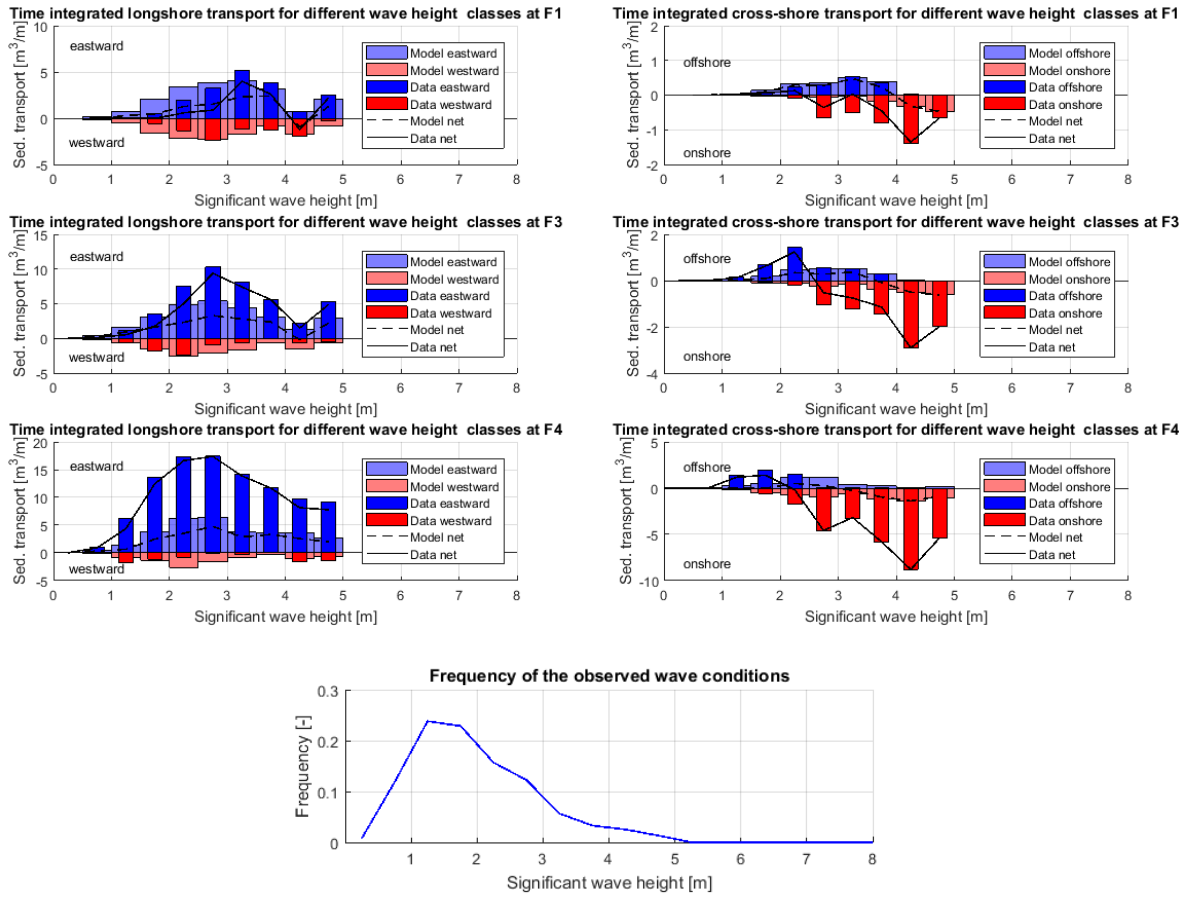

Figure 56 Time-integrated longshore (eastward and westward) and cross-shore (northward and southward) sediment transport calculated using TSAND from measured and modelled currents corresponding to different significant wave height classes and frequency at which particular wave height class was observed

In the Figure 57 a relation between the time-integrated bedload (bright red and blue) and suspended load (transparent red and blue) sediment transport computed by TSAND from the modelled and the measured currents for the period of the KG2 field campaign is presented. Numbers indicate the total sediment transport rates. From this figure it can be seen that the bedload transport values, determined by different current input, are much closer to each other than the total transport and the deviation only slightly increases at shallow water. The main difference between the sediment transport between the measured and the modelled currents arises from the suspended load transport. In the total transport calculated from the measured currents its role significantly increases as the water depth decreases, while for the modelled currents it also increases, but much slower. Besides that, for the cross-shore direction the net suspended load transport calculated from the modelled currents is directed offshore, while bedload transport is in the onshore direction.

This happens because bedload transport, which is observed during storm events, occurs only in one direction corresponding to the direction of waves (longshore eastward and onshore), while suspended load transport can be in both directions, similarly to the currents, (time series of the bedload and suspended load transport calculated from the modelled and the measured currents are presented in Appendix C.). And because the cross-shore residual current in the model is mainly directed offshore and is almost not affected during storms, it results in the onshore directed net suspended load transport.

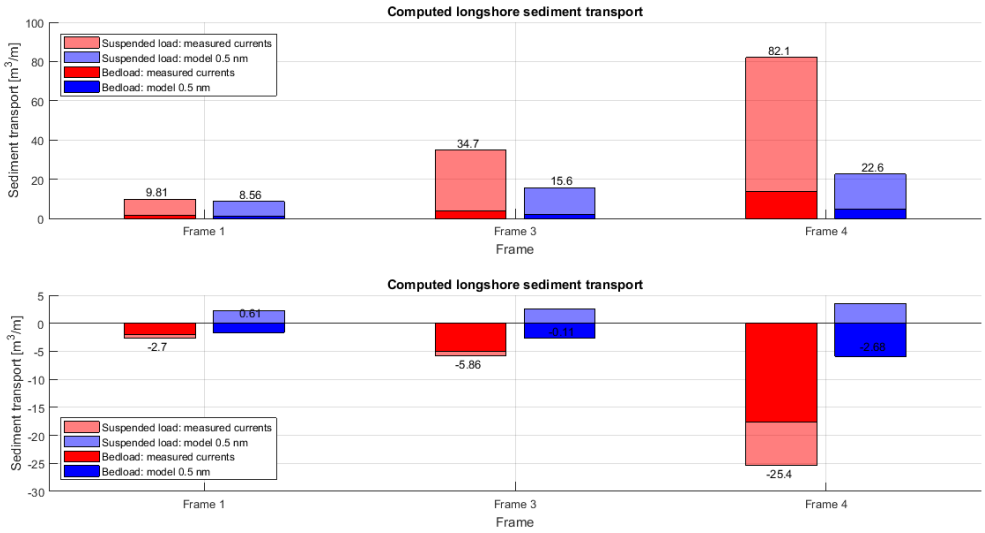

Figure 57 Bedload and suspended load contribution to the integrated total longshore and cross-shore sediment transport, computed from measured and modelled currents at the KG2 frames locations for a period from 9-29 November 2017

5.5.2 SENSITIVITY TO THE INPUT WAVE CONDITIONS

In order to assess the influence that input wave conditions have on computed sediment transport rates, TSAND calculations were performed for the period from 9 to 29 November 2017 for the measured currents with wave conditions from the AZB11 wave buoy, which is located at 20 m water depth, and from wave transformation table for the frame F1. Previously (Figure 21), it was shown that wave transformation tool tends to underestimate significant wave height, at certain moments by almost 0.5 m, and peak wave period, by about 2 seconds on average and going up to 5 seconds. Between three lower shoreface frames wave characteristics derived from the transformation table vary very slightly: wave height decreases towards shallower water by approximately 0.2 m from frame F1 to frame F4 and wave direction becomes more onshore by approximately 5°, while peak wave period in general remains the same and only at certain short periods it shows a decrease from deeper towards shallower water. Calculated sediment transport rates are presented in Figure 58 and from this figure it can be seen that different wave conditions have very small effect on total sediment transport at 20 m water depth in both longshore and cross-shore direction.

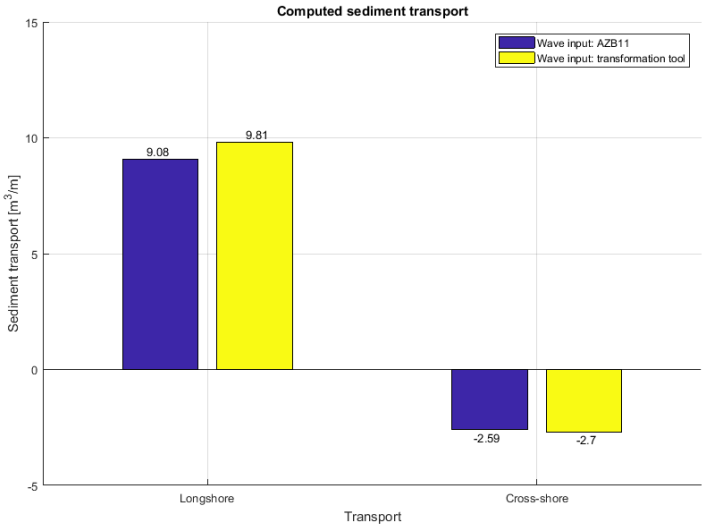

Figure 58 Integrated total longshore and cross-shore sediment transport at frame F1, computed from measured currents with input wave conditions measured at AZB11 wave buoy and derived using wave transformation table at the KG2 frames locations for a period from 9-29 November 2017

5.5.3 NET ANNUAL SEDIMENT TRANSPORT

In order to make a conclusion about the validity of the offline sediment transport modelling approach for the analysis of the net annual sediment transport on the lower shoreface of the Ameland tidal inlet, it was necessary to assess how important is the mismatch, observed between the transport rates predicted by TSAND from the measured and modelled currents, on a yearly time scale. For that reason, the net annual sediment transport rates were calculated using the 0.5 nm DCSM-FM model currents and wave conditions from the Wave Transformation Tool over a period of 5 years, from 2013 to 2017, as input for the sediment transport model. The resulting transport rates in the longshore and cross-shore direction are presented in the Figure 59. From this figure it can be seen that predicted values are in line with the transport rates, predicted from the model currents for the period of the KG2 November 2017 campaign. Longshore net annual transport is directed to the east and increases towards the shallow water, while cross-shore transport it is directed offshore at deeper water and becomes more onshore at shallower water.

Yearly variation in the net annual sediment transport rates, which is observed in the Figure 59, is related to the yearly variation in wind and wave conditions. As it can be seen from the Figure 60, the year 2013 was characterized by the lowest duration of storms with 0.01% exceedance significant wave height being less than 4 m and it is also characterised by the lowest longshore transport rates. From the Figure 61 it can be seen that the year 2015 compared to other years was characterized with more frequent and stronger winds coming from southeast, which resulted in relatively high offshore directed net annual sediment transport at all the locations on the lower shoreface predicted from the DCSM model currents. For the year of 2017, for which 0.01% wave height is about 7 m and most frequently observed wind direction was from the west, the modelled longshore eastward and onshore net transport is the highest.

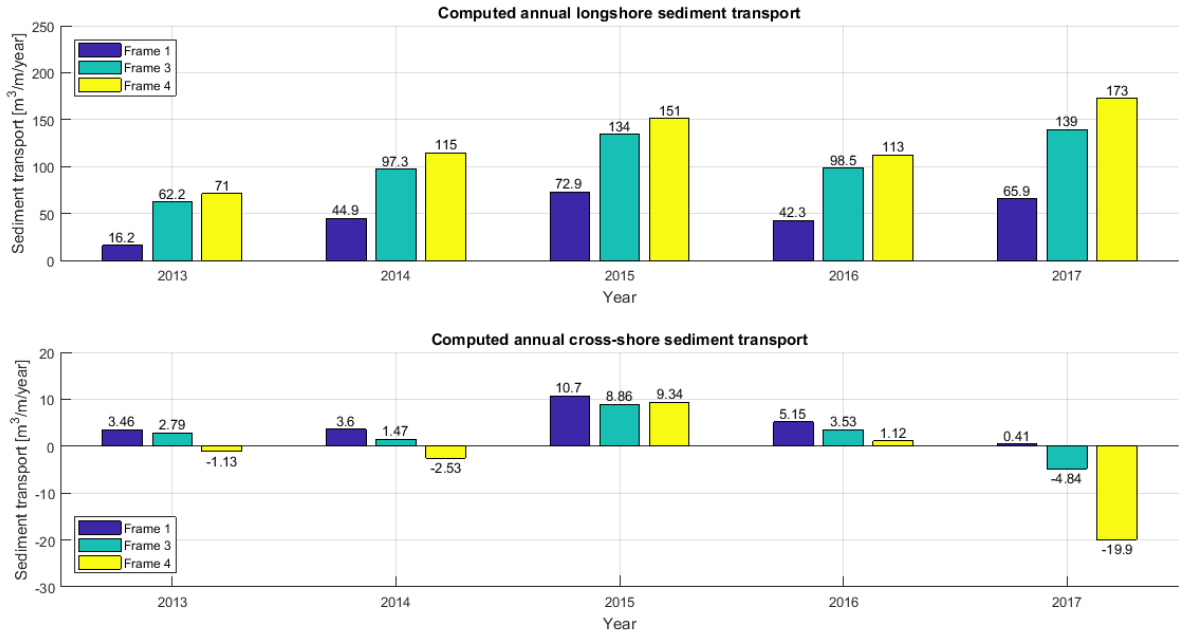

Figure 59 Net annual longshore and cross-shore yearly sediment transport rates computed at the KG2 frames locations for the period between 2013 and 2017 using the 0.5 nm model currents

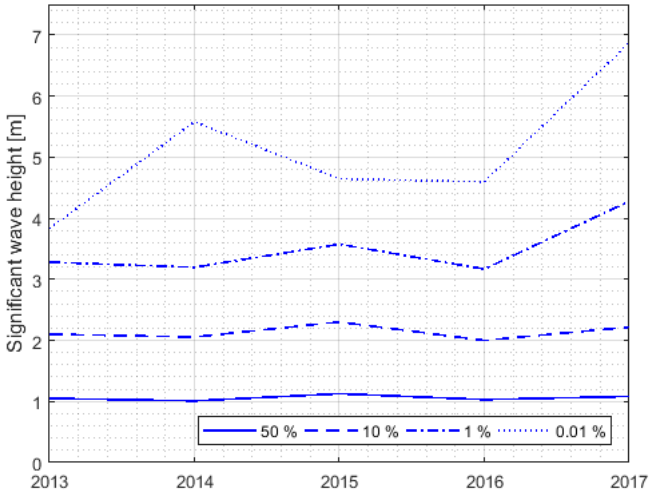

Figure 60 Yearly distribution of significant wave height with 50%, 10%, 1% and 0.01% exceedance probability at Eierlandse Gat station

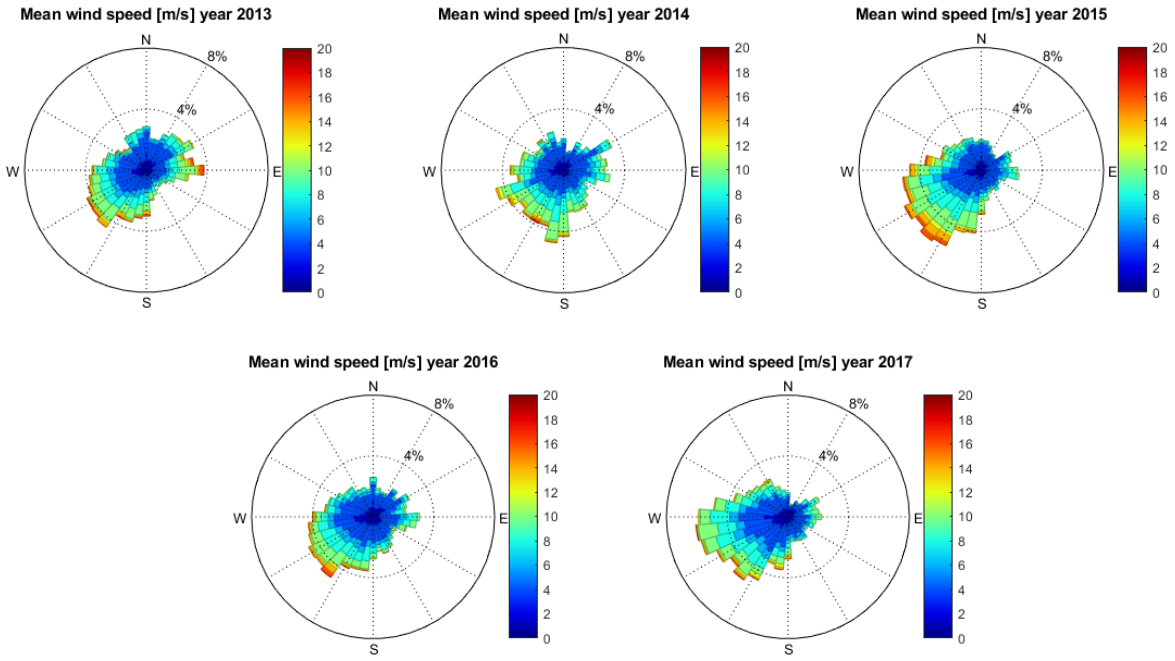

Figure 61 Yearly (2013-2017) wind roses at the station Hoorn (Terschelling)

However, if we compare the net annual transport rates calculated for the year of 2017 with the transport rates that were calculated from the currents measured during the KG2 campaign we can see that transport rates during this particular stormy period constitute a very significant part of the yearly transport. For the transport in the longshore direction at frames F1 and F3 the values predicted by the model for the entire year of 2017 and for the period of the field campaign are realistic, 10 and 35 m^3/m for the field campaign and 66 and 139 m^3/m for the year, which is, respectively, 7 and 4 times higher. For the shallowest frame F4 transport during field campaign constitutes more than a half of the net transport for the same year, 82 and 173 m^3/m respectively. The problem, however, can be seen from the transport rates in the cross-shore direction. For the period between 9 and 29 November of 2017 measured currents give total transport rates of 3, 6 and 25 m^3/m in the onshore direction at frames F1, F3 and F4 respectively, while modelled currents give nearly the same results for the entire year. Of course, the period of the field campaign is characterised by several large storms, however, even within this year there are several periods with even more severe storms (Figure 62).

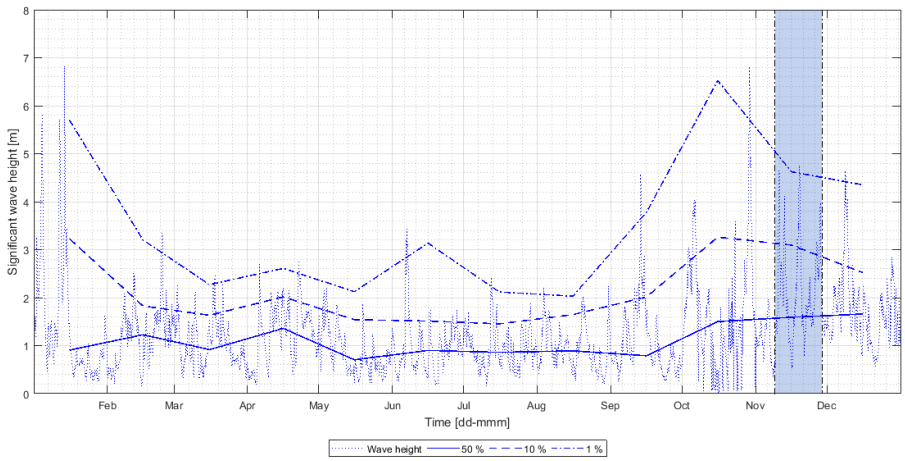

Figure 62 Significant wave height over the year 2017 and monthly distribution of significant wave height with 50%, 10% and 1% exceedance probability at frame F1 derived from the wave transformation tool

As a result, we can conclude that in its current state the DCSM-FM model currents cannot be used for calculating net annual sediment transport rates on the lower shoreface in front of the Ameland tidal inlet. This is the case not only for the shallower part, but also for the boundary of the coastal foundation, where during storms an onshore transport was observed in the data due to influence of the tidal inlet on the currents, which is not captured in the DCSM model. The importance observed difference of 3 m^3/m can be assessed using the following rough calculation. Assuming that there are 5 stormy months (150 days) a year, during which the sediment transport patterns are similar to the ones that were modelled for the 20-day period of the KG2 field campaign and the rest of the year the conditions are calm and there is no sediment transport present on the lower shoreface, yearly transport rates can be estimated by multiplying transport rates predicted from the measured currents by 7.5. This will give approximate yearly transport values of 75, 260 and 615 m^3/m longshore eastward and 23, 45 and 190 m^3/m onshore at frames F1, F3 and F4 respectively. For the cross-shore transport these values are almost an order of magnitude higher than were predicted from the DCSM model currents. For the length of the coastline of 50 km, which is approximately a sum of the widths of all the tidal inlets of the Dutch Wadden Sea, the cross-shore transport at 20 m water depth of 23 m^3/m/year will result in net transport of 1.15 million m^3/year constituting nearly 10% of the total yearly nourishment currently applied on the Dutch coast.

5.6 SENSITIVITY TO SEDIMENT CHARACTERISTICS

The results presented in the previous section were obtained for the value of the mean grain diameter d_{50} of 250 µm, which was used because it is the TSAND model default value and it approximately corresponds to the mean grain diameter for the Dutch coast. However, it can vary and according to the work of Eirsma (1968) at the area of Ameland and Terschelling the value is between 200 and 250 µm. Because of that, sensitivity of the sediment transport results to the input mean grain diameter was assessed by calculating sediment transport rates using TSAND with the values d_{50} of 200 and 300 µm, the results of which were then compared to the transport for the default value of d_{50} equal 250 µm for the period of the field campaign as well as for the period from 2013 to 2017 and net annual sediment transport rates. The comparison between transport rates during the period of the field campaign predicted with the default and with higher d_{50} value is presented on the Figure 63, and on the Figure 64 results are compared for the default and lower value of d_{50}. From these figures it can be seen that when the mean grain size is increased compared to the default the eastward longshore sediment transport from the measured currents almost does not change at the frame F1 and decreases by 7 and 5% respectively at frames F3 and F4. From the modelled currents the transport also decreases, but the relative change is slightly higher, 7 to 15%. In the cross-shore direction with mean grain diameter increase the transport rates are almost not affected, with the largest change of 1.5 m^3/m observed for the onshore transport at frame F4. Decrease of the mean grain diameter, on the other hand, had much stronger effect on the total sediment transport calculated the period of the field campaign. In the longshore direction both measured and modelled currents gave up to 30% higher transport rates at all three locations, while for cross-shore change in d_{50} has opposite effect on the results for measured and modelled currents. For the measured currents the net transport over the field campaign becomes higher in the onshore direction, while modelled currents show more offshore or smaller onshore net transport. This results from the fact that change in grain diameter has higher effect on suspended load compared to bedload and because the residual currents during storms in the DCSM model are directed offshore, reduced d_{50} leads to the net transport being in more offshore direction. On the Figure 65 and Figure 66 the comparison is given for the net annual sediment transport between 2013 and 2017 calculated from the DCSM model currents with increased and decreased mean grain diameter. From these figures we can see that the effects on a yearly scale are similar to the ones that were observed for the period of the field campaign, while the relative importance of the grain diameter change is higher. However, because the cross-shore transport at 20 m water depth for the field campaign almost does not change, while the yearly transport for 2017 is either 8 m^3/m/year offshore when d_{50} is higher or 2 m^3/m/year onshore when d_{50} is higher, which is still small compared to the yearly estimate based on the

data from the field campaign. Because of that, it can be concluded that mean grain diameter does not affect the conclusion made in the previous section about applicability of the offline sediment transport modelling approach.

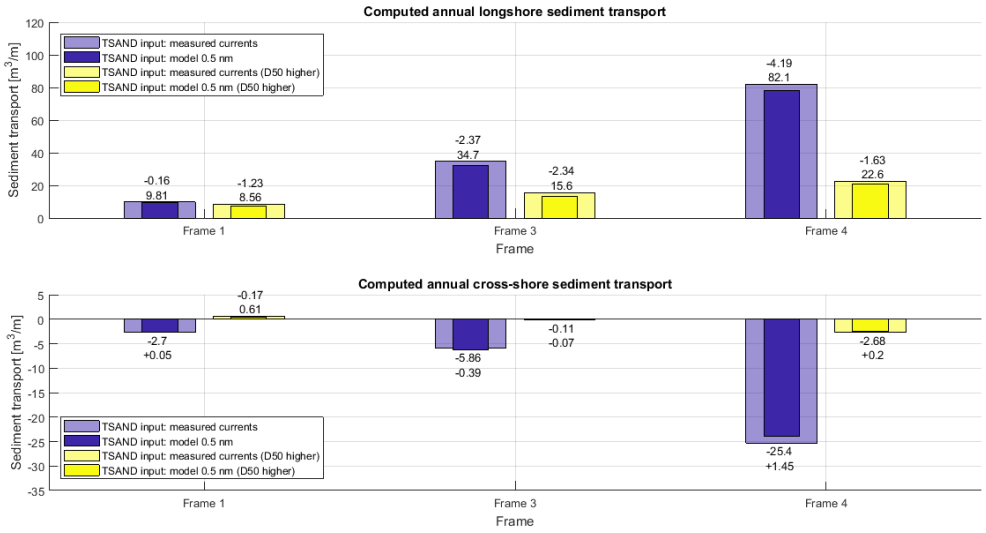

Figure 63 Integrated total longshore and cross-shore sediment transport with default $d_{50} = 250\ \mu m$ and with higher $d_{50} = 300\ \mu m$, computed from measured and modelled currents at the KG2 frames locations for a period from 9-29 November 2017

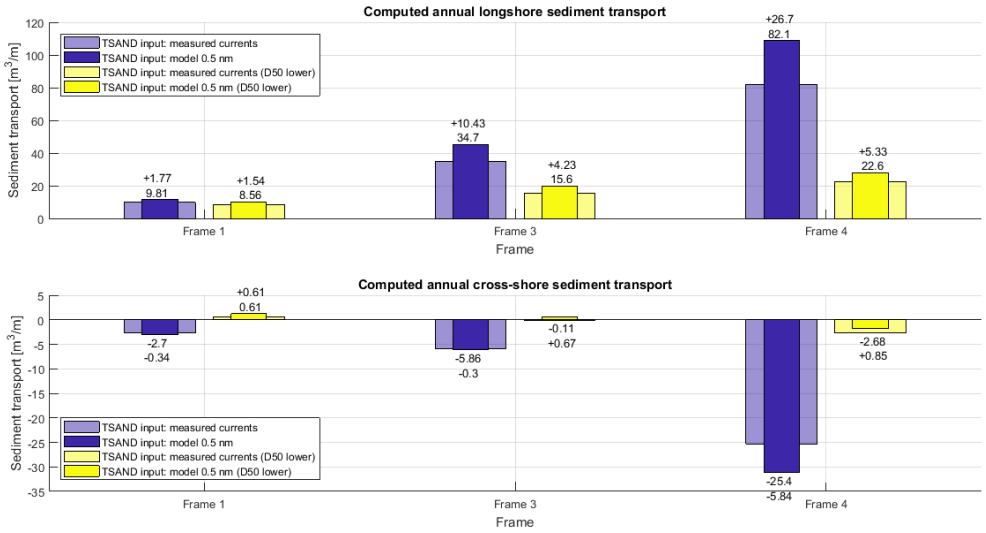

Figure 64 Integrated total longshore and cross-shore sediment transport with default $d_{50} = 250\ \mu m$ and with lower $d_{50} = 200\ \mu m$, computed from measured and modelled currents at the KG2 frames locations for a period from 9-29 November 2017

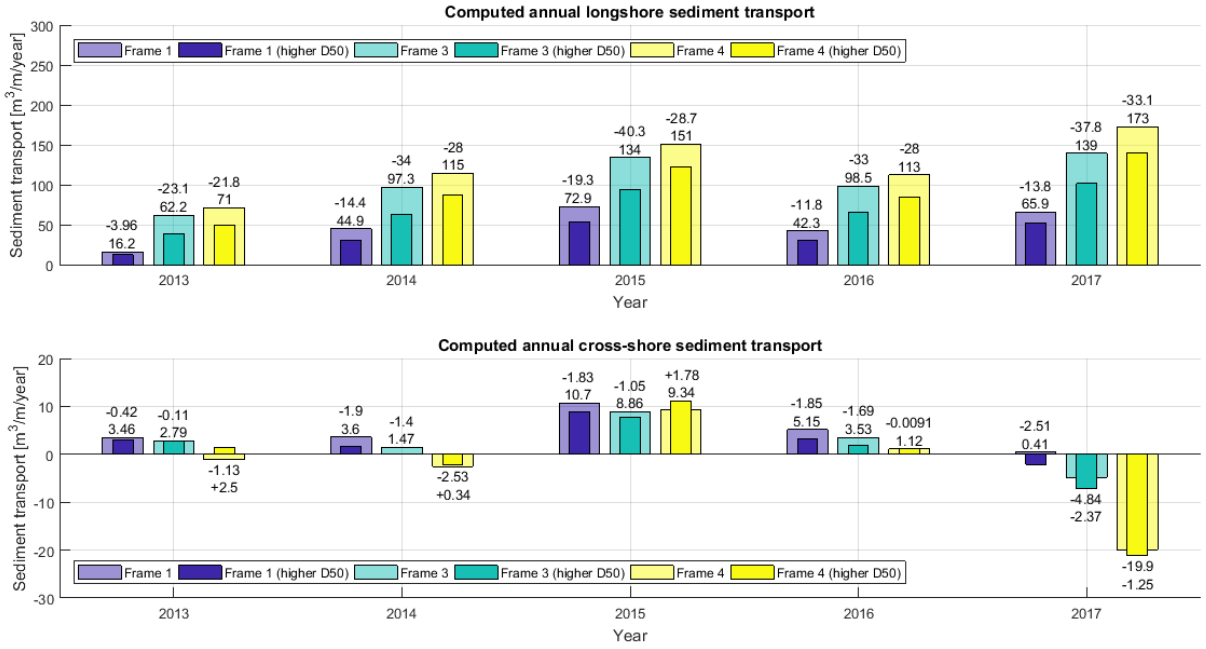

Figure 65 Net annual longshore and cross-shore yearly sediment transport rates computed at the KG2 frames locations for the period between 2013 and 2017 using the 0.5 nm model currents with default $d_{50} = 250\ \mu m$ and with higher $d_{50} = 300\ \mu m$

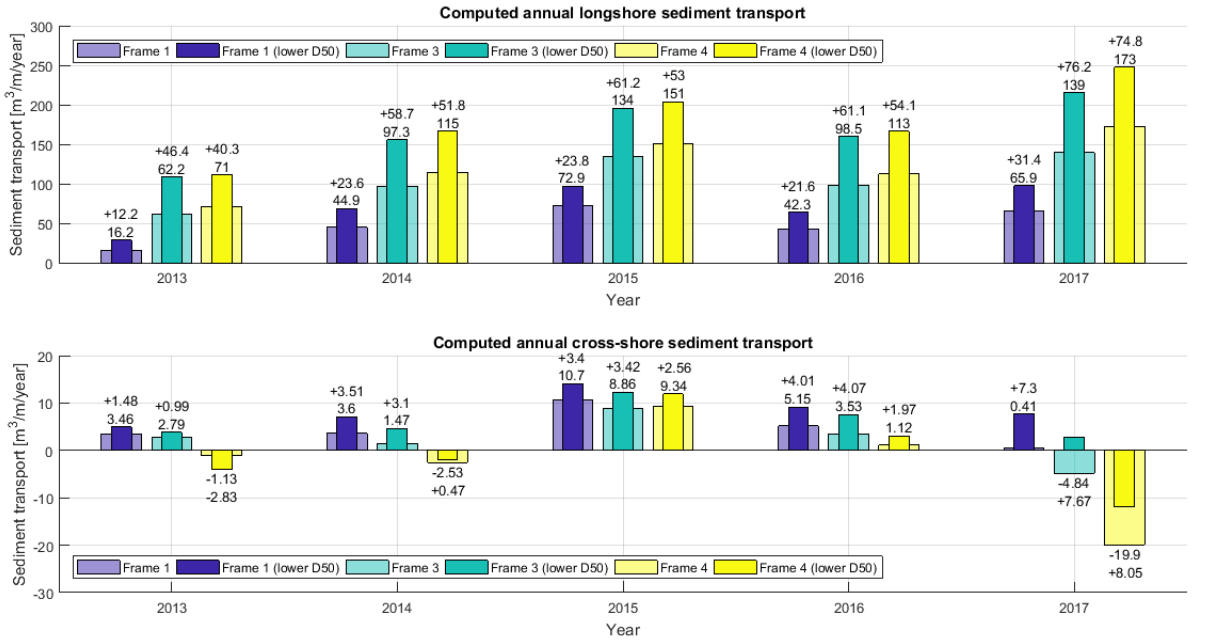

Figure 66 Net annual longshore and cross-shore yearly sediment transport rates computed at the KG2 frames locations for the period between 2013 and 2017 using the 0.5 nm model currents with default $d_{50} = 250\ \mu m$ and with lower $d_{50} = 200\ \mu m$

5.7 DISCUSSION AND CONCLUSIONS

The results of this chapter can be summarized in the following points:

DCSM-FM MODEL WATER LEVELS AND DISCHARGES THROUGH THE TIDAL INLET

- DCSM-FM model shows good correlation with the measured water levels inside and outside of the Wadden Sea for the year of 2017 with correlation coefficient higher than 0.97. Water level variation is reproduced with lowest uRMSE values of 0.09 m in the North Sea, which is in line with the results of Zijl et al. (2018), and 0.18 m in the Wadden Sea. The bias values, however, are relatively high, about 0.35 m for the 0.5 nm resolution, which is related to the fact that the vertical reference of the model is not clearly defined and to the way the model was calibrated to get the best possible reproduction of the water level variation in the North Sea.
- The model with 0.5 nm resolution gives slightly better results than the one with resolution of 1 nm, especially in the Wadden Sea. Refinement of the grid form 0.5 nm to 0.25 nm, however, gives lower bias, while the RMSE increases due to increase in tidal amplitude. This is related to the fact that in the 0.25 nm model the bathymetry representation did significantly change, particularly for the tidal inlet channels, which became deeper while the friction settings were used the same as for 0.5 nm model. This means that refinement that was done in the model requires a recalibration in order to properly compare its results with the other models, which was not possible to do within this master project due to time limitation. Because of that, in all the other sections only results of the 1 nm and the 0.5 nm model versions are compared.
- During storm events surge water levels are reproduced well in the North Sea, while in the Wadden Sea they are typically underestimated in the model by about 0.2 m, which suggests that there is not enough water flowing in the basin through the tidal inlet during storm conditions.
- Amplitude of the discharges through the Ameland tidal inlet is typically overestimated by the model, which is related to the bias in water levels. Exchange during calm conditions is also slightly overestimated.

DCSM-FM MODEL LOWER SHOREFACE CURRENTS

- In general, the DCSM-FM model demonstrates high correlation with the measurements for currents in the longshore direction with correlation coefficients higher than 0.99 at of 20 m water depth. Towards shallower water model accuracy steadily decreases as correlation coefficient goes down to 0.95 at 11 m water depth, while RMSE and bias significantly increase from 0.09 to 0.22 and from 0 to -0.17 m/s, respectively, meaning that closer to the coast velocity is on average underestimated by the model. For the currents in the cross-shore direction model shows much worse results than in the longshore in terms of correlation, especially for the middle frame F3, correlation coefficient varies between 0.3 and 0.6, while RMSE also increases from deep to shallow water from 0.06 to 0.12 m/s.
- For only tidal currents model performance is much better, with lowest correlation coefficient for the cross-shore currents of 0.48 and highest RMSE of 0.07 m/s, which suggests that the mismatch between measured and modelled currents is not related to tidal processes.
- Refinement of the DCSM model form 1 nm to 0.5 nm results in small statistical improvement in the modelled currents, in particular at frame F4 for longshore currents and at all three frames for cross-shore currents.
- Time-series of filtered currents show that during calm conditions model results are quite close to the measured currents, while deviation is mainly observed during storm events when high waves and strong wind are coming from direction between north and north-west. In the longshore direction residual currents are underestimated by the model during storms, especially at shallow water, while for cross-shore currents model does not reproduce onshore current during storms and slightly increased offshore current after storms.
- These patterns are similar for both 1 and 0.5 nm model versions, which suggests that the observed mismatch is not caused by the lack of resolution, but by the lack of the wave-driven currents in the model.

To make final conclusions about the effect of resolution and the role of wave-driven currents, the results of the Delft3D model were used.

- The effects of updating bathymetry at the Ameland tidal inlet from 2011 by 2017 data on the model results were shown to be small with change in RMSE and bias of 0.01 m or less for water level and 0.01 m/s or less for currents.

DELFT3D MODEL RESULTS AND WAVE-DRIVEN CURRENTS

- Comparison of the DCSM-FM model currents with the results of the detailed Delft3D model for the Ameland tidal inlet with and without waves has shown that the model with waves is able to capture to a certain degree the measured currents during storm events, while without waves the Delft3D model results are similar to the results of the DCSM model. From this it is possible to conclude that the mismatch between measured and DCSM model currents are not caused by the lack of model resolution, but indeed by the absence of wave-driven currents.
- The Delft3D model with waves, however, does not reproduce currents during storm events entirely, it performs much better than the DCSM model, but still underestimates the peak residual velocities in both cross-shore and longshore direction. This can be related to incorrectly reproduced effects of large-scale atmospheric forcing. This follows from the underestimated wind-driven longshore current peak on 28 November 2017, which is the only event over the period of the KG2 field campaign reproduced better by the DCSM model. Besides that, for this event at shallow water the detailed model with waves shows less accurate results than the same model without waves. Another possible reason for the mismatch could be the way wave-driven currents are defined in the model or the fact that the model does not take into account vertical velocity distribution, however, neither of these factors were investigated in detail within this master thesis project thus it can be treated more as a first guess.
- The fact that at the deepest location at 20 m water depth longshore currents from the models without waves show very good agreement with the measurements, while in the cross-shore direction a small onshore current is observed in the data during storms, which is not captured by the model, and because the longshore current due to wave breaking is the only mechanism that can result in the mismatch between currents in the longshore direction, it can be concluded that at 20 m water depth there is no wave breaking. This means that differences in cross-shore currents do not only result from direct onshore flow towards the inlet due to balance between radiation stress gradient and bed shear stress, but also due to some other mechanism related to wave-driven currents, which could be the effect of the tidal inlet “pulling” the water, which extends further during storms due to water level setup on the barrier islands and ebb-tidal delta.

SEDIMENT TRANSPORT MODELLING

- Comparison of the sediment transport rates calculated using TSAND from the measured and modelled by the DCSM model currents for the period of the field campaign has shown that, even though statistically the DCSM model performs relatively good, in the longshore direction at the deepest frame F1, modelled currents give values very close to the ones predicted from the measured currents, but as it becomes shallower they tend to give lower transport rates than the measured currents and the difference is highest at the shallowest frame F4. In the cross-shore direction measured currents give an onshore total sediment transport at all the locations significantly increasing towards shallow water, while DCSM model currents give small offshore transport at deeper water and small onshore transport – at shallower, but much smaller compared to the transport from the measured currents.
- Using the measured currents as TSAND input shows that sediment transport occurs mainly during storm events and during these events the main difference with the sediment transport, calculated using the

model currents, is observed. This is in line with the differences that were observed during validation of the DCSM model.

- Comparing the transport rates for different wave height classes has shown that for both measured and modelled currents net onshore transport is observed during high waves, while low waves correspond to a net offshore transport. The magnitude of the net transport and the wave class at which it changes direction are, however, significantly different and the difference increases towards shallow water. The largest mismatch in net cross-shore sediment transport is observed for waves between 4 and 4.5 m, which are observed 2.5 % of the time. In the longshore direction the net transport is directed eastward for all the wave height classes and it increases at shallow water, while the wave height at which deviation in the net transport rates from different input currents starts to be observed decreases. However, the largest mismatch in net transport now corresponds to the wave heights of 2-2.5 and 2.5-3 m, which in total are observed 28% of the time. This can be explained by the fact that in the longshore direction velocity magnitude is high, resulting in higher bed shear stress and sediment transport even at relatively low waves, while in the cross-shore direction similar velocities are reached only during severe storms.
- Sediment transport rates, predicted from the measured and the modelled currents, are closer for bedload transport, while deviation is mainly caused by differences in predicted suspended load transport.
- Differences between the measured wave conditions and conditions derived from the Wave Transformation Tool almost do not affect the sediment transport rates at 20 m water depth.
- Comparing the transport rates, calculated using TSAND from the modelled currents for the entire year of 2017, with the ones calculated using measured currents for the period of the KG2 field campaign it is possible to conclude that the wave-driven currents are very important for the net annual sediment transport on the lower shoreface, especially in the cross-shore direction, as the values for the 20-day period with waves are nearly the same as for the full year. Because of that, in its present state the offline sediment transport modelling approach cannot be used for analysing net annual sediment transport for the Ameland tidal inlet. This is the case even for the water depth of 20 m, where the yearly cross-shore transport from modelled currents is around zero and about 3 m^3/m onshore for the field campaign. From a rough estimation of the yearly transport from the transport during field campaign is can be seen that this mismatch can be significant for the determining the required nourishment volume of the Coastal Foundation.
- Change of the mean grain diameter does not affect the conclusions.

6. SEDIMENT TRANSPORT PROCESSES

Even though in the previous chapter it was concluded that the offline approach cannot be used to analyse the net annual sediment transport on the lower shoreface of the Ameland tidal inlet, it still was attempted to use it along with the measured currents to assess contributions of different physical mechanisms, such as wave-induced Longuet-Higgins streaming, Stokes drift, wave velocity asymmetry and wind-driven currents, to the net annual sediment transport. In the current chapter the net sediment transport rates predicted using TSAND with input measured and the 0.5 nm DCSM-FM model currents will be presented for the period of the field campaign and with input model currents for the period between 2013 and 2017. The transport rates were computed with and without taking into account different processes for the period of the field campaign in order to analyse how important are the wave-driven currents for assessing contributions of different transport mechanisms to the net sediment transport on the lower shoreface of the Ameland tidal inlet and, after that, the annual transport rates were assesses and compared the results to Van Rijn (1997) results for the Holland coast.

6.1 WAVE-INDUCED NEAR BED STREAMING

In order to assess the effect of the wave-induced Longuet-Higgins streaming on the predicted sediment transport rates, TSAND calculations were done without the additional analytically computed current, which is derived using the equation (21) presented in the Chapter 3 and is added to the total current velocities used to compute the bedload sediment transport. In the Figure 67 the time series of the additional near bed current velocities in longshore and cross-shore directions due to Longuet-Higgins streaming are presented. From this figure it can be seen that during storms, when significant wave height exceeds about 4 m, additional velocity can reach 0.05 m/s in the longshore eastward direction and 0.1 m/s in the onshore direction. All the sediment transport rates presented in the previous chapter were calculated with the effect of streaming included, but, as it can be seen form Figure 68, which demonstrates integrated sediment transport computed using the measured and the 0.5 nm DCSM model currents with and without additional analytically calculated streaming for the period of the field campaign, it has only very small effect on the results. In general, it can be seen that the change in transport rates when the streaming is excluded is in line with the additional current velocities. For the modelled currents the longshore eastward transport decreases by 0.05, 0.2 and 0.6 m^3/m at the locations F1, F3 and F4 respectively when streaming is not taken into account. Meanwhile, in the cross-shore direction the absolute value of the sediment transport decreases for all the frames by less than 0.1 m^3/m, becoming smaller offshore at F1 and smaller onshore at F3 and F4. This changes as well as the small effect can be explained by the fact that the Longuet-Higgins streaming affects only bedload transport and, as it was shown in the Figure 57 in Section 5.5.1, the bedload role in the total sediment transport on the lower shoreface is small. For the measured currents we can see that the effect of streaming is comparable with the effect observed for the modelled currents at the location of the deepest frame F1, while for the frames F3 and F1, at 16 and 11 m water depth respectively, change in the net transport due to streaming is slightly higher. This results from higher current velocities during storms when the wave-driven currents are taken into account, which leads to increased bed shear stress and higher effect of the additions streaming currents.

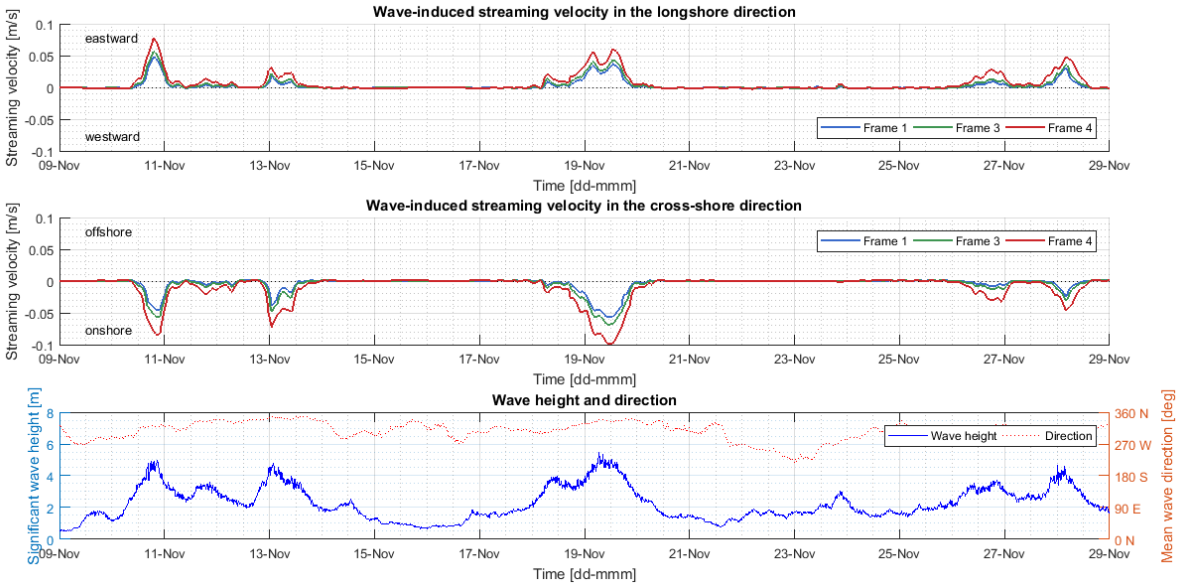

Figure 67 Computed wave-induced streaming velocity time series in longshore and cross-shore direction at the KG2 frames locations

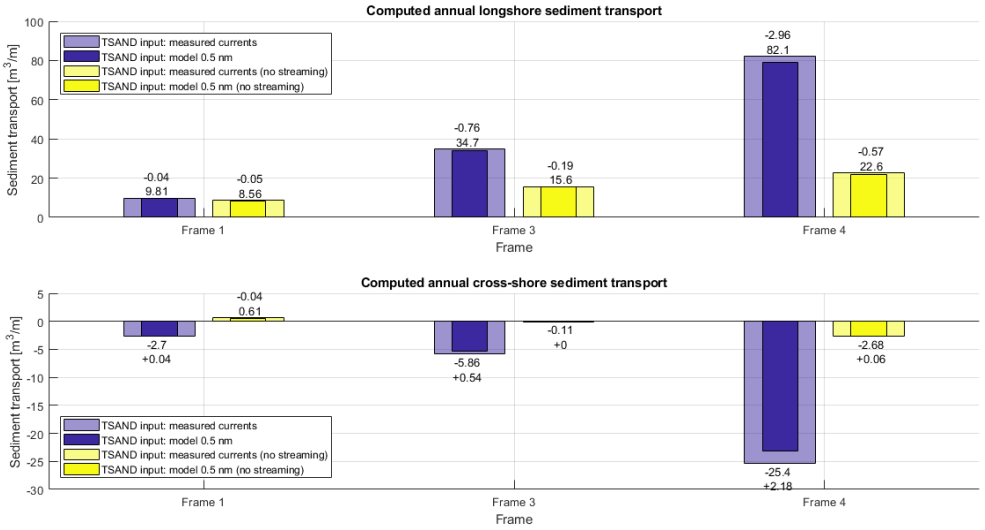

Figure 68 Integrated total longshore and cross-shore sediment transport, computed at the KG2 frames locations for a period from 9-29 November 2017 from measured currents, modelled currents from 0.5 nm and same modelled currents without additional streaming velocity

In the Figure 69 the effect of excluding wave-induced near bed streaming is presented for the net annual sediment transport comuted using the DCSM model currents. From this figure it is possible to conclude that on a yearly time scale streaming has also very small influence on the results. Depending on the year additional contribution for the net annual longshore transport in the eastward due to streaming are 0.5-1.5 m^3/m for the frame F1, 0.6-2.4 m^3/m for F3 and 1.1-4.4 m^3/m for F4. For the cross-shore direction the effect of streaming on net annual sediment transport is close to zero with a maximum of 0.4 m^3/m. However, as it was observed from Figure 68, in the presence of wave-driven currents the effect of streaming at 16 and 11 m water depth is higher than what is predicted from the model currents clearly driving a net onshore transport. Because of that, a conclusion can be made that at 20 m water depth Longuet-Higgins streaming almost does not contribute to the net annual transport, which is in line with the results of Van Rijn (1997) and in order to properly assess its contribution at shallower water wave-driven currents should be taken into account.

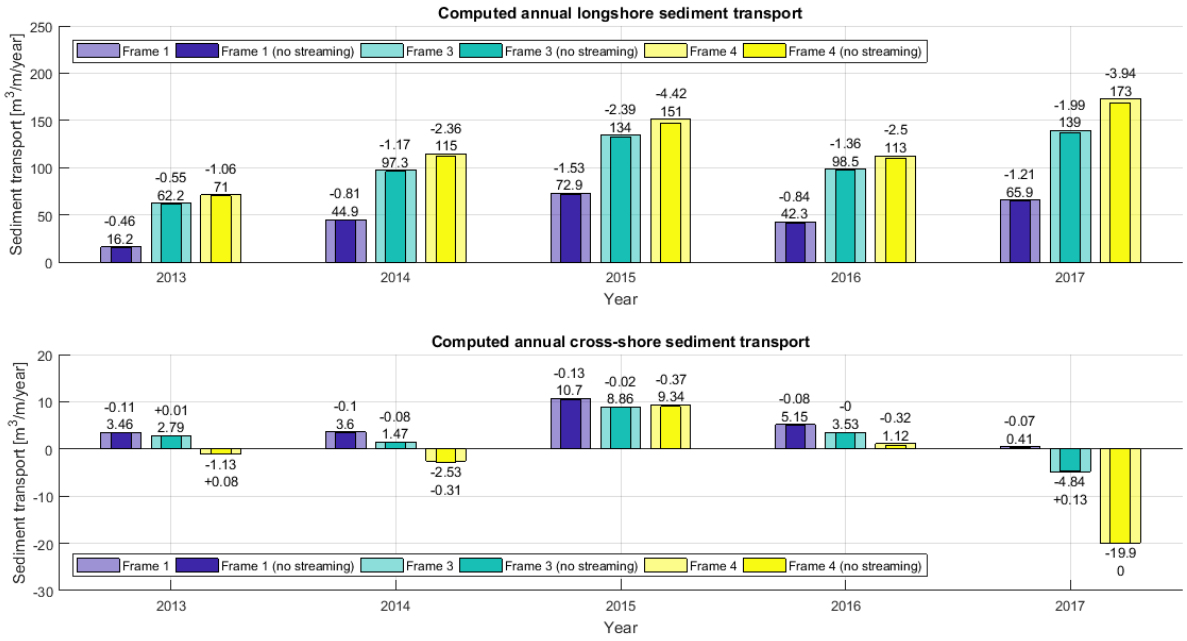

Figure 69 Net annual longshore and cross-shore yearly sediment transport computed at the KG2 frames locations for the period between 2013 and 2017 using the 0.5 nm model currents without the effect of streaming (numbers above the bars show reference transport rates and change due to excluding the effect of streaming)

6.2 STOKES DRIFT

In order to at least partly account for the non-inclusion of the wave-induced currents in the DCSM model, the TSAND model has an option to compute wave-related return current, which develops in case of an uninterrupted coast as a compensation for the pressure gradient generated due to the mass flux in the direction of wave propagation as a result of Stokes drift and the water level set-up. This return current is calculated using the expression for the depth-average Stokes drift velocity U_s:

$$U_s = \frac{M_s}{\rho h} \tag{22}$$

where h - water depth (m) and M_s – mass flux due to Stokes drift (kg/m/s), which can be calculated as:

$$M_s = E_w / c \tag{23}$$

$$E_w = \frac{1}{8}\rho g H_{rms}^2 \tag{24}$$

with E_w – wave energy (J/m^2), c – wave celerity (m/s) and $H_{rms} = H_s/\sqrt{2}$ – significant wave height (m). Calculated Stokes drift velocity is then taken with a minus sign (in the direction opposite to the wave propagation direction), divided into x and y components and added to the provided input currents. However, in case of the Ameland tidal inlet the coastline is interrupted, so the return current will not be present. Confirmation of that was also seen from the measured currents during KG2 campaign as the cross-shore flow during storms was directed towards the coast over the entire water column (see Figure 39 in Section 4.3 and Appendix B). For that reason the option for computing additional return current in TSAND was disabled for the analysis.

However, the onshore directed mass flux due to Stokes drift will still be present, which can result in additional onshore sediment transport. Because of that, the same expressions were used to compute the depth-average

Stokes drift velocity in the direction of wave propagation, which was then added to the input currents from the DCSM-FM model. Because Stokes drift contributes mainly to the suspended sediment transport the total mass transport velocity U_m, which can be defined as a sum of Lagrangian Stokes drift velocity U_s and Eulerian mean velocity U_m, was used to compute suspended load transport, while for calculating bedload transport only Eulerian velocity was used. Depth-average Stokes drift velocities, calculated using equation (22), are shown in Figure 70 for the locations of the frames on the lower shoreface of the Ameland tidal and it can be seen that they can reach 0.05 – 0.07 m/s in longshore direction to the east and 0.07 – 0.09 m/s in the onshore direction. In order to get better representation of the Stokes drift, instead of using depth-average value a theoretical Stokes drift profile can be used assuming linear wave theory, which is defined by the following equation:

$$U_s(z) = \frac{1}{8}\omega k H_s^2 \frac{\cosh(2kz)}{\sinh^2(kh)} \tag{25}$$

where $k = 2\pi/L$ – wave number, $\omega = 2\pi/T$ – angular frequency, z – distance above the bed. Computed velocities did not include the additional mass flux in the wave breaking roller, which can also be added, which can be estimated by following expressions (Svendsen, 1984; Boers, 2005):

$$M_r = 2E_r/c \tag{26}$$

$$E_w = \frac{1}{2}\rho c \frac{H_{max}^2}{T_p} Q_b \tag{27}$$

where E_r – roller energy and Q_b – fraction of breaking waves. This, however, is not expected to have a significant contribution compared to the total mass flux due to Stokes drift, which occurs over the entire water column, and was not taken into account.

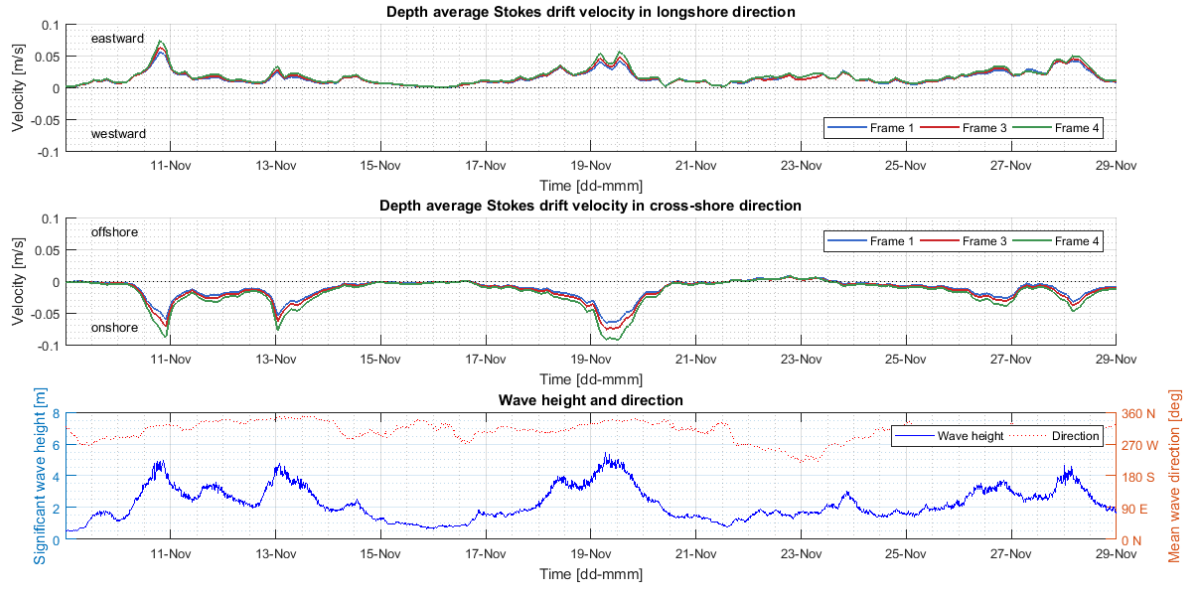

Figure 70 Additional depth-average Stokes drift velocity in longshore and cross-shore direction at the KG2 frames locations

Because the Lagrangian Stokes drift (following water particles) cannot be measured in an Eulerian way (measurements at a fixed point), calculated velocities cannot be validated against the measured data from the KG2 campaign and, because of that, sediment transport due to Stokes drift can only be analysed as potential additional contribution to the total sediment transport. The values of the total sediment transport in longshore and cross-shore direction calculated over the period of the KG2 field campaign from the measured and the 0.5 nm model currents without changes and with additional Stokes drift velocity profile are presented in Figure 71. From this figure it can be seen that adding the Stokes drift to the currents leads to increased eastward total

sediment transport in the longshore direction and an onshore sediment transport in the cross-shore direction. The contribution of the Stokes drift to the total transport increases towards the shallow water. However, similarly to what was observed for the Longuet-Higgins streaming, it can be seen that contribution of the Stokes drift without the wave-driven currents is smaller than for the measured currents. At water depth of 20 m (frame F1) the net transport due to Stokes drift is comparable, while at 16 (F3) and 11 m water depths (F4) measured currents show 2 to 4 times higher transport rates than the modelled currents. Besides that, additional transport due to Stokes drift can be lower due to the fact that the sediment particles might not follow the same paths as the water particles as they can also settle, but at least this method gives certain estimation of the maximum contribution.

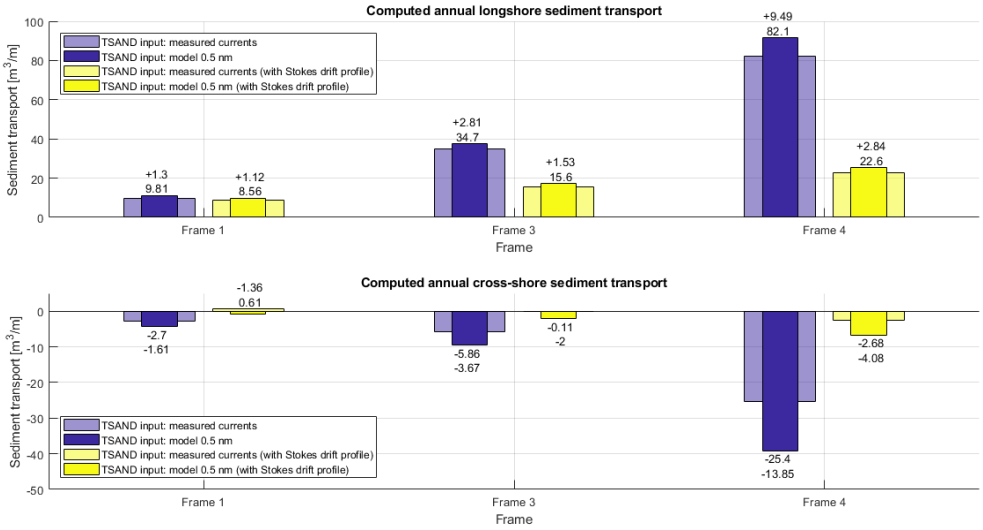

Figure 71 Integrated total longshore and cross-shore sediment transport, computed at the KG2 frames locations for a period from 9-29 November 2017 from measured currents, modelled currents from 0.5 nm and same modelled currents with additional depth-average Stokes drift velocity

The effect of Stokes drift on net annual sediment transport calculated from the DCSM model currents is presented in Figure 72. From this figure we can see that for the longshore transport additional potential contribution of the Stokes drift is about 15% for the stormiest year 2017 and around 5-10% for a year with average wave conditions. In absolute values it the additional yearly contribution due to Stokes drift to the longshore transport changes from 2.1-9.4 m^3/m at location of frame F1 to 2.3-13 m^3/m at F3 and 3.4-25 m^3/m at F4. For the cross-shore transport we can see that with the effect of Stokes drift net annual sediment transport also becomes more onshore at all the locations and change in sediment transport is within 1.8-13 m^3/m for the frame F1, 3-19 m^3/m for F3 and 6.3-41 m^3/m for F4. It can be seen that the yearly variation of the Stokes drift contribution in both longshore and cross-shore directions is relatively large depending on the wave conditions. For the year 2017, which is characterised with some very severe storms, its potential role is much larger as the net annual transport rates increase by 13, 19 and 41 m^3/m at frames F1, F3 and F4 respectively, while the average change in cross-shore transport for the other four years is 3.4, 5.3 and 11 m^3/m. As a result, even though wave-driven currents are not included in the DCSM model and because of that the Stokes drift contribution is underestimated, it can be concluded that it can play an important role on the lower shoreface of the Ameland tidal inlet, especially for stormy years and for the cross-shore transport, as its effect in this direction can significantly exceed the absolute values of the net yearly sediment transport calculated using the DCSM currents. For considered period Stokes drift results in average additional net yearly transport at 20 m water depth of up to 5 m^3/m in both eastward longshore and onshore direction. To properly assess the Stokes drift role at shallower water wave-driven currents need to be taken into account.

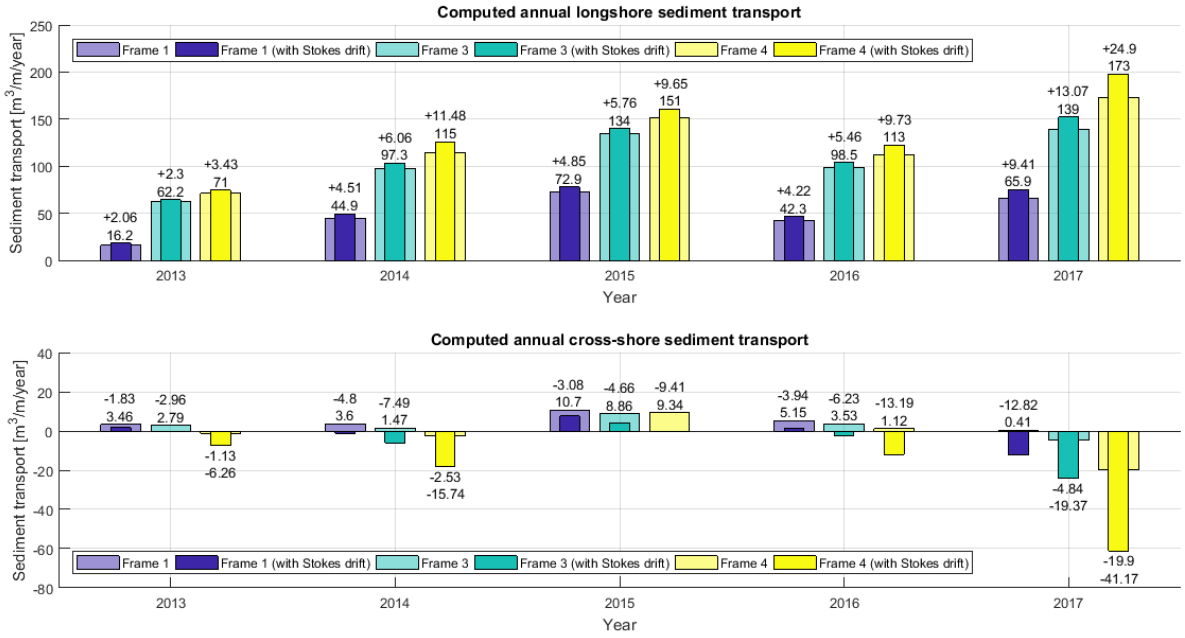

Figure 72 Net annual longshore and cross-shore yearly sediment transport computed at the KG2 frames locations for the period between 2013 and 2017 using the 0.5 nm model currents with additional Stokes drift profile (numbers above the bars show reference transport rates and change due to adding Stokes drift profile)

6.3 WAVE VELOCITY ASYMMETRY

In order to assess the effect of wave asymmetry on the sediment transport, the total sediment transport rates were calculated with and without additional contribution to the suspended load transport, which was computed using equation (10) presented in the Section 3.3.1. In the Figure 73 the effect of the wave asymmetry on the total longshore and cross-shore sediment transport is presented for the period of the KG2 field campaign for measured and modelled currents. From this figure it can be seen that for that wave asymmetry plays minor role in the sediment transport. Longshore transport slightly decreases when the wave asymmetry is not taken into account. The decrease is slightly higher for the measured currents, 0.1-0.7 m^3/m compared to the 0.1-0.2 m^3/m for the modelled currents. In the cross-shore direction the transport becomes slightly more offshore, changing by 0.1-1 m^3/m for the measured currents and 0.1-0.3 m^3/m for the modelled. The larger effect of wave asymmetry for the measured currents, similarly to what was observed for the effect of Stokes drift, is related to higher current velocities and suspended sediment concentrations during storm events compared to the DCSM currents, which results in slightly higher suspended sediment transport driven by wave asymmetry than for the modelled currents.

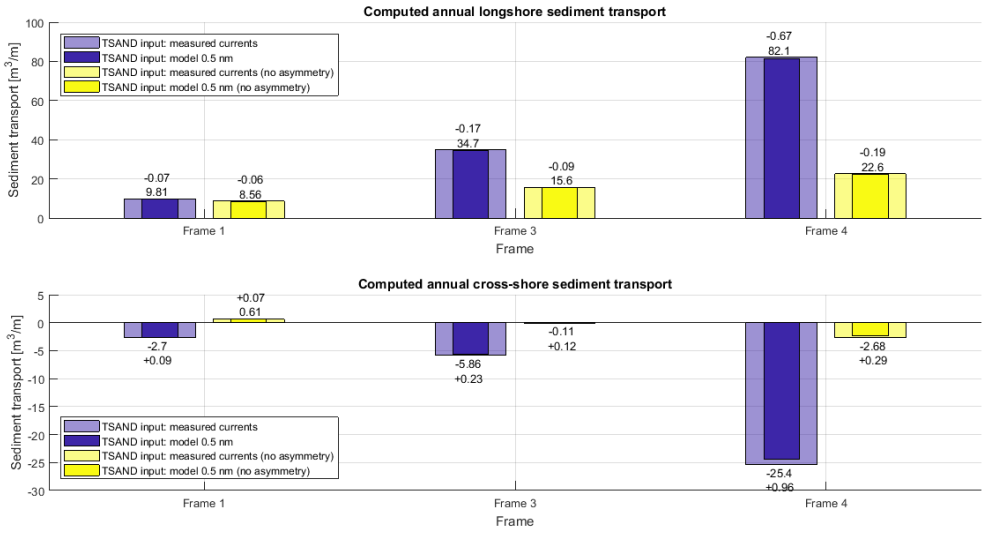

Figure 73 Integrated total longshore and cross-shore sediment transport with and without sediment transport contribution due to wave asymmetry computed from measured and modelled currents at the KG2 frames locations for a period from 9-29 November 2017

In the Figure 74 a comparison between the net annual longshore and cross-shore transport rates calculated from the modelled currents with and without additional transport due to wave asymmetry is presented for the years 2013 to 2017. From this figure it can be seen that on a yearly time scale the role of wave asymmetry is also very small. In the longshore direction variation of the yearly wave asymmetry contributions to the net eastward transport are 0.1-0.5 m^3/m for location of the frame F1, 0.1-0.7 m^3/m for F3 and 0.3-1.5 m^3/m for F4. In the cross-shore direction yearly transport due to wave asymmetry is also offshore and varies between 0.1-0.7 m^3/m at frame F1, 0.1-1.1 m^3/m at F3 and 0.3-2.4 m^3/m at F4. Similarly to the Longuet-Higgins streaming and Stokes drift, the largest change is observed for the year 2017, which was characterised with the most severe storm events. As it was seen from the Figure 73, the contribution of the wave asymmetry for the modelled currents underestimates the wave asymmetry transport for the measured currents by a factor 2 to 3 at frames F3 and F4. However, it can still be concluded that at 20 m water depth wave asymmetry almost does not affect the net sediment transport, which is also in line with the study of Van Rijn (1997). At shallower water the effect of wave asymmetry increases, but, even though its contribution to the net transport is underestimated, it can still be concluded that its effect is relatively small.

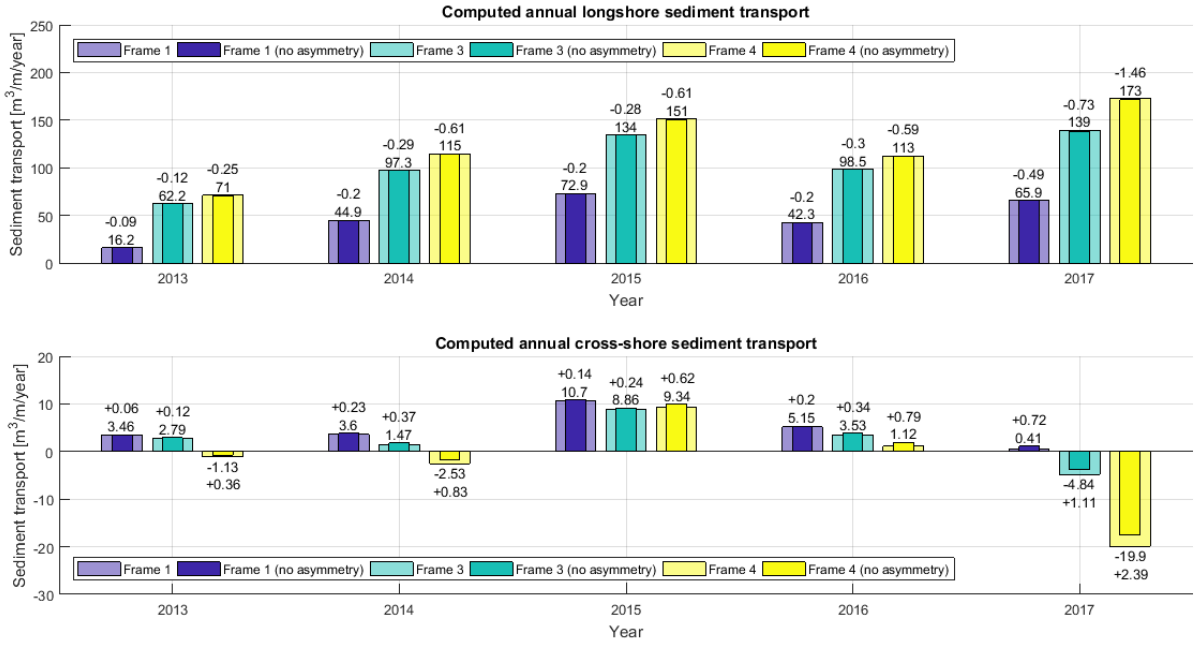

Figure 74 Net annual longshore and cross-shore sediment transport with and without sediment transport contribution due to wave asymmetry computed from measured and modelled currents at the KG2 frames locations for a period from 9-29 November 2017

6.4 WIND-DRIVEN CURRENTS

In order to assess the contribution of wind-driven currents to the predicted sediment transport rates, a 0.5 nm DCSM model run was performed for the year of 2017 without including the effect of wind. In the Figure 75 and Figure 76 a comparison between the measurements, model currents with wind and model currents without wind is presented for the longshore and cross-shore direction respectively. From these figures it can be seen that when both wave-driven and wind-driven currents are not taken into account, only tidal currents remain and the residual currents do not change in time, increasing towards shallow water from zero to about 0.05 m/s to the east for the longshore direction and giving a small offshore-directed current in the cross-shore direction.

In the Figure 77 comparison between the transport rates, calculated using modelled currents from the basic 0.5 nm and from the same model without wind for the period of the field campaign, is presented. From this figure it can be seen that wind-driven currents also play a relatively large role in the sediment transport on the lower shoreface. As it was shown in the Chapter 4, over the period of the KG2 campaign western wind was observed most frequently and the longshore sediment transport rates with the effect of wind excluded are reduced over the entire lower shoreface. The effect of wind is particularly important at the deepest frame F1, where the effects of wave-driven currents in the longshore direction are almost absent as the DCSM model with win shows good agreement with the data, which means that most of the longshore transport at this location occurs as a result of wind action. In the cross-shore direction we can see that sediment transport becomes slightly more onshore when wind is not taken into account. This probably is related to the strong south-southwestern winds that were also observed during field campaign, which to a certain degree reduces flow of water and sediment towards the tidal inlet. Also, it can be seen that the effect of wind on total transport in both longshore and cross-shore direction slightly increases towards shallower water. From the Figure 78, on which difference between sediment transport calculated with and without wind-driven currents for the entire year of 2017 is presented, we can see the similar patterns as for the period of the field campaign.

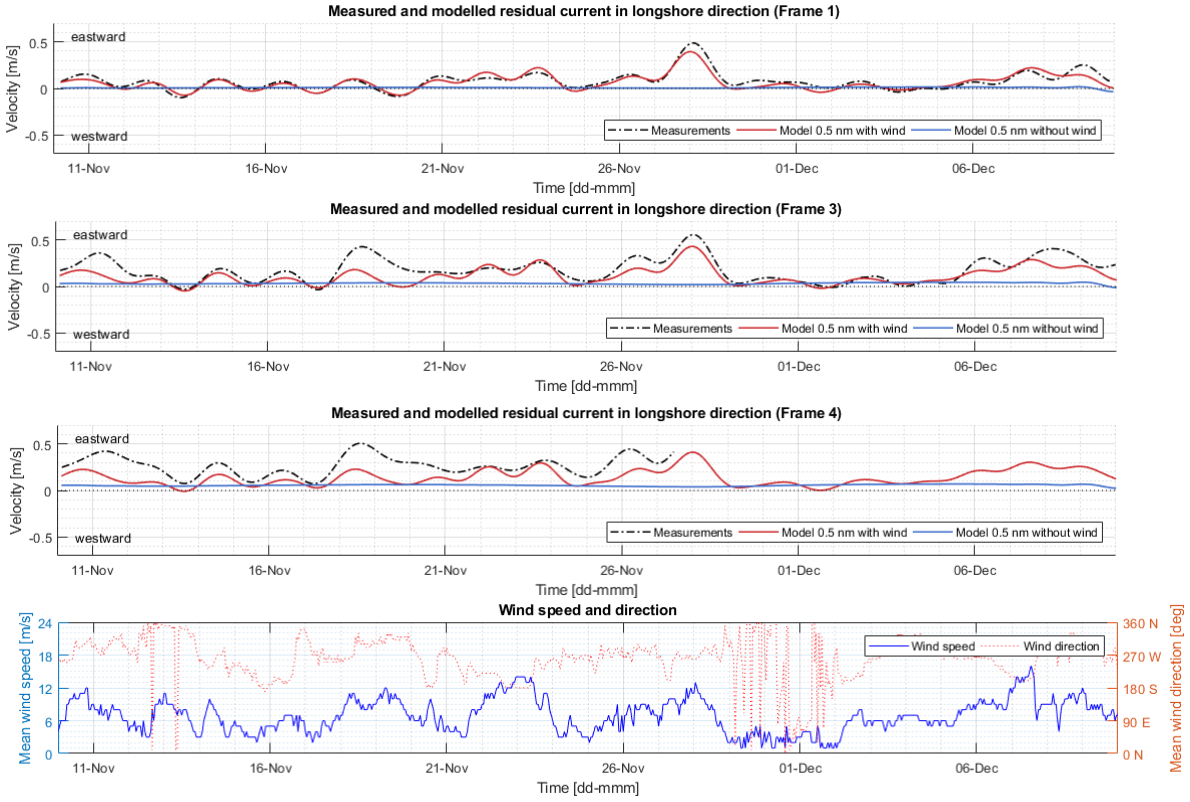

Figure 75 Measured and modelled (DCSM 0.5 nm with and without wind) depth-average longshore residual currents at the lower shoreface frames

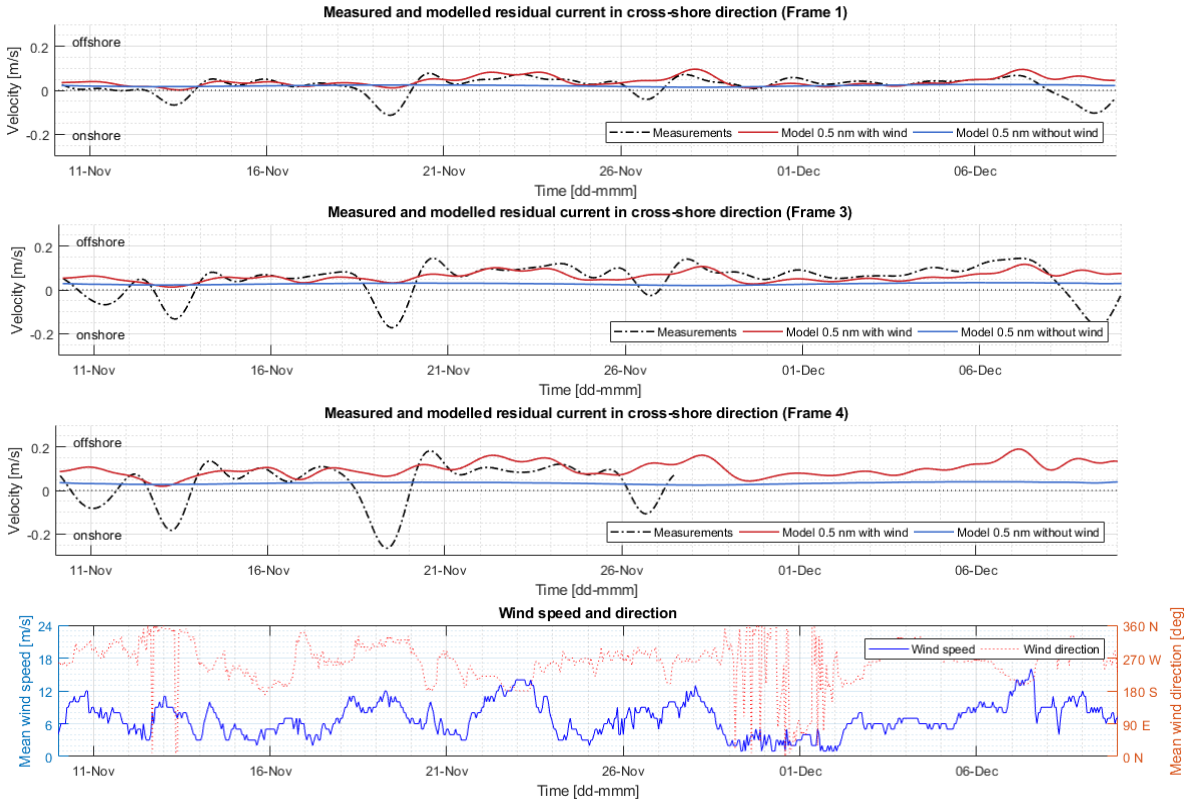

Figure 76 Measured and modelled (DCSM 0.5 nm with and without wind) depth-average cross-shore residual currents the lower shoreface frames

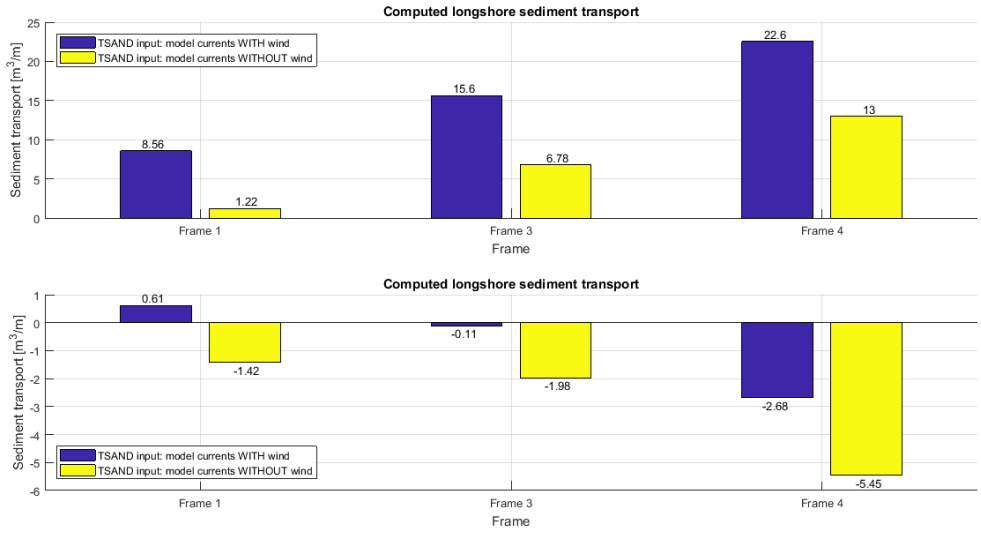

Figure 77 Integrated total longshore and cross-shore yearly sediment transport, computed at the KG2 frames locations for the period of the field campaign from the regular 0.5 nm model and from 0.5 nm model without wind

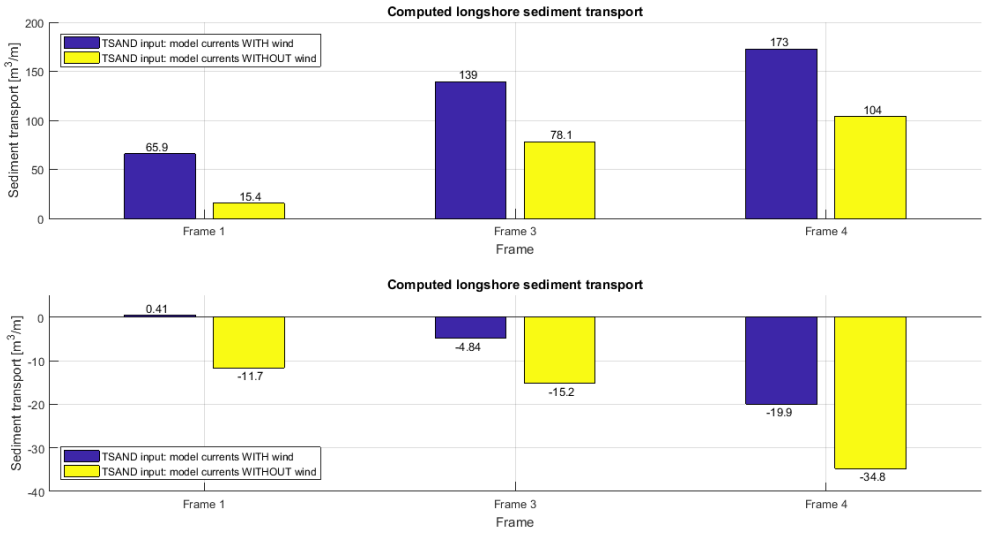

Figure 78 Net annual longshore and cross-shore yearly sediment transport, computed at the KG2 frames locations for the year of 2017 from the regular 0.5 nm model and from 0.5 nm model without wind

6.5 DISCUSSION AND CONCLUSIONS

Sediment transport modelling results can be summarized in the following points:

- Comparison of the transport rates calculated using the measured and the modelled currents with and without different sediment transport mechanisms, particularly Longuet-Higgins streaming, Stokes drift and wave velocity asymmetry, has shown that for shallower parts of the lower shoreface at frames F3 (16 m water depth) and F4 (11 m water depth) the absence of wave-driven currents in the DCSM model results in underestimation of the mechanisms contributions for the net annual sediment transport. For the water depth of 20 m the results for the measured and the modelled currents were comparable and it was possible to quantitatively estimate contribution of different mechanisms to the longshore and cross-

shore net annual transport. For more shallow water their contribution could be assessed only in a qualitative way and in order to the proper analysis the wave-driven currents should be taken into account.

- Excluding the effects of wave-induced Longuet-Higgins streaming and wave velocity asymmetry both results in decreased eastward longshore and onshore net sediment transport. At 20 m water depth their contribution to the net annual transport is almost zero, which is in line with the results of Van Rijn (1997). At shallower water their role increases, but compared to other mechanisms it is still relatively small.
- Stokes drift can lead to a certain amount of additional eastward and onshore sediment transport and its role is particularly important for the cross-shore sediment transport increasing the net transport for the field campaign nearly 1.5 times at all three locations. At 20 m water depth its contribution to the net yearly transport was on average 5 m^3/m in both cross-shore and longshore direction and it increases towards the shallow water. Variation of the Stokes drift contribution from year to year is also very high significantly increasing for the years characterised with storm events of low frequency of occurrence.
- Comparison of the transport rates calculated using currents from the DCSM model runs with and without wind for the year of 2017 has shown that wind-driven currents contribute to the net eastward sediment transport in longshore direction and reduce the onshore transport. This is in line with the observed wind conditions which showed most frequently observed wind during stormy periods coming from the west and the strongest winds coming from the south and southwest. Comparing the transport rates for the field campaign from measured and modelled currents with and without wind it can be concluded that the relative role of wind-driven currents is the highest at deeper water and decreases towards the shallower water, where the mismatch in the transport rates due to wave-driven currents becomes more important.

7. DISCUSSION, CONCLUSIONS AND RECOMMENDATIONS

The objective of this master thesis was twofold, first, to obtain better understanding about hydrodynamics and sediment transport processes on the lower shoreface of the Ameland tidal inlet, in particular about the effect of waves on currents and about physical mechanisms that determine the net annual sediment transport, and, second, to validate the new "offline" sediment transport modelling approach for the lower shoreface of the Ameland tidal inlet. In this chapter, first, the points of discussion will be presented. This will be followed by the conclusions of the study, which will be presented in a form of answers to research questions that were formulated in the introduction to this report. After that, some recommendations will be given regarding the further application of the offline sediment transport modelling approach and the DCSM-FM model for more large scale analysis of the sediment transport on the Dutch lower shoreface based on the conclusions that were made for the Ameland tidal inlet.

7.1 DISCUSSION

The main point for discussion in this master thesis project comes from interpretation of the mismatch between the modelled and the measured currents during storm events. From the measured residual currents an increased longshore eastward current was observed during the storm events at 11 and 16 m water depth (Figure 45). In the cross-shore direction an increased onshore current was observed during the storms and an offshore current – after storms for all three locations (Figure 46). Combining these observations made from the data with the results of the DCSM model and the Delft3D model without waves, in both of which the observed patterns are not captured (Figure 51), suggests that the mismatch results not from the coarse DCSM model resolution but from the absence of waves and wave-driven currents in the model. However, it is not entirely clear what exactly drives these currents. Assuming that the wave breaking is the only mechanism lacking in the model that may cause the mismatch between the measured and the modelled currents in the longshore direction, the fact that the DCSM model shows almost perfect agreement with the data for the longshore currents at 20 m water depth suggests that wave breaking does not occur at this location. Because of that, a conclusion can be made that the onshore current during storms is not caused by the onshore flow into the tidal inlet that develops due wave breaking and balance between radiation stress gradient and bed shear stress, similarly to how the longshore current is generated. This means that this onshore residual current results from some other mechanism, but still related to the effect of waves, which is the only component missing in the DCSM model, which could be the effect of the tidal inlet "pulling" the water in due to water level setup on the barrier islands and ebb-tidal delta, which extends further away from the inlet during storms. This effect can be investigated using a spatial picture of the residual currents and surge water levels derived from a model that includes the effects of waves.

This leads to another question that arises when looking at the results Delft3D model with waves compared to the measurements and to the results of the models without waves. From this comparison it was observed that the Delft3D model with waves reproduces the patterns of the measured residual currents but only to some extent, as the mismatch with the data is still relatively high (Figure 51). One of the reasons that might cause this deviation might be the incorrectly reproduced large scale atmospheric forcing. This hypothesis results from the observation on how different models reproduced the event that was observed in the data around 28 November 2017. Regular storm events that lead to the current patterns that were described above are characterized by waves between 4 and 5 m and wind coming from approximately northwest. During event on November 28, significantly increased eastward longshore residual current was observed simultaneously at all three lower shoreface frames, while in the cross-shore direction the onshore current was not present. The period prior to this event was characterized by a steady western wind for 5 to 6 days and significant wave heights of 3 to 4 m suggesting that the observed longshore current is mainly wind-driven. And for this event,

the DCSM model without the effect of waves showed better results than the Delft3D model without waves, while the worst results for this particular event were observed for the Delft3D model with waves. Because of that, a hypothesis can be made that the problem can be related either to mismatch in the atmospheric forcing within the model domain, or to some issues with the boundary conditions, which are derived from another model, both of which can lead to incorrectly reproduced wind-driven currents in the model and mismatch between the Delft3D model and the measurement during storms. In the DCSM model, on the other hand, these problems might not be present as it covers much larger area, over which large scale circulation due to the atmospheric forcing can develop, resulting in better performance of the model for the wind-driven currents. Another possible reason for the mismatch between the Delft3D model with waves and the measurements could be the way that the wave-driven currents are defined in Delft3D or the fact that the model is depth average. None of these three factors, however, were investigated in detail within this master thesis project as the Delft3D model was outside of the main scope of the study.

7.2 CONCLUSIONS

Research Question 1:

What do the new current measurements show in terms of hydrodynamics on the lower shoreface of the Ameland tidal inlet?

From the new measurements from the Ameland tidal inlet, which consist of current profiles at 20, 16 and 11 m water depth for a period from November 8 to December 11 2017, we can conclude that the currents on the lower shoreface are dominated by the tides but are also significantly affected by wind and waves during storms. The period of the field campaign can be characterized as very stormy, with several storm events with offshore significant wave height reaching 5 m, which also corresponds to strong northern and north-western wind. During these storm events an increased eastward longshore current was observed in the shallower part of the lower shoreface. In the cross-shore direction these storms led to an onshore current over the entire water column, which was observed at all three locations on the lower shoreface and increased towards the shallow water, while calm conditions are generally characterised by a very small offshore directed residual current. After the storm event, a slight increase in offshore current was observed, which, together with the onshore current, can be explained by the process of filling and emptying of the Wadden Sea during storms, which also can be seen from the water levels inside and outside of the Wadden Sea.

Research Question 2:

How valid is the offline sediment transport modelling approach for the lower shoreface of the Ameland tidal inlet?

Validation of the DCSM-FM model, which does not include waves and, as a result, wave-driven currents, has shown that for the area of the Ameland tidal inlet model performs well in reproducing the water level variation in the North Sea (uRMSE 0.09 m). For the Wadden Sea the performance is worse (uRMSE 0.18 m) and the surge water level in the Wadden Sea is typically underestimated during storm events, which suggests that in the model not enough water is flowing through the tidal inlet at these conditions. Besides that, because the vertical reference in the model is not clearly defined and because of the way it was calibrated, water levels in the model are also characterized with a bias of 0.35 m leading to an overestimation of the discharges through the tidal inlet during both flood and ebb. Validation of the model by the current measurements from the KG2 field campaign has shown that tidal currents are reproduced well by the model (correlation coefficient 0.99 for longshore and 0.5-0.9 for cross-shore currents and RMSE 0.06 m/s) and it demonstrates good agreement with the data during periods of calm conditions. For the total currents model showed better results for deeper

water. Correlation for the longshore currents was still high, with correlation coefficient value of 0.95-0.99, while RMSE increased to 0.09-0.19 m/s and bias was between 0.01-0.14 m/s. For the cross-shore currents correlation decreased to 0.3-0.65, while RMSE increase to 0.05-0.15 m/s. From the filtered currents it was seen that during storms the model does not capture the characteristic current patterns that were observed in the measurements. Eastward longshore current at the shallower part of the lower shoreface is significantly underestimated, while in cross-shore direction the model shows a steady small offshore directed current regardless of the wave conditions. Sensitivity of the results to the model bathymetry was small and comparing the DCSM model results to the results of the detailed Delft3D model of the Ameland tidal inlet suggested that the mismatch between the data and the DCSM model does not occur due to coarse resolution and inaccurate representation of bathymetry, but indeed by the lack of waves and wave-driven currents in the model.

Comparison of the sediment transport rates calculated using TSAND from the measured and the DCSM model currents for the period of the field campaign has shown that, in the longshore direction at the deepest frame F1, modelled currents give values very close to the ones predicted from the measured currents, but as it becomes shallower they tend to give lower transport rates than the measured currents and the difference is highest at the shallowest frame F4. In the cross-shore direction measured currents give onshore-directed total sediment transport at all the locations significantly increasing towards shallow water, while DCSM model currents give small offshore transport at deeper water and onshore transport – at shallower, but much smaller compared to the transport from the measured currents. The sediment transport occurs mainly during storm events and the main difference between the result from the measured and the modelled currents is observed during these events. Comparing the transport rates, calculated using TSAND with the modelled currents for the entire year of 2017, with the ones calculated using measured currents for the period of the KG2 field campaign it was possible to conclude that the mismatch in the currents is very important for the net annual sediment transport on the lower shoreface, especially in the cross-shore direction, as the values for the 20-day period with waves are nearly the same as for the full year. Because of that, it can be concluded that in its present state the offline sediment transport modelling approach cannot be used for the analysis of the net annual sediment transport for the Ameland tidal inlet. This is the case even for the water depth of 20 m, where the yearly cross-shore transport from modelled currents is around zero and about 3 m^3/m onshore for the field campaign. From a rough estimation of the yearly transport from the transport during field campaign is can be seen that this mismatch can be significant for the determining the required nourishment volume of the Coastal Foundation.

Research Question 3:

What is the magnitude and direction of the cross-shore and longshore net annual sediment transport on the lower shoreface of the Ameland tidal inlet and which physical mechanisms determine this?

Because the offline sediment transport modelling approach was concluded to be not applicable for the lower shoreface of the Ameland tidal inlet, this research question could not be fully answered. However, some assessment of the contributions of different sediment transport mechanisms still could be done. Comparison of the transport rates calculated using the measured and the modelled currents with and without different sediment transport mechanisms, particularly Longuet-Higgins streaming, Stokes drift and wave velocity asymmetry, has shown that for shallower parts of the lower shoreface at 16 and 11 m water depth the absence of wave-driven currents in the DCSM model also results in underestimation of the mechanisms contributions for the net annual sediment transport on the lower shoreface. For the water depth of 20 m the results for the measured and the modelled currents were comparable and it was possible to quantitatively estimate contribution of different mechanisms to the longshore and cross-shore net annual transport. For more shallow water their contribution could be assessed only in a qualitative way and in order to the proper analysis the wave-driven currents should be taken into account.

Excluding the effects of wave-induced Longuet-Higgins streaming and wave velocity asymmetry both results in decreased eastward longshore and onshore net sediment transport. At 20 m water depth their contribution to the net annual transport is almost zero, which is in line with the results of Van Rijn (1997). At shallower water their role increases, but compared to other mechanisms it is still relatively small. Stokes drift can lead to a certain amount of additional eastward and onshore sediment transport and its role is particularly important for the cross-shore sediment transport increasing the net transport during the field campaign nearly 1.5 times at all three locations. At 20 m water depth its contribution to the net yearly transport was on average 5 m^3/m in both cross-shore and longshore direction and it increases towards the shallow water. Variation of the Stokes drift contribution from year to year is also very high as it significantly increases for the years characterised with storm events of low frequency of occurrence. Wind-driven currents contribute to the net eastward sediment transport in longshore eastward direction and reduce the onshore transport. This is in line with the observed wind conditions which showed most frequently observed wind during stormy periods coming from the west and the strongest winds coming from the south and southwest. Comparing the transport rates for the field campaign from measured and modelled currents with and without wind it can be concluded that the relative role of wind-driven currents is the highest at deeper water and it decreases towards the shallower water, where the mismatch in the transport rates due to wave-driven currents becomes more important.

7.3 RECOMMENDATIONS

As a result of this master thesis project it was concluded that at the moment the offline approach with the currents from the DCSM model cannot be used for the analysis of the net annual sediment transport on the lower shoreface in case of an interrupted coastline. However, certain modifications to the currents, which were not tested within this master thesis project, potentially can be made in order to still make use of the DCSM model as there definitely are multiple arguments for it. Analysis of the currents on the lower shoreface of the Ameland tidal inlet has shown that wave-driven currents due to breaking play there a considerable role during storm events with significant wave height of 4 to 5 m driving longshore currents and, as a result, sediment transport. To account for that, it can be attempted to compute longshore current due to wave breaking using some analytical expression. This is necessary not only for the tidal inlet case, but also for other locations with the closed coast as the effect of the longshore current due to wave breaking there will probably be comparable. To compute the onshore current due to wave breaking there is no analytical expression available, potentially one can be derived similarly to the expression for the longshore current: from the balance between wave force and bed shear stress in the cross-shore direction (instead of the balance between wave force and water level setup, which is usually used for the closed cost). Any analytical expressions, however, contain a lot of assumptions and first should be validated using field data of the KG2 campaign.

Because this master thesis project focused only on an interrupted coastline situation, its conclusions cannot directly be translated to a location with closed coast. At other locations at the Dutch lower shoreface wave breaking will still result in longshore currents, while in the cross-shore direction wave-driven currents in case of a closed coast will be significantly different. Because of that, it is recommended to perform analysis, similar to the one that was done for Ameland, for the locations at Terschelling and Noordwijk in order to evaluate the importance of the wave-driven return current, which develops due to wave breaking on a closed coast, for the sediment transport on the lower shoreface using the KG2 data and DCSM model. If its contribution will be important, last version of the TSAND model contains an analytical expression to calculate this return current as a depth-average and uniformly distributed over the water column, but to get better representation of the undertow, an analytical undertow profile can be used instead (Van Rijn, 2013), which can also be validated by the field data. Only after that a conclusion about application of the DCSM model along with TSAND for the analysis of the net annual sediment transport on a closed coast can be made.

REFERENCES

Boers, M. (2005) Surf zone turbulence. Ph.D. thesis, Delft University of Technology, The Netherlands.

Burau J.R, Simpson M.R., Cheng R.T. (1993) Tidal and residual currents measured by an acoustic Doppler current profiler at the west end of Carquinez Strait, San Francisco Bay, California, March to November 1988 (No. 92-4064). Sacramento, California: U.S. Army Corps of Engineers

Davies A.G., Villaret C. (1999) Eulerian drift induced by progressive waves above rippled and very rough beds. *Journal of Geophysical Research*, **104** (C1), pp. 1465-1488

De Fockert A., Luijendijk A. (2011) Wave look-up table: Building with Nature. Memo 1002337-002-ZKS-0001. Deltares, Delft, the Netherlands

Dissanayake P.K. (2011) Modelling morphological response of large tidal inlet systems to sea level rise. PhD thesis, UNESCO-IHE, Delft, The Netherlands, 168 pp.

Duran-Matute M., Gerkema T. (2015) Calculating residual flows through a multiple-inlet system: the conundrum of the tidal period. *Ocean Dynamics*, **65**, pp. 1461-1475

Eisma D. (1968) Composition, origin and distribution of Dutch coastal sands between Hoek van Holland and the island of Vlieland. *Netherlands Journal of Sea Research*, **4** (2), pp. 123-267

Forbes A.M.G. (1988) Fourier transform filtering: A cautionary note. *Journal of Geophysical Research*, **93** (C6), pp. 6958-6962

Godin G. (1972) The Analysis of Tides. University of Toronto Press, 264 pp.

Goring D.G., Nikora V.I. (2002) Despiking acoustic Doppler velocimeters data. *Journal of Hydraulic Engineering*, **128** (1), pp. 117-126

Grasmeijer B.T. (2018) Method for calculating sediment transport on the Dutch lower shoreface. Memo 1220339-005-ZKS-0002. Deltares, Delft, the Netherlands

Grasmeijer B.T., Ruessink B.G (2003) Modelling of waves and currents in the nearshore parametric vs. probabilistic approach. *Coastal Engineering*, **49**, pp. 185-207

Mol J.W. (2018) KG2 DVA metadata frame 1, 3, 4. RWS CIV

Mori N., Suzuki T., Kakuno S. (2007) Noise of acoustic Doppler velocimeter data in bubbly flow. *Journal of Engineering Mechanics*, **133** (1), pp. 122-125

Munk W.H. (1950) Origin and generation of waves. 1st International Conference on Coastal Engineering Proceedings, Long Beach, California, ASCE, pp. 1-4

Nederhoff C.M., Schrijvershof R., Tonnon P.K., Van der Werf J.J. (2018).The Coastal Genesis II Terschelling - Ameland inlet (CGII-TA) model, Model setup, calibration and validation of a hydrodynamic-wave model. Draft report 1220339-008, Deltares, The Netherlands.

Niedoroda A.W., Swift D.J.P, Hopkins T.S. (1985) The Shoreface. Coastal Sedimentary Environments. Davis R.A. {ed.}. New York, NY. Springer – Verlag, (Second Revised, Expanded Edition) 8, pp. 533-624

Pawlowicz R., Beardsley B., Lentz S. (2002) Classical tidal harmonic analysis including error estimates in MATLAB using T_TIDE. *Computers & Geosciences*, **28**, pp. 929-937

Ribberink J.S. (1997) Bed-load transport for steady flows and unsteady oscillatory flows. Delft Hydraulics, Delft, The Netherlands

Shirahata K. Yoshimoto S., Tsuchihara T., Ishida S. (2016) Digital filters to eliminate or separate tidal componentsin groundwater observation time-series data. *Japan Agricultural Research Quarterly*, **50** (3), pp. 241-252

Svendsen, I.A. (1984) Mass flux and undertow in a surf zone. *Coastal Engineering*, **8**, pp. 347-365.

Taal M., Mulder J., Cleveringa J., Dunsbergen D. (2006) 15 years of coastal management in the Netherlands; Policy, implementation and knowledge framework. The Hague, Rijkswaterstaat, National Institute for Coastal and Marine Management/RIKZ.

Thompson R.E., Emery W.J. (2014) Data analysis methods in physical oceanography (3rd ed.). Elsevier

Thompson R.O.R.Y. (1983) Low-pass filters to suppress inertial and tidal frequencies. *Journal of Physical Oceanography*, **13**, pp. 1077-1083

Van der Burgh L. (2018) Risk and coastal zone policy: example from the Netherlands. Available from http://www.coastalwiki.org/wiki/Risk_and_coastal_zone_policy:_example_from_the_Netherlands [accessed on 12-06-2018]

Van der Werf J., Grasmeijer B., Hendriks E., van der Spek A., Vermaas T. (2017) Literature study Dutch lower shoreface. Report 1220339-004-ZKS-0001. Deltares, Delft, the Netherlands

Van Rijn, L.C. (1993) Principles of sediment transport in rivers, estuaries and coastal seas. Aqua Publications, Amsterdam, The Netherlands

Van Rijn, L.C. (1997) Sediment transport and budget of the central coastal zone of Holland. *Coastal Engineering*, **32**, pp. 61-90

Van Rijn L.C. (2007a) Unified view of sediment transport by currents and waves. I: Initiation of motion, bed roughness and bed-load transport. *Journal of Hydraulic Engineering*, **133** (6), pp. 649-667

Van Rijn L.C. (2007b) Unified view of sediment transport by currents and waves. II: Suspended transport. *Journal of Hydraulic Engineering*, **133** (6), pp. 668-689

Van Rijn, L.C. (2011) Principles of fluid flowand surface waves in rivers, estuaries and coastal seas. Aqua Publications, Amsterdam, the Netherlands

Van Rijn L.C., Ribberink J.C., Reniers A., Zitman T. (1994) Yearly-averaged sand transport at the-20 and -8 m NAP depth contours of Jarkus profiles 14, 40, 76 and 103. Report H1887. Delft Hydraulics, Delft, The Netherlands

Walters R.A., Heston C. (1982) Removing tidal-period variations from time-series data using low-pass digital filters. *Journal of Physical Oceanography*, **12**, pp. 112-115

Zijl F., Veenstra J. (2018) Setup and validation of 3D DCSM-FM. Memo 1220339-005-ZKS-0003. Deltares, Delft, The Netherlands

Zijl F., Verlaan M., Gerritsen H. (2013) Improved water-level forecasting for the Northwest European Shelf and North Sea through direct modelling of tide, surge and non-linear interaction. *Ocean Dynamics*, **63**(7), pp. 823-847

APPENDICES

APPENDIX A. MEASURED AND MODELLED DEPTH-AVERAGE VELOCITY TIME-SERIES

In this appendix the full time series comparison of the measured and DCSM model depth-average longshore and cross-shore currents are presented for the frame F1 (Figure A.1), F3 (Figure A.2) and F4 (Figure A.2), from which the mismatch between the modelled and measured total currents can be seen during the storm events at all three locations.

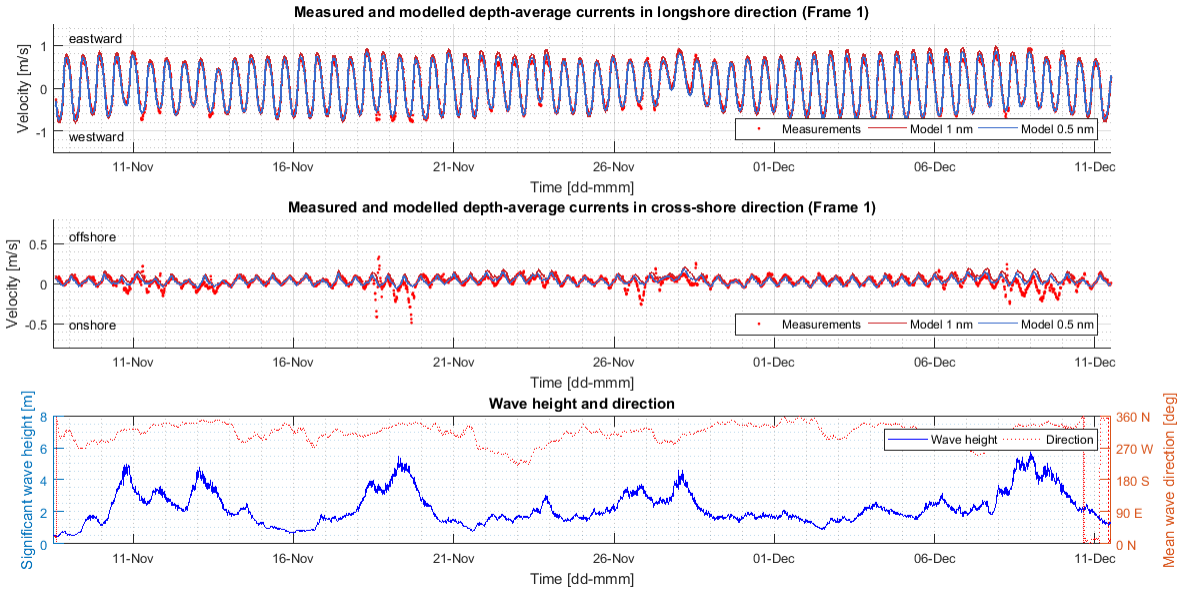

Figure A.1 Measured and modelled (DCSM 1 and 0.5 nm) depth-average cross-shore and longshore current velocity time-series at frame F1 (water depth 20 m) with wave conditions

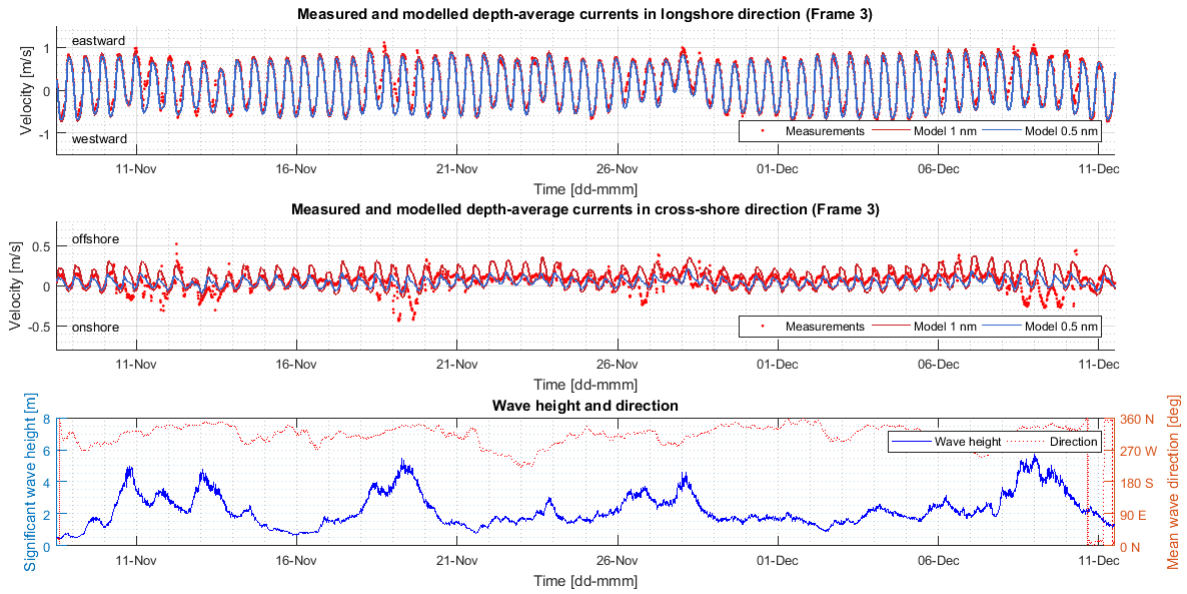

Figure A.2 Measured and modelled (DCSM 1 and 0.5 nm) depth-average cross-shore and longshore current velocity time-series at frame F3 (water depth 16 m) with wave conditions

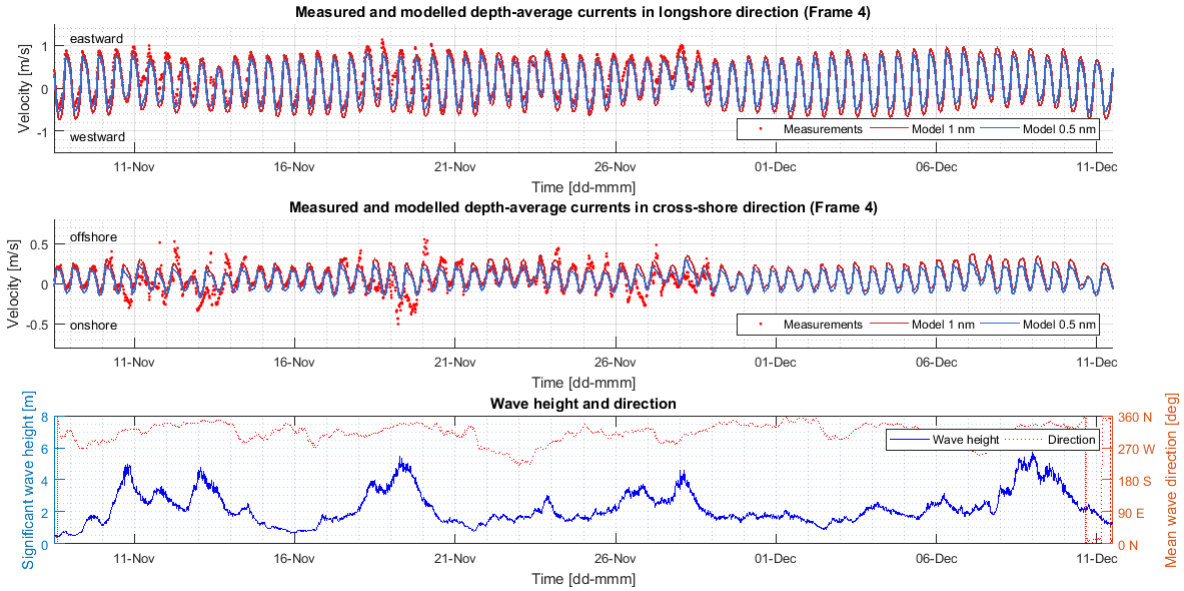

Figure A.3 Measured and modelled (DCSM 1 and 0.5 nm) depth-average cross-shore and longshore current velocity time-series at frame F4 (water depth 11 m) with wave conditions

APPENDIX B. MEASURED AND MODELLED INSTANT VELOCITY PROFILES DURING CALM AND STORM CONDITIONS

In this appendix comparison of the instant measured and modelled velocity profiles is presented for longshore and cross-shore currents at all three lower shoreface frames at different stages of a tidal cycle together with the time series of the depth-average velocities and observed wind and wave conditions. In the Appendix B.1 the figures are given for the calm conditions during peak ebb (Figure A.4), flood (Figure A.5), peak flood (Figure A.6) and ebb (Figure A.7). In the Appendix B.2 the data is given for storm conditions during peak flood (Figure A.8), ebb (Figure A.9), peak ebb (Figure A.10) and flood (Figure A.11).

B.1 CALM CONDITIONS

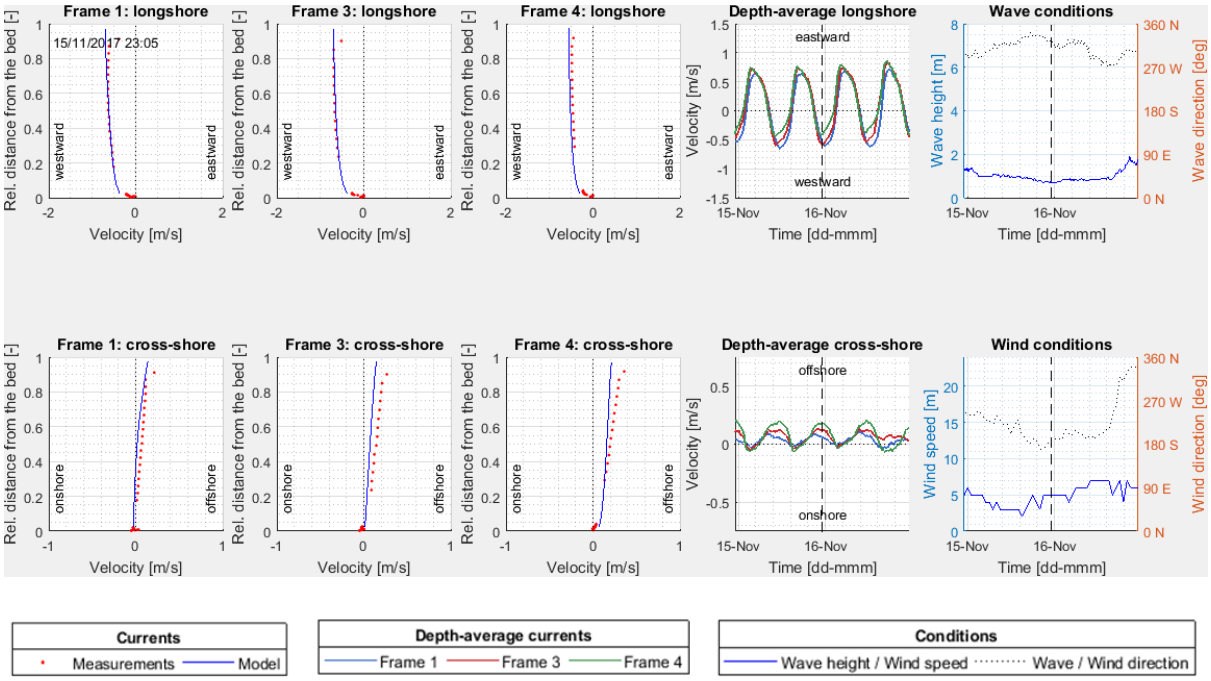

Figure A.4 Measured and modelled (DCSM 0.5 nm) velocity profiles at lower shoreface frames with measured depth-average velocities and observed wind and wave conditions on 15 November 2017 23:05 (calm conditions, peak ebb)

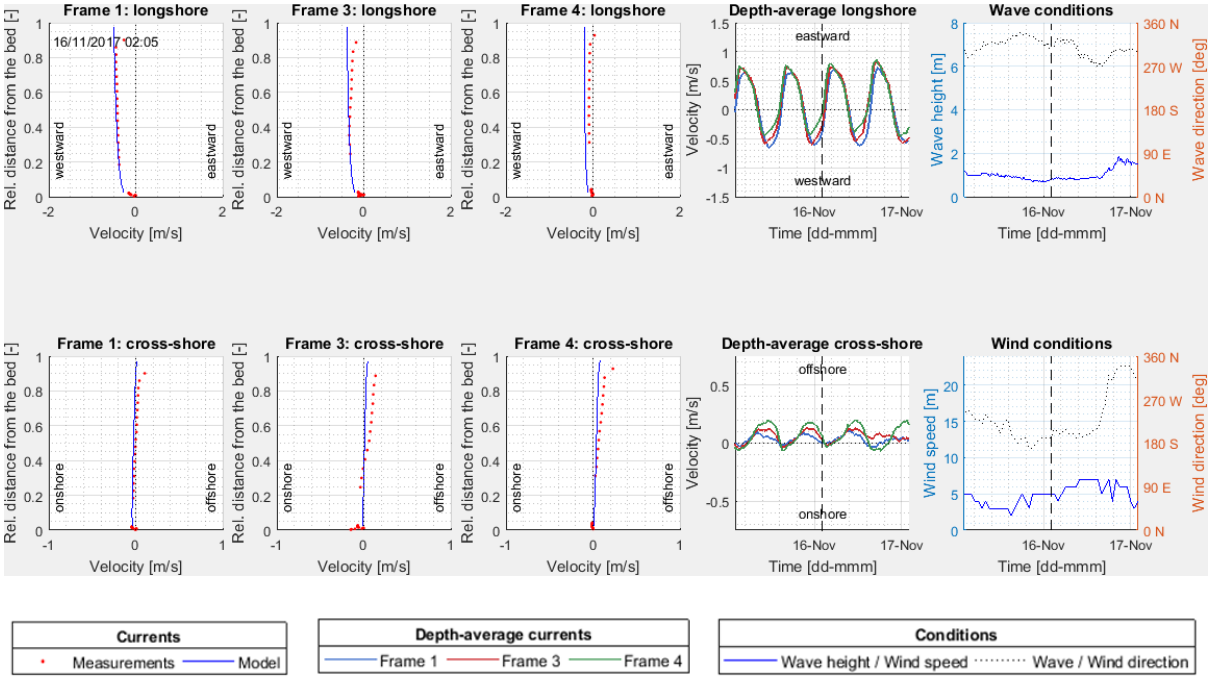

Figure A.5 Measured and modelled (DCSM 0.5 nm) velocity profiles at lower shoreface frames with measured depth-average velocities and observed wind and wave conditions on 16 November 2017 2:05 (calm conditions, flood)

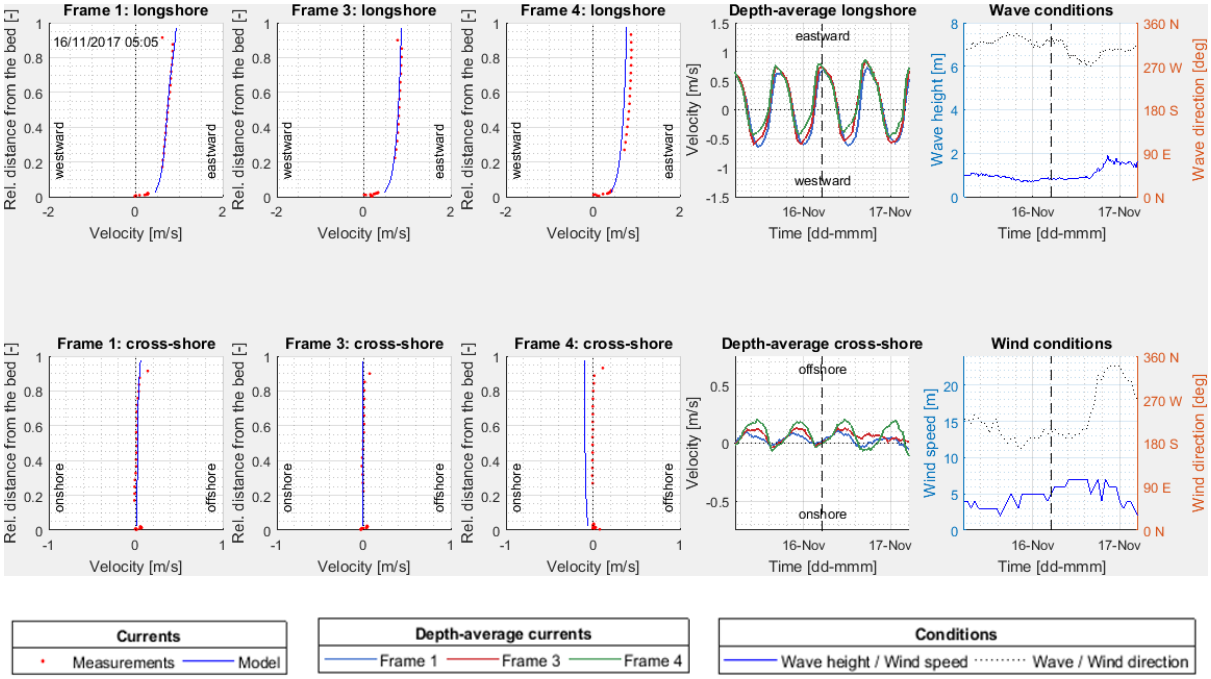

Figure A.6 Measured and modelled (DCSM 0.5 nm) velocity profiles at lower shoreface frames with measured depth-average velocities and observed wind and wave conditions on 16 November 2017 5:05 (calm conditions, peak flood)

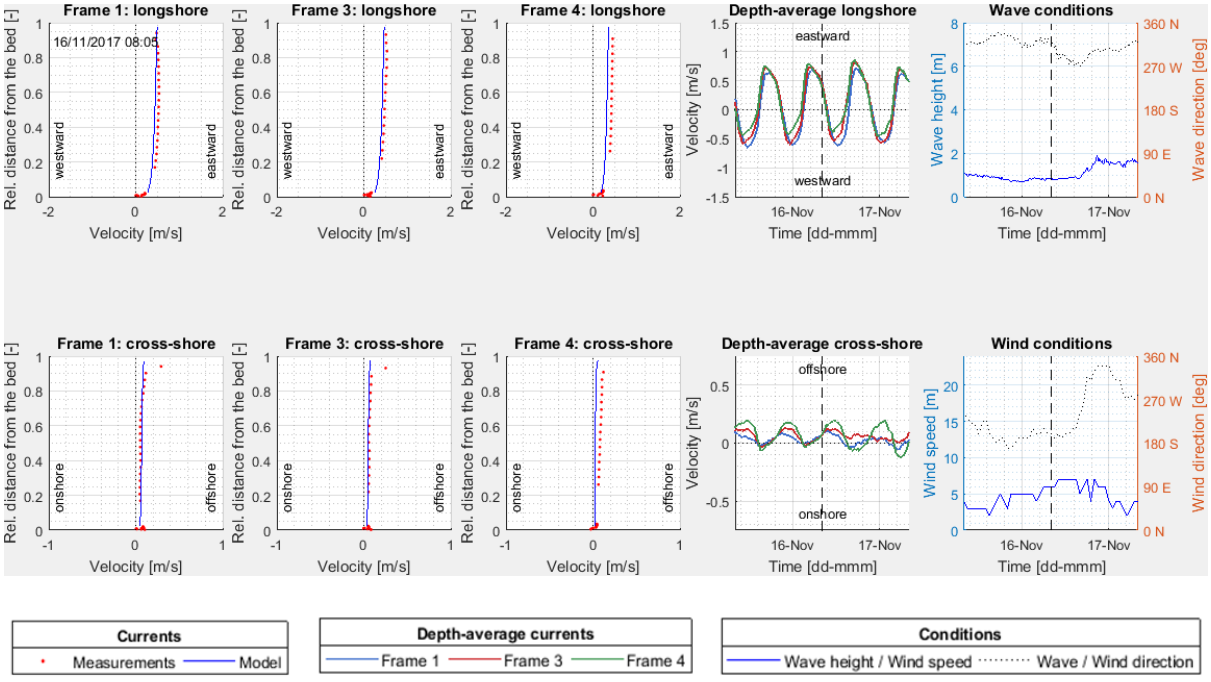

Figure A.7 Measured and modelled (DCSM 0.5 nm) velocity profiles at lower shoreface frames with measured depth-average velocities and observed wind and wave conditions on 16 November 2017 8:05 (calm conditions, ebb)

B.2 STORM CONDITIONS

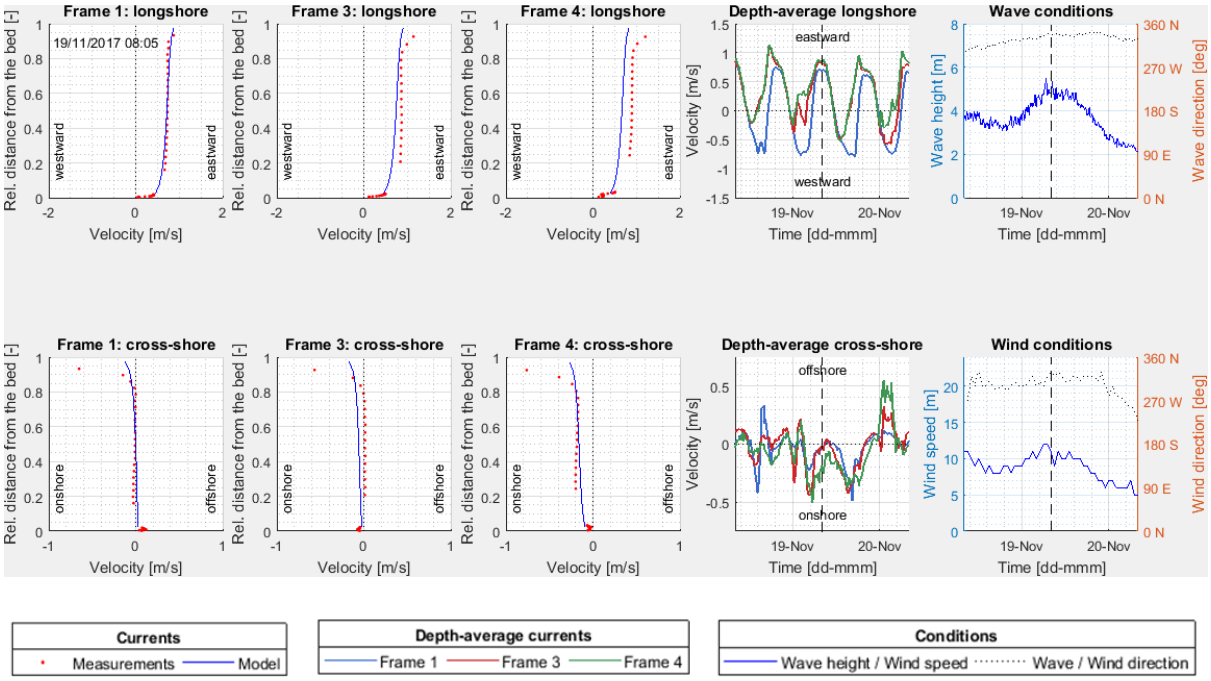

Figure A.8 Measured and modelled (DCSM 0.5 nm) velocity profiles at lower shoreface frames with measured depth-average velocities and observed wind and wave conditions on 19 November 2017 8:05 (storm conditions, peak flood)

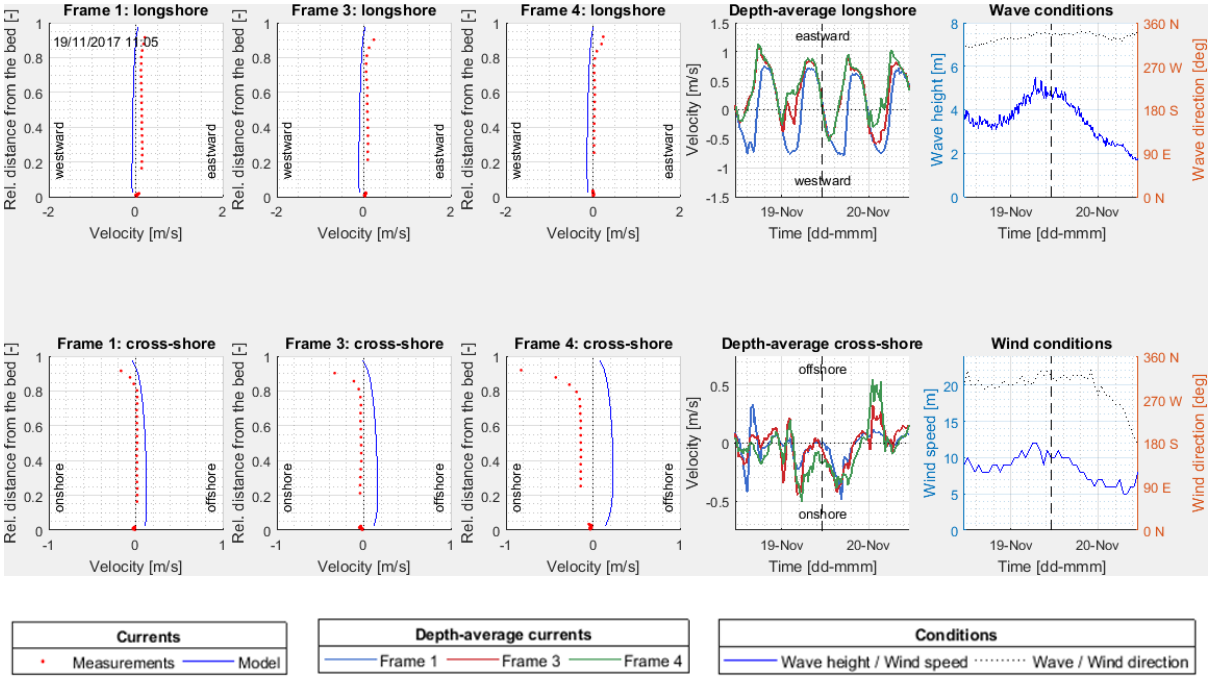

Figure A.9 Measured and modelled (DCSM 0.5 nm) velocity profiles at lower shoreface frames with measured depth-average velocities and observed wind and wave conditions on 19 November 2017 11:05 (storm conditions, ebb)

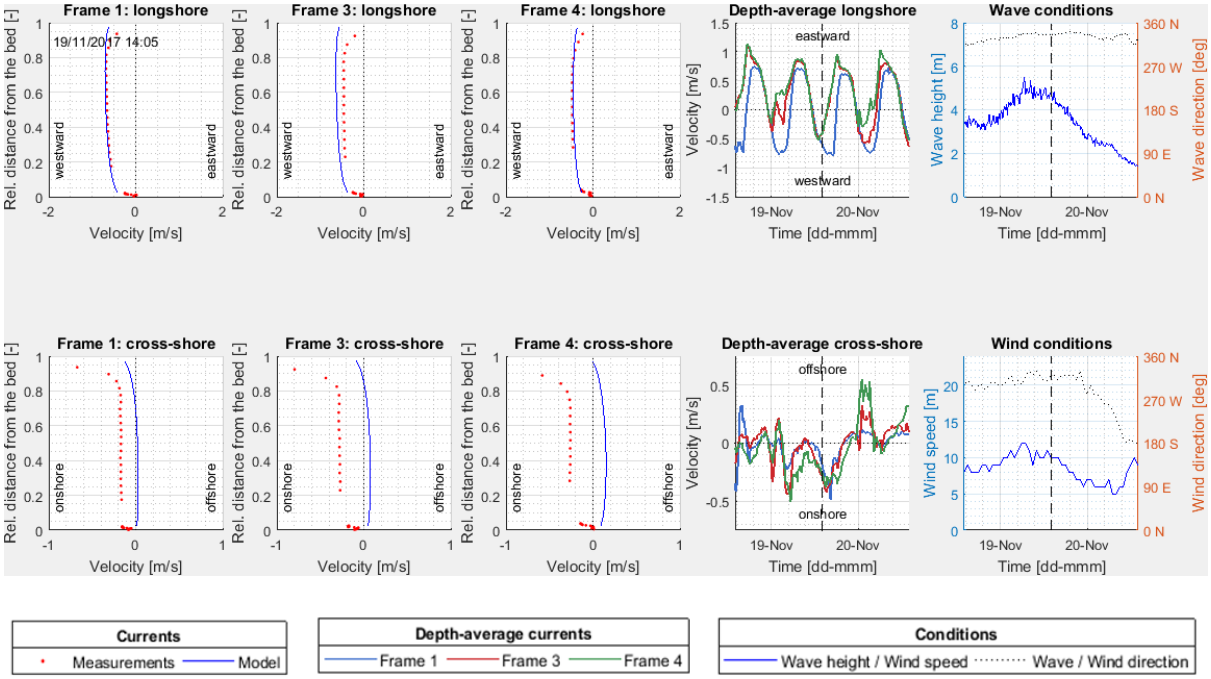

Figure A.10 Measured and modelled (DCSM 0.5 nm) velocity profiles at lower shoreface frames with measured depth-average velocities and observed wind and wave conditions on 19 November 2017 14:05 (storm conditions, peak ebb)

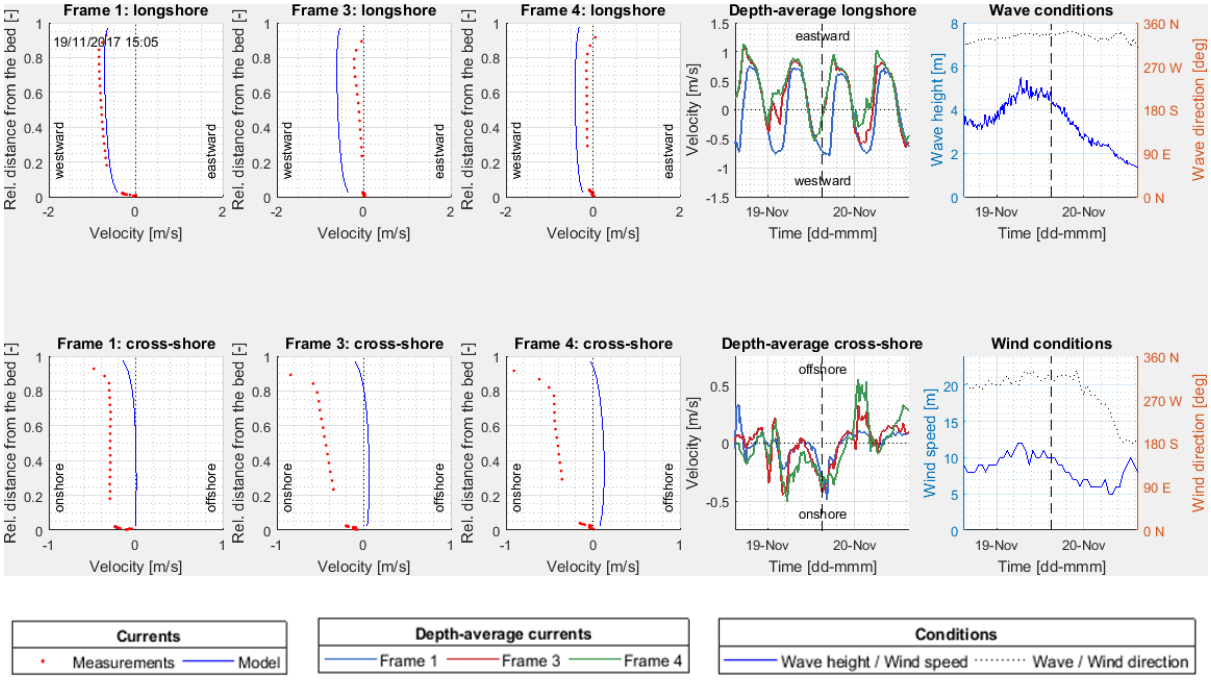

Figure A.11 Measured and modelled (DCSM 0.5 nm) velocity profiles at lower shoreface frames with measured depth-average velocities and observed wind and wave conditions on 19 November 2017 15:05 (storm conditions, flood)

APPENDIX C. BEDLOAD AND SUSPENDED LOAD TRANSPORT TIME SERIES

In this appendix time series of the bedload and suspended load sediment transport in the longshore (Figure A.12) and cross-shore (Figure A.13) direction calculated using TSAND from the modelled and the measured currents are given.

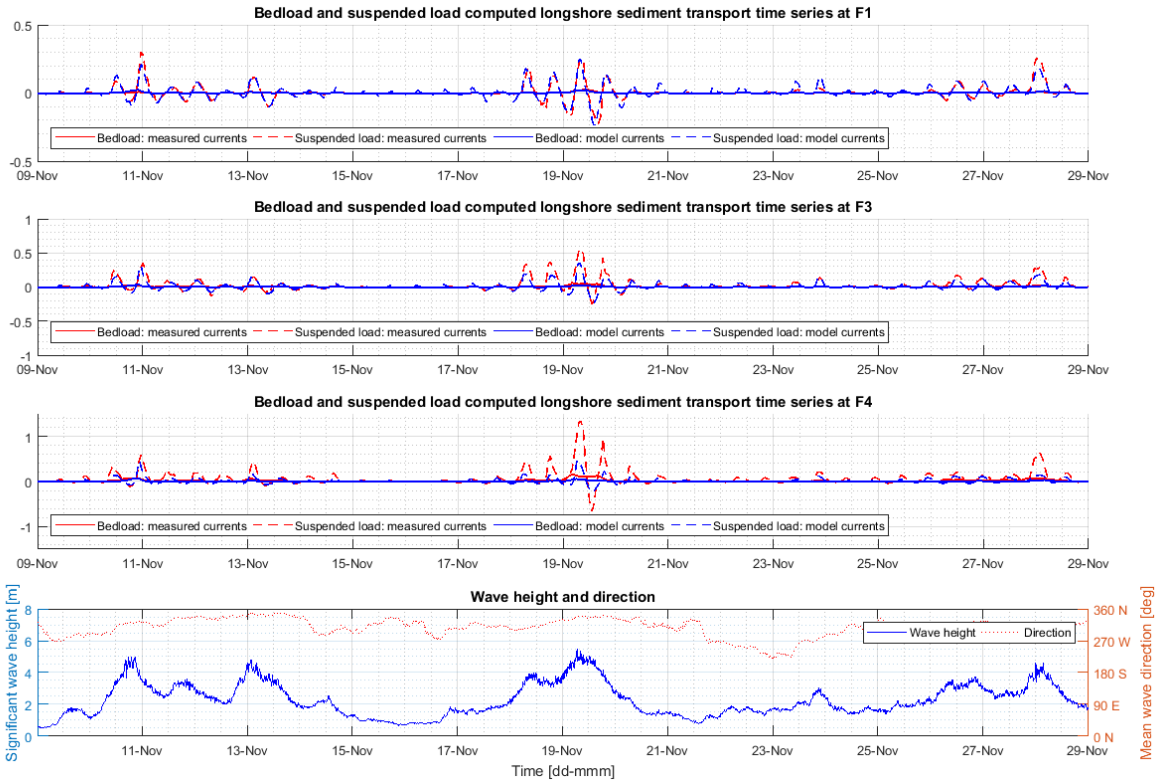

Figure A.12 Bedload and suspended load longshore transport time series calculated from the modelled and the measured currents

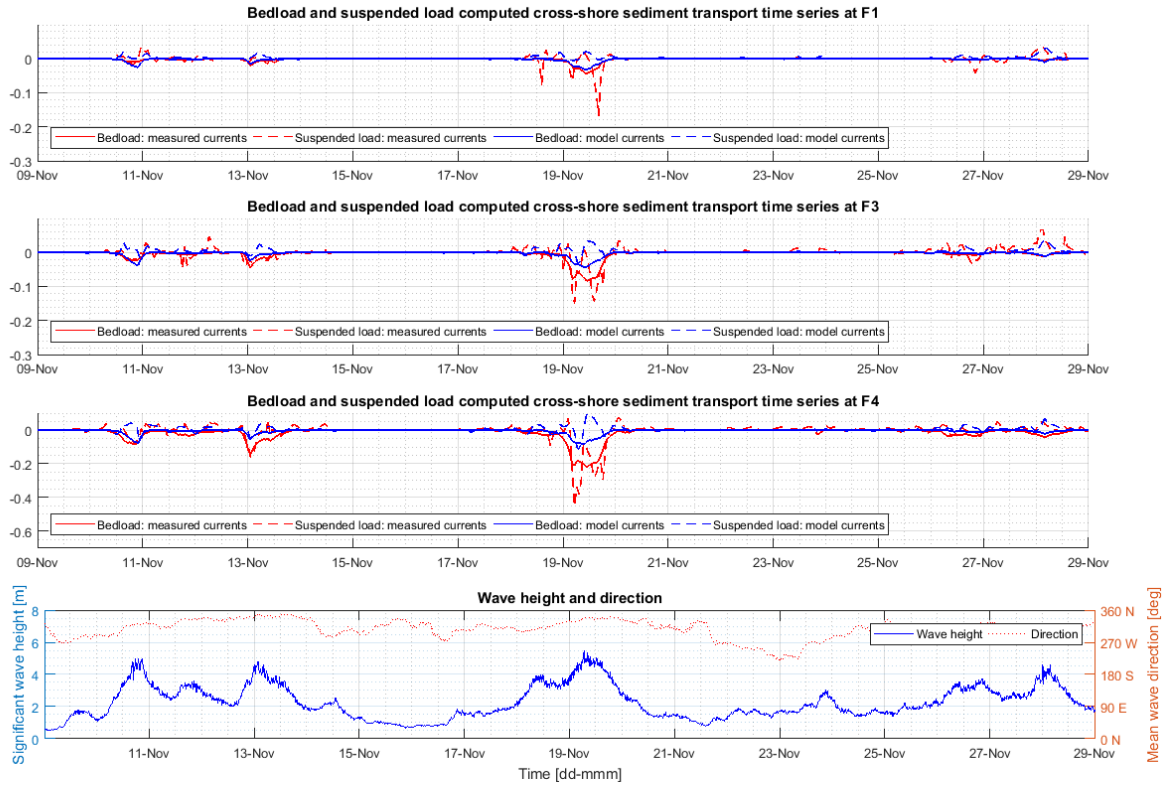

Figure A.13 Bedload and suspended load cross-shore transport time series calculated from the modelled and the measured currents